A new simplified vector-based model to support solar energy planning at urban scale

Liao Wei

Robinson College

University of Cambridge

Date of Submission: 7th August, 2019

This dissertation is submitted for the degree of

Doctor of Philosophy

This thesis is the result of my own work and includes nothing which is the outcome of work done in collaboration except as declared in the Preface and specified in the text. It is not substantially the same as any that I have submitted, or, is being concurrently submitted for a degree or diploma or other qualification at the University of Cambridge or any other University or similar institution except as declared in the Preface and specified in the text. I further state that no substantial part of my thesis has already been submitted, or, is being concurrently submitted for any such degree, diploma or other qualification at the University of Cambridge or any other University or similar institution except as declared in the Preface and specified in the text. It does not exceed the prescribed word limit for the relevant Degree Committee.

W. Liao

07 Feb 2020

Abstract

Dissertation title: **A new simplified vector-based model to support solar energy planning at urban scale**

Wei Liao

Evaluation of solar potential is a necessary step for integrating solar technologies in buildings in order to properly assess the benefits of harvesting solar energy and draw well-informed decisions in various design phases. Solar energy planning at urban scale requires large-scale solar analysis to support various decision-making contexts, such as making urban solar targets, prioritizing urban zones or buildings for solar integration, and optimizing solar technologies tailored for targeting buildings. Existing tools have the following major limitations to support such decision-making situations. (1) Current advanced simulation models based on ray trace and ray interception techniques are not effectively scalable to evaluate solar potential at urban scale due to the expensive modelling process and computational cost. (2) Simple and statistical models developed for large-scale analysis are not suitable to accurately predict solar irradiance on individual surfaces with proper consideration of urban shading and reflection. This dissertation addresses the need for developing scalable, efficient analysis methods to support the solar energy planning process.

This dissertation has developed a simplified vector-based model that effectively predicts the solar potential of urban areas on the basis of consideration of the urban context. The proposed model is based on vector-based methods without the use of ray trace and ray interception techniques, and consists of new methods that suitably account for the non-uniform solar radiation of the sky, obstruction by urban surfaces, and reflection by urban surfaces in urban areas. The proposed model establishes three new methods to simplify the calculation in the context of urban applications: (1) a two-segment discretisation model, (2) an edge-angle detection obstruction model, and (3) a unified view-angle-based reflection model.

This dissertation demonstrates the usability of the new model in supporting decision-making in the solar energy planning process. It addresses the following two hypotheses to examine the usability of the new model: (1) Simplified, vector-based model, tailored to urban applications, predict accurate solar radiation on urban surfaces to effectively support urban-scale analysis and (2) solar analysis with full representation of urban surroundings is necessary in the calculation of urban shading and solar reflection to correctly support distributed PV planning.

For the first hypothesis, the performance of the method is compared against the advanced daylight simulation program RADIANCE and measurements obtained from controlled experiments. The first comparison demonstrates the new method provides flexible setting options for different resolution and prediction accuracy requirements and generates reasonably accurate predictions. The second comparison further confirms the prediction accuracy against the measurements for the horizontal and vertical surfaces under different shading and reflection conditions. The comparison with the ray interception approach demonstrates the computational efficiency of the proposed obstruction model for solar analysis that substantially reduces calculation iterations for detecting sky and building obstructions. For the second hypothesis, predictions and decisions derived by the developed method are compared against those by a lower fidelity models to investigate the importance of modelling urban shading and reflection with full representation of urban surroundings in three decision making contexts of urban-scale distributed PV planning process. Additionally, the second hypothesis is furthered examined and highlighted by investigating the effect of an additional dynamic PV model on decision-makings in comparison with the effect of the proposed high-fidelity solar radiation model for urban shading and solar reflection. The new model is demonstrated to enable cost-efficient solar potential analysis based on urban contexts for supporting solar energy planning at urban scale.

Preface

I remember the greyness in the sky every time when I travelled back home in China for a vacation. Looking down from the plane, it was like a thin sheet covering the cities, the towns or even the remote mountains and rice fields. There was not much detail to see from the plane, not because of the distance, but the air pollution hunting over the land. As someone who grew up in the southern part of the country, memory with the sky was not like that when I was little. After 30 years of continuous success of economic development, China transformed from a poor and underdeveloped country to an economic giant today. Life nowadays is much better for the people, but not so much for the air we breathe in. In fact, the air pollution has gotten so bad in the northern part of the country, during the winter season, the pollutions were blown across the sea all the way to Korea and Japan by the monsoon from Siberia. There started a war, a war announced against the polluted air, a difficult war to win as more than 70% of the energy generated in China is coal-based, the dirtiest source of energy knew for a long time. Due to the political concern of energy safety of an oil-dependent energy system, the Chinese government is reluctant to expand its gas plants, a relatively cleaner source of energy compared with coal-based plants, and has no choice but turn to renewable energy.

Under such background, I began my story of studying solar energy and its utilization in the built environment. During the study in my master course, I was lucky to participate in a project funded by the National Nature Foundation of China, where I studied the benefits and challenges of integrating semi-transparent PV on building facades. As it is important to understand how solar energy can be utilised on the building level, I soon realised it is not enough. Solar technologies should not be some fancy showcases on some fancy hi-tech looking architecture. If we ever want to win the war against air pollution, it needs to be applied in a much larger scale with a lot more people to participate to embrace this renewable energy. The current urban area needs to be more progressive in integrating solar technologies in the built

environment and future development. One key task to promote solar energy utilisation in urban buildings is to know how the solar resource is first distributed in our cities. And I found a research gap in the methods for properly and efficiently predict solar energy on such large-scale, I perused a further answer in my PhD course. I chased after the question of how we can better, more efficiently deliver a solar potential evaluation at urban-scale. The methods and tools I established in the study is an attempt to contribute a small but crucial part of what could help us to better fight in the environmental war against air pollution and energy crisis.

Lastly, I declare that this dissertation is my own work and contains nothing which is the outcome of work done in collaboration with others, except as specified in the text and acknowledgements. The work in this dissertation is not substantially the same as any that I have submitted, or, is being concurrently submitted for a degree or diploma or other qualification at the University of Cambridge or any other University or similar institution except as declared in the Preface and specified in the text. I further state that no substantial part of my dissertation has already been submitted, or, is being concurrently submitted for any such degree, diploma or other qualification at the University of Cambridge or any other University or similar institution except as declared in the Preface and specified in the text. The dissertation does not exceed the prescribed word limit for the relevant Degree Committee.

Cambridge, 15 Apr 2019

Acknowledgements

The dissertation only becomes reality with the firm support and generous help from many individuals and from the funding bodies. I would like to express and extend my gratitude as follows.

I am ineffably indebted to my supervisor Dr. Yeonsook Heo, for her most valuable guidance and patience throughout my entire course. Her insightful advice and comments on the research project have been greatly inspirational, and in fact essential to the completion of the dissertation.

I am greatly thankful to Dr. Shen Xu and his research team. Field experiments would not be possible without their full supports in providing the required funding and human resources. I would like to express my gratitude to all of the members of the team, especially to Jianghua Wang, Zhaojian Wang, Zihao Zhang for their valuable time and efforts during the experiment.

I would also like to thank my colleagues in the research group of Behaviour and Building Performance (BBP). It has been a great pleasure working with them and learning from them through accessing and discussing a wide range of research topics in the group.

The research project would not be possible without the funding granted by the Cambridge Trust and the Chinese Scholarship Council. I thank them for this once of a lifetime opportunity to study at the University of Cambridge.

Last but not least, I want to thank all of my families and friends for their unconditional love and supports.

Thank you!

Table of contents

ABSTRACT I

PREFACE III

ACKNOWLEDGEMENTS V

TABLE OF CONTENTS VI

NOMENCLATURE VIII

CHAPTER 1: INTRODUCTION - 1 -

1.1 Solar energy planning at urban scale - 1 -

1.2 Current methods for urban-scale solar potential analysis - 4 -

1.3 Research objectives and methodology - 8 -

1.4 Structure of the dissertation - 10 -

CHAPTER 2: A SIMPLIFIED VECTOR-BASED MODEL FOR URBAN-SCALE IRRADIANCE PREDICTION - 12 -

2.1 Current approaches for modelling urban contexts in solar analysis - 13 -

2.1.1 Classic approach - 13 -

2.1.2 Statistical model-based approach - 14 -

2.1.3 2.5D raster/pixel-based approach - 15 -

2.1.4 Urban canyon-based approach - 17 -

2.1.5 3-dimensional vector-based approach - 19 -

2.1.6 Current simulation software - 22 -

2.2 Main features of the proposed models - 24 -

2.2.1 Sky discretisation model - 26 -

2.2.1.1 Current standard model - 26 -

2.2.1.2 Proposed model - 29 -

2.2.2 Obstruction model - 37 -

2.2.2.1 Current standard model - 37 -

2.2.2.2 Proposed model - 38 -

2.2.3 Reflection model - 40 -

2.2.3.1 Standard model - 40 -

2.2.3.2 Proposed model - 41 -

2.3 Surface subdivisions - 44 -

2.4 Implementation - 45 -

2.5 Summary - 47 -

CHAPTER 3: MODEL VALIDATION - 48 -

3.1 Model validation framework - 48 -

3.2 The studied urban area - 49 -

3.3 Comparison against RADIANCE - 50 -

3.3.1 Effect of model setting parameters - 51 -

3.3.2 Results - 53 -

3.4 Comparison against controlled experiments - 56 -

3.4.1 General design - 56 -
3.4.2 Construction of the physical urban geometry - 59 -
3.4.3 Weather measurements - 63 -
3.4.4 Measurements uncertainty - 65 -
3.4.5 Impact of parameter uncertainty on the prediction - 66 -
3.4.6 Results - 68 -
3.5 Computational efficiency - 74 -
3.6 Summary - 76 -
CHAPTER 4: RELEVANCE OF THE NEW MODEL IN THE URBAN SOLAR ENERGY PLANNING PROCESS - 78 -
4.1 Introduction - 78 -
4.2 Urban distributed PV planning process - 81 -
4.2.1 Political phase - 82 -
4.2.2 Urban design phase - 83 -
4.2.3 Building design phase - 84 -
4.2.4 Summary of decision-making contexts selected for analysis - 85 -
4.3 Radiation prediction model - 87 -
4.3.1 Classic model - 87 -
4.3.2 Canyon-based model - 88 -
4.3.3 High-fidelity vector-based model - 89 -
4.4 PV system model - 90 -
4.4.1 Static PV model - 90 -
4.4.2 Dynamic PV model - 92 -
4.4.2.1 Physics-based methods - 93 -
4.4.2.2 Statistical models - 96 -
4.4.3 Comparison among different PV cell temperature models - 97 -
4.5 Comparison in decision-making contexts - 106 -
4.5.1 Selected models for comparisons - 106 -
4.5.2 Examination of radiation prediction models - 108 -
4.5.2.1 Solar targets: maximum PV potential - 108 -
4.5.2.2 Place-making - 110 -
4.5.2.3 Economic assessment - 113 -
4.5.3 Examination of PV models - 116 -
4.5.3.1 Solar targets: maximum solar potential - 116 -
4.5.3.2 Place-making - 117 -
4.5.3.3 Economic assessment - 118 -
4.6 Summary - 119 -
CHAPTER 5: CONCLUSIONS AND FUTURE WORK - 121 -
5.1 Summary and conclusions - 121 -
5.2 Future research - 124 -
REFERENCE - 126 -
PUBLICATIONS - 138 -

Nomenclature

BES	building edge subdivision
BVA	solid angle of building view
GVA	solid angle of ground view
SVA	sky view angle
SVF	sky view factor
SHS	sky horizontal subdivision
SIS	strip inside subdivision
SRSS	sky radiance sampling subdivision
UHA	urban horizontal angle

avg	average
B	building
diff	diffuse
dh	diffuse horizontal
G	irradiance (W/m^2)
g	ground
K	number of SIS
low	lower boundary of sky patch (rad)
M	number of SRSS
N	number of SHS
norm	normal
R	radiance ($W. sr/m^2$)
up	upper boundary of sky patch
β	altitude of lowest blocked point (rad)
ρ	average reflectance
σ	angle between surface normal and a line (rad)
ϕ	altitude of sky patch (rad)
ξ	altitude of highest blocked point (rad)
γ	angle of plane sloped
ψ	azimuth bandwidth

Chapter 1: Introduction

1.1 Solar energy planning at urban scale

Solar energy has been well recognised as a clean and almost inexhaustible energy. With the improvement of solar technology, continuously decreasing costs and increasing acceptance by the public, it has been considered as one of the most promising energy sources. Different solar technologies, including BIPV (building integrated photovoltaic), solar thermal collector (STC) and other solar design strategies in buildings, have been increasingly adopted by architects, developers, city planners and authorities as the way to provide clean energy and therefore reduce the demands of traditional fossil fuels.

Through solar technologies, direct radiation from the sun, diffuse radiation from the sky and reflected radiation from surrounding environment reaches solar collectors that transfer the solar energy into various forms, such as electricity through Photovoltaics (PV) (Tripathi et al., 2016), hot water through thermal collectors (Dupeyrat et al., 2014), or direct heat source through passive solar walls (Bansal et al., 1993; Stritih and Novak, 1996; O'Hegarty et al., 2016). The annual available solar energy on a solar collector varies substantially in different

geological locations due to the diverse climate conditions (e.g. solar positions and paths, cloudiness, air mass) (Besharat, et al., 2013). Built environments also play an important role in creating shading on solar systems due to the surroundings, particularly when an intended solar application area is located in urban areas (Cheng et al., 2006). The available solar energy received on the surfaces of interests, such as building roofs or facades, can be referred to as solar potential (Cheng et al., 2006). Other names such as solar availability or daylight availability are also commonly used in different studies to evaluate the usability of solar energy in buildings (Compagnon, 2004; Chatzipoulka, et al., 2016). Assessment of available solar energy forms a foundation for successful solar applications as it provides key information about possible energy yields for solar projects.

Evaluation of the the solar potential of urban surfaces is an important step in solar energy planning. Kanters and Wall (2016) comprehensively identified five different design phases for solar energy planning in urban environments: political phase, urban design phase, building design (new buildings) and renovation (existing buildings) phase, implementation and monitoring phase. The political phase where the solar potential of urban surfaces at a large scale is evaluated to inform policy-making and strategic plans for setting and achieving a solar target. For example, Byrd et al. (2013) investigated the maximum PV potential in areas located in the central business district (CBD) and low-density suburbs in Auckland, New Zealand. The study designed the energy generation capacity on the basis of the solar analysis that contributes to reducing the electricity load of a city, supplying energy for a mixture of building types and the charging of electric vehicles, and reducing peak electricity demand. The next level is the urban phase where the key task is “place-making: creating a vision for an area and then deploying the skills and resources to realise that vision” (Yeang, 2000). Solar potential analysis can inform urban designers by evaluating the effect of restrictions on variables such as maximum building height and density, extent of impervious surface and open space, and land use types and activities (Montavon, 2010). Furthermore, it is also used to identify the most potential areas for solar applications by providing solar maps of each building or block in an urban area for well-informed decisions by house owners, developers and planners (Mapdwell, 2018). In the

building design and renovation phases, performance-based design (Lewis, 2014) for sustainable buildings requires a detailed analysis of the performance and economic assessment of the designed buildings. In this phase, for example, developers and building owners decide their investment in PV systems on the basis of the payback time of the PV investment given the evaluated solar potential (BRE, 2016; Kessler; 2017; Ingrams, 2018;), and therefore a detailed model of PV systems have been added to the solar radiation prediction model to support investment decisions (Paul et al., 2010). Kanters and Wall (2016) pointed out that different levels of tools are necessary to provide useful information in different design phases. They also highlighted that the level of detail in the analysis model required for design phases increases as the design process goes from top (e.g., political phase and urban phase) to bottom (e.g., individual building and implementation phase).

Specifically, the rise of distributed PV planning in urban areas places an urgent demand for proper evaluation of solar potential at urban scale. Different from a traditional and centralised PV plant in a remote location without the interference of urban shading, urban distributed PV, as the name suggests, integrate PV systems in individual buildings distributed in a complex urban environment. On one hand, the advantage of the distributed PV system in urban areas is that it provides energy directly in the buildings where energy is consumed. As a result, it reduces the need for extending infrastructure to transmit PV yield through long distances to consumers and avoids line losses of electricity during distribution. Besides, the distributed PV system can be grid-connected to sell the excess PV yield to the city grid as part of the urban energy system, and thus reduces the need of investing an energy storage system individually in individual buildings. On the other hand, however, urban distributed PV planning requires solar potential analysis of individual buildings across a large urban area where they suffer substantial PV yield losses due to urban shading from the surrounding buildings, and therefore requires careful assessment of potential PV yield with consideration of the urban context to draw well-inform design decisions. For example, urban solar maps have been used to assist in selecting locations with high solar availability for PV installation by providing information about predicted PV yield, estimated investment cost, and potential carbon emission

reduction (Berlin Solar Atlas, 2018; Mapdwell, 2018; Solarkataster, 2018). Some researchers further incorporated additional parameters, such as historical urban data including building types and ages for a comprehensive evaluation of solar applications in urban environment (Amado and Poggi, 2014; Berlin Environment Atlas, 2018). Researchers have also explored the electricity network compatibility to adopt the predicted PV yield electricity in urban areas. Wall (2012) generated hourly and monthly PV yield predictions and coupled them with three different distribution grids at one planned urban area in Sweden to identify the maximum PV hosting capacity and accordingly the resulting overload capacity given a maximum PV yield potential in the urban area. These studies above have demonstrated the importance of solar analyses at urban scale in evaluating solar projects for a large audience of planners, developers and property owners in terms of economic and environmental benefits.

1.2 Current methods for urban-scale solar potential analysis

Several research studies have attempted to derive generic relationships between urban morphology and solar potential through statistical analyses. Mohajeri et al. (2016) characterised the urban morphology in terms of compactness measures, including site coverage, plot ratio, and building density, and found the received solar radiation in the tested urban area is strongly correlated with its distance to the dense city centre, and with the average building height in that urban area. The author also confirmed various correlation coefficient between the yield of different active and passive solar applications in relation to urban compactness. The research provides general guidelines for evaluating the solar potential of large urban areas; for example, solar irradiance differs up to 30%–40% depending on the compactness of an urban area, and annual solar irradiation in the suburban area is generally 10–15% higher than that in the city centre. However, this level of information is not sufficient to support a wide range of design and planning projects for other cities nor provides the detailed information needed to identify a group of building areas with the maximum solar potential within the urban area and optimise the design of solar systems for the identified areas. Another study carried by Sarralde et al. (2015) used an extensive set of urban form parameters (18 parameters) to capture variability in the urban morphology of about 4700 neighbourhoods to define the correlation between the

urban morphology and the solar potential of the neighbourhood. However, this study provides aggregated-level information about the correlation between the overall urban morphology and the solar potential of the entire neighbourhood. This level of information may be useful if the same design strategies are applied to all the buildings in the neighbourhood area, but it is not sufficient to prioritise buildings for solar integration, nor tailor the design of solar technologies for individual buildings.

Another approach for urban-scale solar analysis is to perform a simulation of solar irradiance by using urban fabric as an input, to generate the outcomes of solar potential for a specific urban case in the decision-making process. Different types of models and methods have been developed for predicting solar potential. In terms of how the urban context is considered in the model, they can be grouped into classic models, historical satellite data, canyon-based models, 2.5D raster-based models, and 3D-vector-based models.

Classic approaches (Besharat et al., 2013; Fortin et al., 2008; Freitas et al., 2008) that ignore urban shading and solar reflection from surrounding buildings have been long used for a quick estimation of PV yield on roofs where usually shading and reflection is less significant than those on walls. Historical satellite data have been used to provide annual or monthly predictions of available solar energy at different locations (Sabbagh et al., 1977; Tarpley, 1979; Cano et al., 1986; Gueymard et al., 2011). This approach, however, does not provide predictions of solar energy on vertical surfaces. The low spatial resolution of satellite data is also an issue because it prohibits the proper distinction of individual surfaces in urban areas.

Some models are based on a simplified urban representation to consider urban shading and solar reflection. For example, canyon-based approaches (Arnfield, 1990; Robinson and Stone, 2004; Bozonnet et al., 2005) are based on the urban canyon concept that assumes that buildings that contribute to radiation obstruction and reflection have the same height without skyline variation. They only consider the surrounding buildings within the canyon while ignoring variation in the building height in an urban area. Others such as 2.5D raster-based

approaches (Redweik et al., 2013; Lindberg et al., 2015) are based on actual urban footprints with varying building heights for the representation of dynamic skyline obstruction. However, due to the 2.5 D representation of an urban geometry, vertical surfaces such as walls and façades are defined as binary pixel points. Therefore, an additional process is required with additional hyperpoints assigned within each pixel to represent different height positions for the determination of daylight obstruction at each hyperpoint. As a result, the process for calculating shadings on walls/façades is fairly complicated and fundamentally requires computationally expensive ray-interception algorithms to aid the process, and calculating reflection from surrounding buildings is not possible.

3D-vector-based approach is based on a full representation of surrounding buildings and allows for an accurate reflection of urban shading and solar reflection in a unified manner as 3D points with vector information (i.e., knowing the facing direction) do not need to be pre-classified and can be passed on for calculating daylight obstruction and reflection in the exact same manner. For instance, the advanced daylight simulation tool RADIANCE (Ward, 1994), uses an urban geometry model in a complete 3D format with information of surface vectors and uses computational techniques such as ray tracing or ray interception for complex calculation of detailed obstruction and reflection.

However, current vector-based, high-fidelity models, especially the ones relying on ray-based algorithms, tend to be expensive in terms of modelling and computational costs. A simplified radiosity algorithm was developed by Robinson and Stone (2004) to improve computational efficiency for solar analysis in urban contexts. However, even after the implementation of simplifications to these methods, they are fundamentally based on ray-tracing or ray intercept algorithm with a complex sky discretization model, and consequently tend to result in heavy computational burdens for detecting obstruction and calculating reflections among building and ground surfaces. Furthermore, detailed data on individual surface properties are typically unavailable for urban-scale solar analyses. Given the scale of solar analysis, it is not possible to obtain a detailed level of information about individual

building envelope details (e.g., balcony, windows and parapets) and associated surface properties. Even if all surface albedos are set to the same values in RADIANCE, for example, the calculation process is still the same as that for the case with different albedos. Setting the same albedo for all surfaces does not reduce the computational cost of RADIANCE. Hence, there is room for developing a simplified method tailored to urban applications with typically available urban data.

Therefore, two major limitations regarding the current methods at delivering solar potential at urban scale are identified as follows:

(1) Current advanced simulation models based on ray trace and ray interception techniques are not effectively scalable to evaluate solar potential at urban scale due to the expensive modelling process and computational cost.

(2) Simple and statistical models developed for large-scale analysis are not suitable to accurately predict solar irradiance on individual surfaces with proper consideration of urban shading and reflection.

The two identified research gaps place a significant obstacle to accurately and efficiently delivering a solar potential analysis at urban scale in aid of urban solar energy planning. For the political decision-making phase that often requires solar potential at national or regional scale, one of the key interests is the total amount of solar yield at large scale rather than individual building scale. The current advanced simulation models could not properly scale up to urban level due to high computational and modelling cost, while simple methods could not properly consider urban shading and reflection and lead to inaccurate predictions. The same problem occurs in urban design phases where prioritizing buildings/areas for solar integration requires solar potential evaluation on all individual buildings in the planned urban area. Hence, there is a need for new analysis methods tailored to aid solar energy planning at urban scale to resolve the two major limitations of the current methods.

1.3 Research objectives and methodology

The objective of this dissertation is to develop a new model for solar potential analysis that can effectively support solar energy planning at urban scale. To overcome the limitations of current methods, the new method achieves the following major features:

- It is a solar analysis model tailored for urban applications with consideration of the urban context.
- It does not require any ray tracing or ray interception.
- It provides easy and flexible setting options for different levels of required accuracy.

The dissertation proposes a simplified vector-based model without the use of ray trace and ray interception techniques, yet consists of new methods that suitably account for the nonuniform solar radiation of the sky, obstruction by urban surfaces, and reflection by urban surfaces. Three new model components are created to simplify the simulation process: (1) a two-segment discretisation model, (2) an edge angle detection obstruction model, and (3) a unified view-angle-based reflection model. Unlike the commonly used current simulation models developed to suit the various daylight applications, the simplified method is developed specifically to reflect the context of urban-scale solar analysis, which potentially reduce the computational cost to effectively support large-scale analyses, while achieving the prediction accuracy required for the solar applications. Furthermore, the proposed method is designed to provide easy and flexible setting options for different resolution and prediction accuracy requirements.

This dissertation demonstrates the feasibility of the new model in supporting decision-making in the solar energy planning process. It addresses the following two hypotheses to examine the usability of the new model:

- Simplified, vector-based model, tailored to urban applications, predicts accurate solar radiation on urban surfaces to effectively support urban-scale analysis.
- Solar analysis with full representation of urban surroundings is necessary in the calculation of urban shading and solar reflection to correctly support distributed PV planning.

The first hypothesis is examined by evaluating the model performance of the proposed model. First, the study compares the predictions of the developed method against the advanced daylight simulation program RADIANCE and measurements obtained from controlled experiments through a case study of an urban area located in Wuhan, China. Before comparisons, different configurations and settings of the developed method are first tested for achieving a good balance between prediction accuracy and computational efficiency. The first comparison evaluates the prediction accuracy of the new model against RADIANCE. The second comparison against controlled experiment measurement further tests the accuracy of the new model to predict solar radiation in a real physical environment. Next, the computational efficiency of the new method for detecting surrounding solar obstructions is tested against the current ray-based algorithm.

The second hypothesis is examined by comparing predictions and decisions by the developed method with those of a lower fidelity models to investigate the importance of modelling urban shading and reflection with full representation of urban surroundings. Three decision-making contexts are considered in an urban-scale distributed PV planning process. Additionally, the hypothesis is furthered examined and highlighted by investigating the effect of an additional dynamic PV model on decision-making in comparison with the effect of the high-fidelity model for urban shading and solar reflection.

1.4 Structure of the dissertation

The research outline is illustrated in Figure 1 with the following chapters presented in the dissertation.

- Chapter 1 presents motivations for solar potential analysis in aid of solar energy planning at urban scale, summarises the limitations of current methods, and proposes a new method that can support solar energy planning at urban scale.
- Chapter 2 presents a simplified vector-based model tailored to solar irradiance prediction in an urban context in comparison to current standard models with limited capabilities for urban-scale solar analysis.
- Chapter 3 validates the developed model by comparing the performance of the developed method against the advanced daylight simulation program RADIANCE and measurements obtained from controlled experiments. The computational efficiency of the proposed method of detecting surrounding solar obstructions is tested against the standard ray-based algorithm.
- Chapter 4 demonstrates and examines the usability of the proposed method by examining the relevance of the two key modelling features associated with solar potential evaluation in the solar energy planning process.
- Chapter 5 summarises the dissertation with conclusions and suggestions for future research.

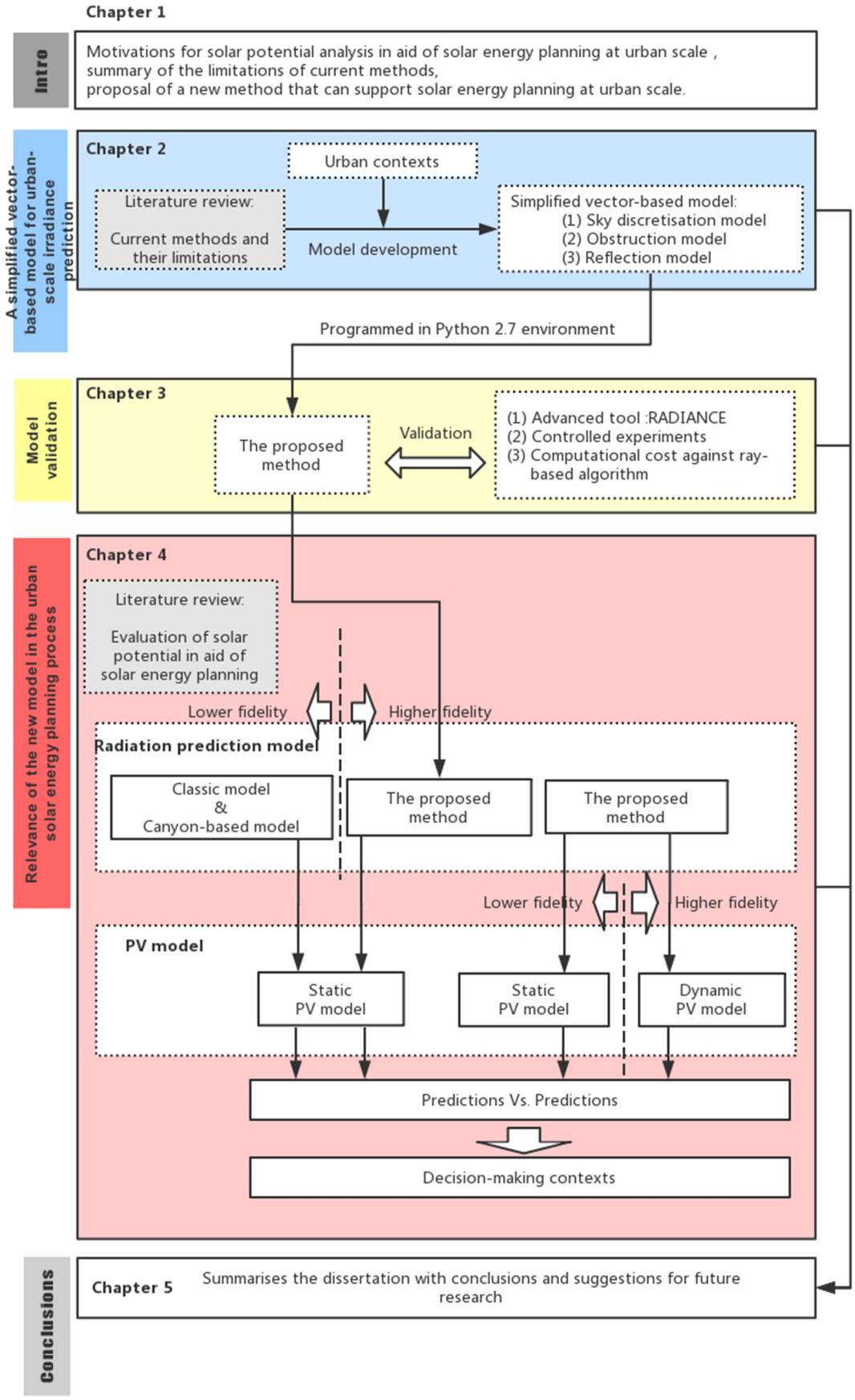

Figure 1. Research outline with the sequence and links between the individual chapters.

Chapter 2: A simplified vector-based model for urban-scale irradiance prediction

This chapter presents a new modelling approach for solar potential prediction at urban-scale. This chapter first summarises the current methods and tools used for the analysis of solar potential at urban scale. A key part in solar analysis for urban applications is how complex urban surroundings are represented for the prediction of shading and solar reflection among urban surfaces. Based on the literature review, the current methods were grouped into five categories, mainly in terms of the spatial dimensions of the urban geometry considered for predicting urban shading and reflection. Then, the chapter summarises the key model components for irradiance prediction at urban scale: sky discretisation model, obstruction model and reflection model. The limitations of the standard models used for urban applications were identified, and a simplified vector-based model was developed to effectively predict solar irradiance at urban scale with proper consideration of urban contexts.

2.1 Current approaches for modelling urban contexts in solar analysis

2.1.1 Classic approach

Classic approaches (Bugler, 1977; Klucher, 1979; Ma and Iqbal, 1983; Hay and McKay, 1985) have been well established and used to estimate global solar radiation on a surface of interest, typically with the assumption that a building is stand-alone without surrounding buildings. Without the consideration of urban context, calculating solar radiation on a surface of interest is straightforward and consists mainly of two steps: calculating the received sunlight by accumulating hourly direct normal irradiance (i.e., the beam sunlight) on a surface given the surface tilt angle and corresponding altitude angle and surface-solar azimuth and calculating the skylight (i.e. diffused irradiance) by estimating the irradiance received from the partly visible sky dome using a isotropic sky model that assumes all of the diffuse radiation is uniformly distributed over the complete skydome. Given the fact that the isotropic sky model is less accurate in weather conditions that are not cloudy and overcast, some researchers (Van Brink, 1987; Hay and McKay, 1988) explored the use of an anisotropic sky to improve the prediction accuracy of diffuse irradiance in various weather conditions. Muneer (1997) applied simple angle calculations given an assumed albedo of the ground surface to calculate irradiance reflected from the ground for a tilted plane, but this approach assumes the ground is completely visible to a plane of interest without any obstruction by surrounding urban surfaces.

Given the fact that shading and reflection in urban areas are mainly due to the surrounding built environment, the basic classic models without any consideration of urban shading can only provide a very crude estimation of received solar radiation in urban environment. Although classic approaches do not account for shading and reflection from surrounding buildings in urban contexts, efforts (Dubayah and Rich,1995; Hofierka and Suri, 2002) have been made to extend the capability of classic models to account for large-scale terrain obstruction such as obstruction from the surrounding mountains represented by GIS-based digital elevation models (DEM). These approaches calculate the obstructed part of sky diffuse irradiance by using the concept of sky view factor (SVF) (i.e., the fraction of visible sky to entire skydome). The consideration of terrain obstruction improves the model performance for calculating solar

radiation in an open field in mountainous regions. However, given the fact that shading and reflection in urban areas are mainly due to the surrounding built environment, the improved classic models are still not sufficient to predict radiation in urban contexts.

2.1.2 Statistical model-based approach

Historical satellite data have been used to provide annual or monthly predictions of available solar energy at different locations (Sabbagh et al., 1977; Tarpley, 1979; Cano et al., 1986; Gueymard et al., 2011). In this approach, predictions of solar energy on vertical surfaces are not available. The low spatial resolution of satellite data is also an issue because it prohibits proper distinction of individual surfaces in urban areas. Typically, meteorological solar radiation data have been used in large-scale solar analyses in the form of a constant hourly irradiance value across the entire city, without consideration of mutual shading among neighbouring buildings. A modified and improved version of the constant approach, PVWatts, was developed by the National Renewable Energy Laboratory (NREL) to calculate the monthly average daily total insolation (sun and sky) on a horizontal surface on the basis of a 40 km square-grid of a typical meteorological year (TMY) dataset for the entire United States (Marion et al., 2001). Although this method accounts for PV panel tilted angle, orientation, and meteorological air temperature in the calculation of energy production, nevertheless, it ignores the shading and reflection effect of the urban context on the solar energy distributed over the urban area.

Meanwhile, existing studies have explored surrogate-model-based approaches based on historical data. Several research papers applied artificial neural networks (ANNs) as a new approach to predict solar irradiance in urban areas (Sözen et al., 2008; Koca et al., 2011; Senkal and Kuleli, 2009). The ANN models used a location of the urban area (e.g. longitude, latitude and altitude), time (e.g. year and month) and historical solar measurements (e.g. mean diffuse radiation and mean beam radiation) as inputs to generate average solar radiation predictions on the ground or roofs for a specific city. Although prediction results showed good agreement with measurements, lacking the ability to predict solar irradiance on specific urban surfaces is a

major limitation. A recent study developed statistical models to provide more location-specific predictions for building roofs (Karteris et al., 2013). However, the statistical models have limitations to extend to predict solar irradiance at fine temporal and spatial resolutions, especially for dense urban areas in which detailed urban morphology needs to be considered as inputs for prediction.

2.1.3 2.5D raster/pixel-based approach

Raster-based approaches based on digital elevation models (DEMs) have been developed to represent the urban landscape on a pixelised 2.5D raster grid for solar irradiance prediction. In these approaches, the solar irradiance received by a target object is calculated by determining whether an object pixel can be observed from either direct or diffuse sunlight.

Early efforts (Dubayah and Rich,1995; Hofierka and Suri, 2002) in developing raster-based methods aimed to account for large-scale terrain obstruction such as obstruction from the surrounding mountains represented by DEMs. In these approaches, whether sunlight is obstructed for each object pixel is determined through producing a shadow map on the DEM, and whether diffuse skylight is obstructed for each pixel is determined by using the concept of sky view factor (SVF) (i.e., the fraction of visible sky to entire skydome). Algorithms for calculating SVF tailored for large-scale terrains (Dozier et al., 1981) were used to pixelise the DEM into grid-based points and run a screening process to identify the nearest grid points that cause the maximum obstruction on each pixel point, which is similar to a radar detecting potential terrain obstructions. The raster-based approaches, considering terrains for solar predictions have been used in regional-scale applications such as precision farming (Reuter et al., 2005), soil moisture studies (Wilson and Gallant, 2000), ecologic assessment (Kumar and Skidmore, 2000), and Hydrology studies (McVicar et al., 2007). Meanwhile, these raster-based approaches have been adopted in some of the tools, such as the Solar Analyst (Fu and Rich, 1999), used to generate solar maps of urban areas. The Solar Analyst is integrated within the ArcGIS environment and has been extensively used to-this-date to generate many solar maps, such as those of New York (CUNY, 2017) and Salt Lake City (Solar Simplified, 2018) for urban

roofs, without consideration of shading and reflection from surrounding buildings. In general, models with consideration of shading due to the terrain level lack the ability to calculate detailed shading by surrounding buildings in urban areas due to their inability of calculating shadow maps and SVF for every point of urban surfaces. To overcome such limitation, improved GIS-based methods tailored for urban applications were later developed.

Improved algorithms and methods have been developed to replace traditional raster-based approaches for urban applications. The latest raster-based methods use digital surface models (DSM) to accurately represent the effect of the surrounding urban morphology on solar irradiance on the 2.5D raster grid. Light detection and ranging (LiDAR) technology is now extensively used to detect objects in urban areas, categorize them into vegetation, ground, and building façades, and provide associated detailed geometric information that allows the creation of DSMs that represent the actual urban context in detail. With DSMs as model inputs, researchers (Lindberg et al., 2015; Redweik et al., 2013) have developed different raster-based shadow calculation methods to determine the obstruction of solar irradiance on building roofs and facades owing to surrounding buildings. For instance, the shadow model developed by Redweik et al. (2013) creates hyperpoints for each pixel in the raster grid and examines whether each hyperpoint is inside (i.e., obstructed) or outside (i.e., unobstructed) of the shadow cast by surrounding buildings to predict direct irradiance.

The latest raster-based approaches greatly improve the capability of predicting solar irradiance on both roofs and facades. However, due to the 2.5 D representation of an urban geometry, vertical surfaces such as walls and façades are defined as binary pixel points (i.e., 1: vertical; 0: non-vertical). Therefore, an additional process is required with additional hyperpoints assigned within each pixel to represent different height positions for the determination of daylight obstruction at each hyperpoint. As a result, the process for calculating shadings on walls/façades is fairly complicated, and calculating reflection from surrounding buildings is not possible. Furthermore, they tend to be computationally expensive for large-scale irradiance predictions as they are based on shadow cast or volume calculations that

fundamentally requires ray-interception algorithm to aid the process (Figure 2). The creation of DSMs often relies on LiDAR technology that is usually expensive and not easily accessible. Indeed, processing data from LiDAR is an intensive process that requires expert skills, thereby making it difficult to use this technology as part of common practices in the building domain. The GIS data is another type of available urban data that can be straightforwardly translated into DSMs for the existing urban infrastructure.

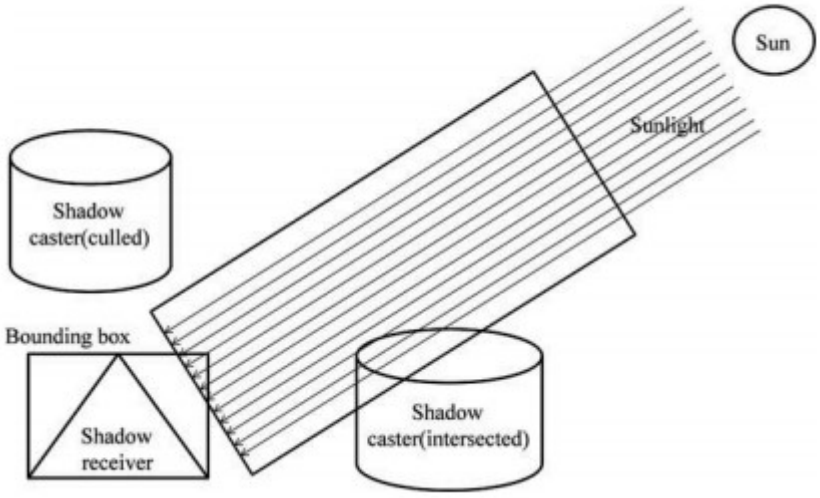

Figure 2. Shadow cast algorithm for obstruction detection aid by ray-interception algorithm (Liang, et al., 2014)

2.1.4 Urban canyon-based approach

Another type of methods for urban solar analysis is based on the urban canyon concept that approximates urban geometry under the assumption that the buildings are identical and regularly distributed in the urban environment. Radiation exchange between surfaces is calculated under this key assumption that allows for translating 3-dimensional urban surroundings into a 2-dimensional canyon elevation. One of the earliest models, developed by Arnfield (1976), is based on canyon geometry and associated surface properties to compute solar and longwave irradiances. The model computes energy exchanges on a canyon cross-section and the solar radiation reflected by canyon surfaces is calculated with the assumption that the reflected radiation is Lambertian (i.e., fully diffused). On the basis of the model, Arnfield (1982) evaluated the effect of canyon albedo, emissivity and other factors for different

land-use zones within Columbus, Ohio and later assessed the role of canyon geometry on solar radiation access (Arnfield, 1990). More recently, Robinson and Stone (2004) developed a canyon-based method in which obstruction from the street across is simplified as a constant horizontal altitude to reflect urban shading for a view point. An obstructing wall from a view point is calculated in terms of angles to upper and lower obstructing surfaces normal to the point of interest for calculating solar irradiance in use with an anisotropic sky model (Figure 3). Bozonnet et al. (2005) developed a simplified method for calculation of radiant interchange among urban surfaces by translating a studied zone into a section of an infinite long street canyon ($W/L \ll 1$ and $H/L \ll 1$) as shown in Figure 4.

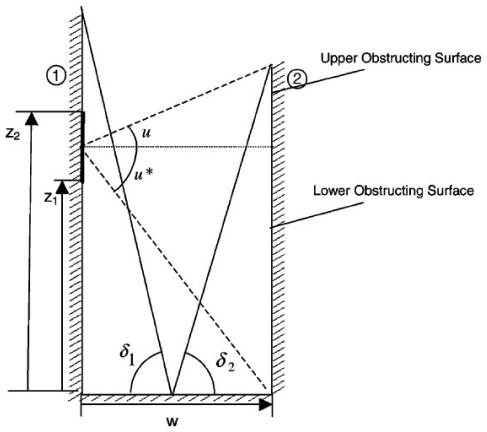

Figure 3. Canyon elevation for solar calculation. (Robinson and Stone,2004)

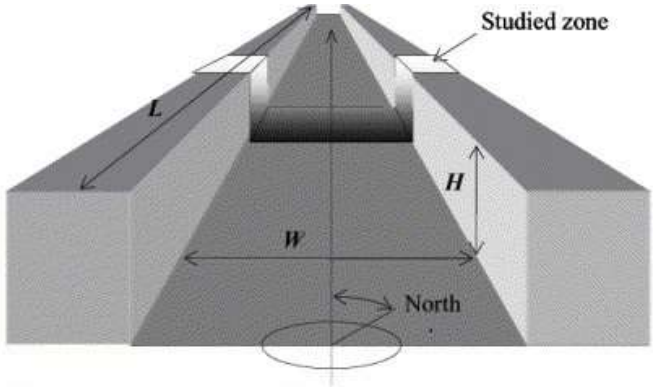

Figure 4. Illustration of a common canyon geometry. (Bonzonnet et al., 2005)

The approximation of an urban geometry into street canyon suggested by the studies mentioned above brings a great advantage in terms of relatively low modelling cost, since it is much more cost-efficient to derive canyon information such as canyon aspect ratio (e.g., H/W) than processing the entire 3D urban geometry for calculating urban shading and reflection. The

canyon concept may sufficiently capture the urban geometric characteristics in a "flat" city in which buildings indeed have similar heights and are regularly distributed along streets, such as Paris and many of the European cities (Figure 5, left-subfigure). However, the canyon concept cannot capture a more complex urban landscape (Figure 5, right-subfigure) in which the distribution of buildings is significantly heterogeneous in terms of building height and shape.

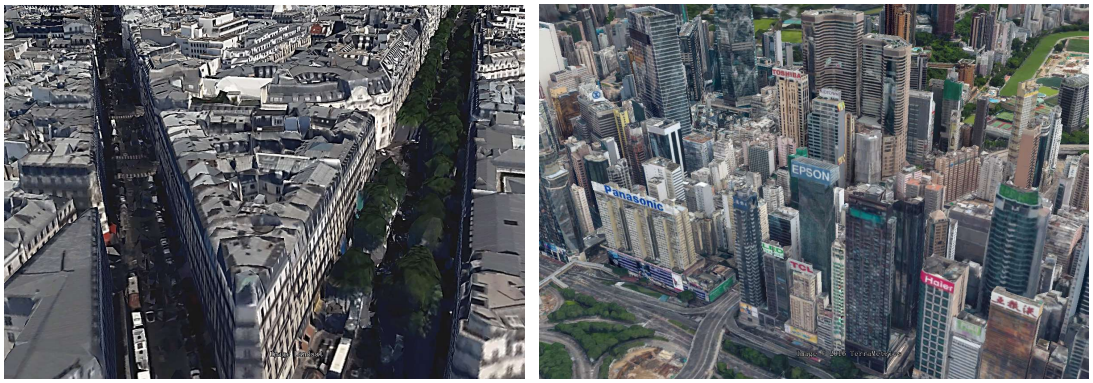

Figure 5. Typical street canyons in a "flat" city (left) in Paris, Europe and "vertical" city in Hongkong, China (right).

2.1.5 3-dimensional vector-based approach

Three-dimensional vector-based simulation models have the highest-fidelity representation of complex urban morphology for solar analyses. In these models, physical objects are modelled individually as vector objects in three dimensions, which gives us great advantages to accurately compute any angle of solar radiation onto individual surfaces as vector objects tell us not only where they are located by 3D coordinates but also which direction they face to by their normal vectors.

Either an isotropic or anisotropic sky model is used in this approach to represent the sky radiation and calculate the diffuse solar radiation on a test point from the visible sky. Traditionally, high-fidelity, vector-based simulation software, such as RADIANCE and Daysim, are commonly used for indoor daylight simulations or image rendering. Daysim (Reinhart and Breton, 2009), using RADIANCE as the simulation engine, provides an effective workflow well-tailored for indoor daylight simulations with a more user-friendly interface. More recently, the simulation software has been used to perform irradiance simulation for generating detailed

city solar maps (Jakubiec and Reinhart, 2012), or for evaluating and improving solar irradiance availability for buildings in urban environments (Kämpf et al., 2010). However, vector-based models used in RADIANCE and Daysim are computationally expensive as they are based on complex algorithms (e.g., raytracing method) in association with the use of a sky discretisation model designed to be generally applicable for various daylight applications. Raytracing is commonly used for detecting light obstruction and reflection. Although forward ray tracing (Nadal and Moll, 2012) can accurately capture light phenomenon such as refraction and Fresnel effect, it is very inefficient as it generates many light rays that never reach the final viewpoint. In addition, as refraction and Fresnel effect is much less significant for daylight assessment in buildings and urban environments, backward raytracing (Arvo,1986) is more commonly used in the field. The commonly used daylight simulation software programs, including Daysim, use backward raytracing with the daylight coefficient method and Perez sky model to perform indoor daylight simulation for prediction of daylight illuminance and glare. Recently, the hybrid ray-tracing method that combines the two mentioned methods were introduced (Chan and Tzempelikos, 2012), but it is nevertheless a naturally heavy and computationally aggressive approach. Furthermore, detailed information on the surface properties of urban surfaces are required as model inputs, and may not be attainable for urban-scale applications for which very limited data exists for individual surface characteristics (e.g., surface reflectance, roughness, specular reflectance, etc.) in urban areas. Indeed, the urban solar studies described above on the basis of the simulation model have often used a single value to describe the surface properties of all building surfaces, and have assumed that all the surfaces in the studied urban area have the same reflection characteristics. For vector-based approaches, both computational cost and urban data availability are currently the two key issues for large-scale urban simulation. Therefore, there is room for developing new models to cope with such issues. It should be noted that there is a growing effort to collect ground-based and remote-sensed survey data (Romanoni, et al., 2017; Sun et al., 2012), which can be used to estimate individual surface properties in a cost-effective manner in the future.

Simplifications to the vector-based models have been suggested by researchers to reduce the computational burden of simulations for urban-scale applications. Erdélyi et al. (2014) developed a three-dimensional solar radiation model (SORAM) and tested it against measurements from a real urban area. SORAM ignores reflected irradiance but uses the high-resolution sky model and ray tracing method to detect obstructions. The accuracy of SORAM was validated against real measurements, but the computational efficiency of the method for large-scale urban applications was not discussed. Robinson and Stone (2004) developed a simplified radiosity algorithm (SRA). In SRA, the reflection model is simplified on the basis of the assumption that all reflected surfaces are Lambertian. With the use of the Tregenza sky model, SRA calculates solid angles of each sky patch in relation to a viewpoint to compute uniform radiance of the sky patch on to the viewpoint. A technique of cumulated sky radiance is incorporated in SRA, where both hourly direct and diffuse radiance are pre-processed and computed into one single sky radiance map beforehand in order to reduce the number of calculation iterations for longer simulation periods (e.g., monthly and annual predictions). SRA also uses the mathematical technique of matrix inversion to reduce the computational cost for reflection calculation. The same authors demonstrated that SRA provides accurate predictions in comparison to RADIANCE. SRA is used in SunTool (Robinson et al., 2007) and CitySim (Walter and Kämpf, 2015) developed for simulation and optimization of urban sustainability.

Among the existing methods described above, the vector-based simulation methods offer functionalities that provide accurate predictions for solar analyses. However, even after the implementation of simplifications to these methods, they are fundamentally based on ray-tracing or ray intercept algorithm with a complex sky discretisation model and, consequently, tend to result in heavy computational burdens for detecting obstruction and calculating reflections among building and ground surfaces. Furthermore, detailed data on individual surface properties are typically unavailable for urban-scale solar analyses. Given the scale of solar analysis, it is not possible to obtain a detailed level of information about individual building geometry and associated surface properties. Even if all surface albedos are set to have the same values in RADIANCE, for example, the calculation process is still the same as that

for the case with different albedos. Setting the same albedo for all surfaces does not reduce the computational cost of RADIANCE. Hence, there is room for developing a simplified method tailored to urban applications with typically available urban data.

2.1.6 Current simulation software

Table 1 lists some of of the software on the basis of different methods discussed above for solar potential analyses at different design scales. Tools such as Solei-32 and SolarFlux target regional-scale solar analyses that need to take into consideration geographical features of an area of interest and, therefore, deploy the basic raster-based models that do not consider complex urban morphology and resulting urban shading and reflection. Tools such as CitySim and SORAM are specifically designed for urban-scale simulation and deploy high-fidelity 3D vector-based models that account for urban shading and reflection. Tools such as RADIANCE and Daysim are well known for their ability to provide a detailed simulation of indoor daylight environment in buildings, and require a high level of data inputs for modelling the geometry of objects in a building and associated surface properties for prediction of daylight distribution across indoor spaces. For PV system design, PV engineers use tools such as PVSyst to test the performance of a designed PV plant or designed PV systems on a building, and the tools offer users an option to consider shading on the designed PV module of interest due to nearby buildings. Among the software, the ones used for prediction of irradiance on urban surfaces at urban-scale rely on computationally heavy techniques such as ray-based and shadow-volume calculation (fundamentally requiring ray-interception). The current simulation software developed initially for different targeting applications are not suitable to effectively predict irradiance distributed over urban surfaces with proper consideration of complex urban morphology in dense urban areas.

Table 1. Current tools for solar analyses

Tools	Functionality	Radiation model type	Initial release	Latest update	Reference
Solei-32	Predictions of solar energy on tilted planes with different orientations and shadow from the surrounding topography	2.5 D	1993	No longer available online	Mészáros et al., 2002
SolarFlux	Predictions of total direct and diffuse radiation, direct sun duration, SVF and fisheye projections of sky obstructions	2.5 D	1993	No longer available online	Hetrick et al., 1993
RADIANCE	Light-backwards ray-tracing algorithm for prediction of direct radiation, diffuse and specular reflections from urban obstructions in a volumetric 3D model	3D	1994	2018	Ward, 1994
Daysim	Indoor daylight simulation tool powered by RADIANCE	3D	2000	2013	Reinhart and Breton, 2009
PVSyst	Predictions of the performance of different PV system configurations for design and evaluation of PV systems	Classic and 3D	1992	2018	Mermoud, 1994
EnergyPlus	Building energy performance simulation tool able to calculate irradiance on building surfaces with identified shading components	3D	2001	2018	Crawley et al., 2001
AutoCAD Solar Analyst (Ecotect)	Building performance analysis tool able to calculate irradiance/shading fraction/daylight hours on given surfaces with easy access and friendly interface	3D	2004	2015	Roberts and Marsh, 2001
ArcGIS Solar Analyst	An extension delivering a set of various radiation maps, fisheye equivalent photograph and a viewshed analysis	2.5D	1999	2018	Fu and Rich,1999

Table 1
(continued)

r.sun	Irradiance raster maps, reflectance and shadow maps for horizontal or inclined surfaces, fitting to overcast and clear-sky conditions	3D	1997	2013	Hofierka, 2002
DIVA	Daylighting and energy modelling plug-in for the Rhinoceros, using the SRA method with ray-tracing technique	3D	2011	2016	Jakubiec, 2011
CitySim	Energy simulation tool aiming at urban scale, able to calculated solar irradiance on building surface in a given time period	3D	2011	2015	Walter and Kämpf, 2015
Solar3DBR	Google SketchUp plug-in for shading factor and the irradiation determination on surfaces of 3D models	3D	2013	2013	Melo et al., 2013
SORAM (codes)	Predictions of direct and diffuse solar radiation incident on a sloping PV cell in an urban environment using ray-tracing technique	3D	Unavailable online		Erdélyi et al., 2014
Ladybug and Honeybee	Outdoor and indoor daylight simulation tool powered by RADIANCE	3D	2013	2018	Roudsari et al., 2013

2.2 Main features of the proposed models

Based on the identified limitations of current approaches at handling urban shading and reflection, this dissertation developed a simplified, physics-based method that allows the efficient modelling of the solar potential in urban areas. The proposed method consists of three model components: (a) two-segment sky discretisation method, (b) edge-angle-detection obstruction method, and (c) unified view-angle-based reflection method, as an improved alternative to the current standard methods. With the reflection of the urban context, the two-segment sky discretisation method allows for reducing the unnecessarily large number of sky

patches required for the prediction of irradiance on urban surfaces. Also, the edge-angle-detection method together with the view-angle-based reflection method can substantially reduce the number of iterations in the calculation process. Furthermore, the new method provides users with flexible control parameter settings related to the analysis setup for various requirements of prediction accuracy.

Figure 6 shows a process of predicting irradiance in urban areas using the proposed method. Three-dimensional urban geometry data is a key input to the proposed method. For a long time, obtaining three-dimensional urban geometry data has been a major obstacle for urban-scale simulations. Manual creation of an urban model is labour intensive, and model creation based on LiDAR requires expensive equipment and experts to collect and process the measured data. Alternatives are the growing databases of 3D urban models. For instance, simplified urban 3D models for UK cities are available in EDiNA (EDiNA, 2017). The proposed method is able to take in any 3D vector-based geometry, either processed from LiDAR or GIS or manually created in tools such as CAD or SketchUp. However, these models only provide geometric information, but do not provide information on the surface properties of buildings and roads, such as albedos, that impact reflected solar irradiance. Given that detailed information about individual urban surfaces will not be accessible in the near future, the proposed method uses two albedos: one for all buildings, and the other for all the roads. Other important inputs to the model are weather data, particularly direct normal incident (DNI), global horizontal irradiance (GHI), and dew point temperature data. These constitute typical weather data such as by TMY2. The all-weather sky model introduced by Perez et al. (1993; 1987) is used to predict sky diffuse radiance distributed over the skydome. With simplified urban geometry, surface albedos and weather data, the proposed model outputs direct sunlight radiation, diffuse skylight radiation, and irradiance reflected by the surrounding buildings. By accumulating the three outputs, the total solar irradiance received on any point-of-interest in a testing urban area is thus obtained. Sections 2.2.1, 2.2.2, and 2.2.3 provide a detailed description of the sky discretisation, obstruction, and reflection models, respectively.

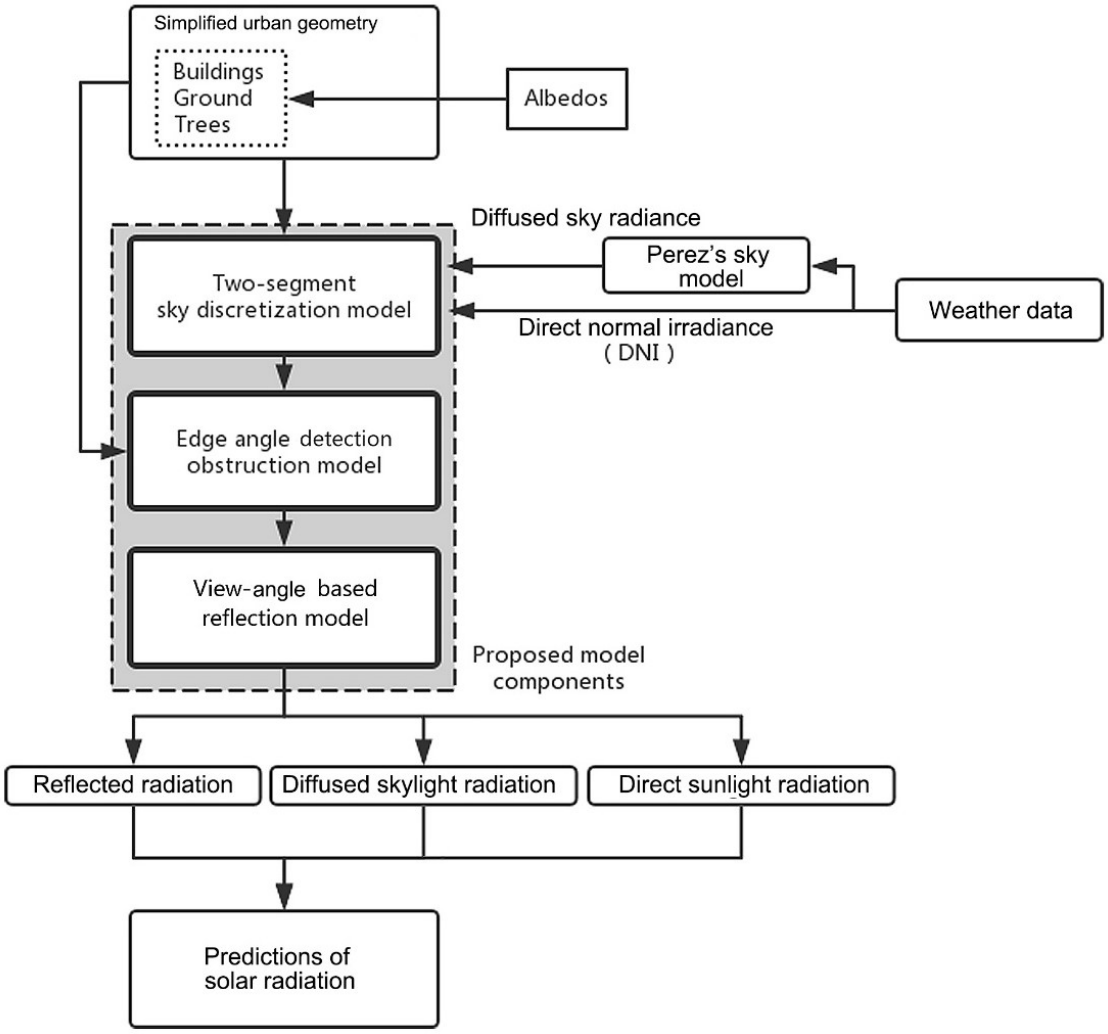

Figure 6. Structure of the proposed model.

2.2.1 Sky discretisation model

2.2.1.1 Current standard model

Existing irradiance simulation models use an anisotropic sky model, particularly the sky model proposed by Perez et al. (1987, 1993), to reflect diffuse solar radiance unevenly distributed over the skydome. The brightness of a specific point on the skydome in a sunny day depends on its relative position to the sun and the zenith of the sky. Sky discretisation techniques have been developed to capture the non-uniform distribution. The Tregenza method (Tregenza, 1987) is the most extensively used discretisation method in existing irradiance simulation models. The method divides the sky vault into 145 patches, and each patch has a relatively

equal area subdivided on the basis of 8 bands with an equal altitude width as illustrated in Figure 7. Any point within a similarly sized patch is considered as uniformly bright. The method was later recommended by the Commission Internationale de l'Eclairage (CIE) as a standard model for the purpose of a detailed daylight simulation. For cases where higher prediction accuracy is needed, a more refined sky model can be created on the basis of the same principles in Tregenza method; for instance, the tool Ladybug and Honeybee allows for creating a skydome with 577 smaller-sized patches, known as Reinhart Sky (Roudsari et al., 2013). It is stated in the tool Ladybug and Honeybee that increased discretisation will result in a considerably increased calculation time for the simulation. Several other proposals of sky discretisation also follow similar principles with different discretisation resolutions (Freitas et al., 2015).

In these methods, each altitude band must have a different integer number of azimuth segments to create all-sky patches with similar areas. As certain combinations of altitude and azimuth bandwidths are required in this approach, users do not have full flexibility to create different sky subdivisions tailored for their targeting applications. Alternatively, a triangle-based discretisation approach was developed by Song et al. (2002) for the projection of an equal-area global grid onto the sky. Schöttl et al. (2016) developed a triangle-based sky discretisation that reduces the computational load by pre-processing and identifying the visible sky nodes before the onset of the iterative calculation process. However, all these methods aim to discretize the entire sky dome in a uniform manner.

In urban areas, most buildings are considered solid masses built on the ground with varying heights as shown in Figure 7. Thus, it is very unlikely that parts of the buildings block only some patches in the middle of the sky, as illustrated in Figure 8 (left subfigure). Indeed, buildings typically obstruct the sky at various levels, starting from the ground level up to a certain height, as illustrated in Figure 8 (right subfigure). Hence, the existing methods that are based on uniform sky discretisation do not allow for efficiently representing the diffuse solar radiation of the unobstructed skydome with the use of the minimal number of sky patches required for reliable predictions. In fact, the number of sky patches used in the simulation

significantly impacts the computational efficiency, as the number of sky patches determines the number of calculation iterations required to assess whether each viewpoint has an unobstructed view to each sky patch on the dome. Alternatively, if the highest point blocked by buildings and projected on the sky is calculated first, all the sky patches vertically below the highest point are completely invisible, and all of the patches above are visible from this viewpoint. Therefore, there is no need to divide the obstructed sky dome into small-sized patches. As illustrated in Figure 9, the existing uniform discretisation methods create a substantial number of unnecessary sky patches.

Figure 7. Fisheye images of real urban obstructions in London(left) and New York (right)

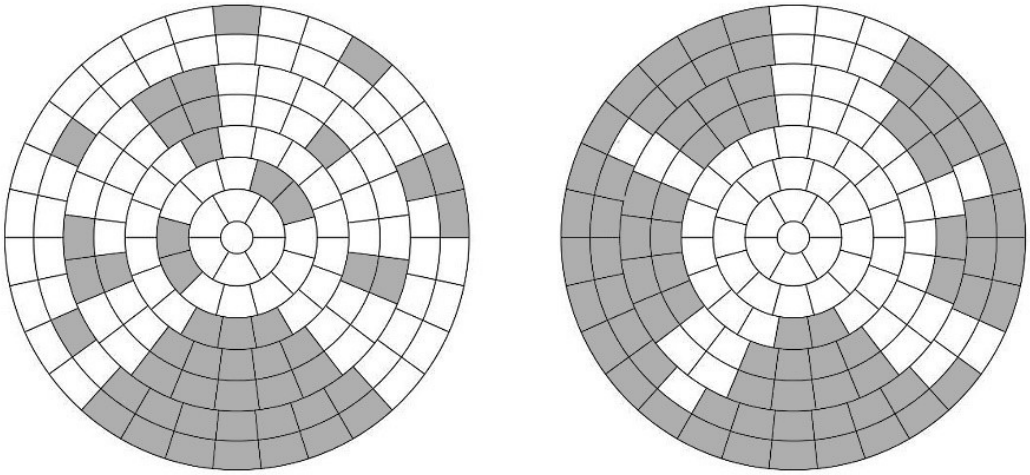

Figure 8. Unrealistic obstruction in the urban context (left) and realistic obstruction in the urban context (right).

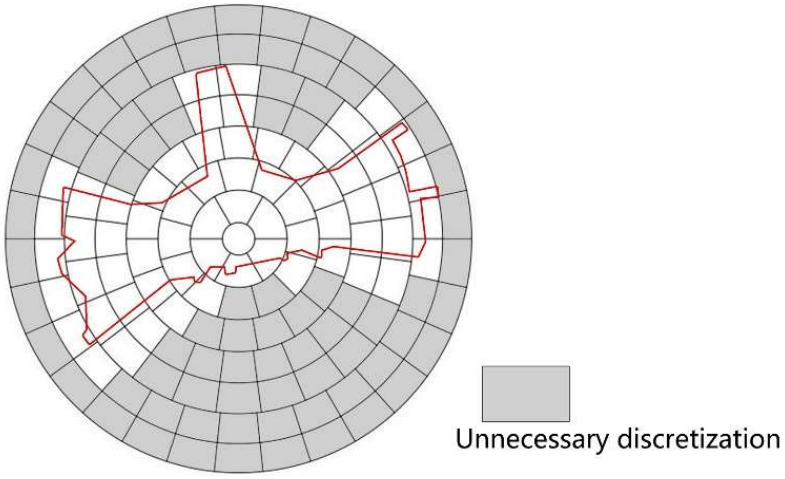

Figure 9. Lower sky patches do not need to be processed for obstruction.

2.2.1.2 Proposed model

As an alternative to the uniform discretisation method, this dissertation proposes a two-segment discretisation method tailored for irradiance prediction in urban environments. Given that buildings block the sky from the ground up to a certain level, depending on their heights, the proposed method divides one sky strip into two segments: one segment blocked by buildings (from the ground to the highest point of the buildings projected to the skydome), and another segment with an unobstructed view to the sky (from the highest point to the zenith of the sky), as shown in Figure 10. Accordingly, the proposed method does not account for daylight beneath elevated structures such as bridges and elevated streets and highways, and hence a small part of daylight coming underneath them is ignored in the proposed method. As a result, for viewpoints near the elevated structures, the proposed method may slightly underestimate the solar radiation received on the viewpoints. However, the impact of this limitation as small because infrastructures are usually elevated at a low level if elevated and available solar radiation beneath them may be already blocked by surrounding buildings in most cases. Daylight coming beneath treetops is more of a problem as trees are often present in a relatively low-density urban environment. In such case, if trees are modelled as solid geometry, daylight predictions may be underestimated to some extent. However, information about building details, detailed urban structures and trees are rarely available in the GIS data, and they are typically

ignored in urban-scale solar analysis.

In the proposed method, the skydome is divided into N number of strips, referred to as sky horizontal subdivision (SHS). On the basis of the same SHS applied to all viewpoints, the two-segment discretisation method calculates the altitude of the highest blocked point per sky strip for each viewpoint. As a result, each viewpoint may have a different pattern of two segments and consequently different sky view factor. In the proposed method, all-sky strips have the same azimuth bandwidth, $\psi = 2\pi/N$, and the sky view factor (SVF) of the i^{th} sky strip is defined in terms of the altitude of the highest blocked point on the corresponding sky strip, ξ_i, from a viewpoint as formulated in Eq. (1) below,

$$SVF_i = 1 - \sin\xi_i \tag{1}$$

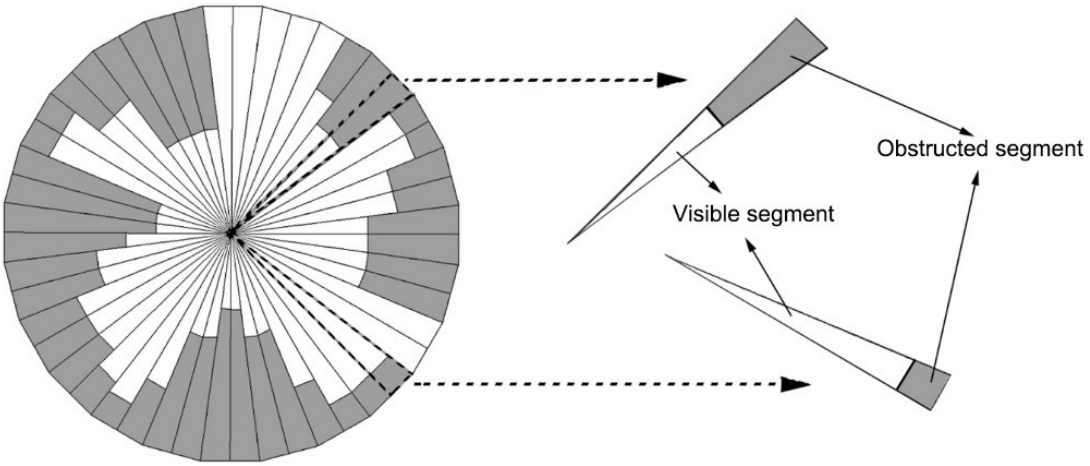

Figure 10. Two-segment sky discretisation method.

Figure 11 demonstrates the captured skylines using the proposed method with different SHS settings against Tregenza-based methods. All images were generated using angular fisheye projection for visualisation convenience. SVF values were calculated on the basis of orthographic fisheye projection for examining the accuracy of the proposed method in capturing surrounding buildings as obstacles. Although SVF is mostly useful for the isotropic sky model, it is still a useful indicator for evaluating the model performance of accurately representing the

visible sky. A viewpoint on the ground in a high-density area (Figure 11) was selected for the test. An image of the skyline viewed at the chosen location was rendered using RADIANCE (Figure 11a). Results of Tregenza-based methods were generated by a ray tracer based on Möller-Trumbore ray interception algorithm (Möller and Trumbore, 2005). Figure 11g shows that the accuracy of the captured skyline noticeably improved as the SHS setting changed from 24 to 500. With the SHS value of 80 (Figure 11d), the proposed sky discretisation method showed a good representation of the skyline, and with the SHS value higher than 120 (Figure 11e and 11f), the captured skyline was almost identical to the rendered image (Figure 11a). In terms of the calculated SVF, the absolute error decreased from 0.026 to 0.006 as SHS increased from 24 to 120. For Tregenza-based methods, the absolute error of SVF is 0.019 and 0.005 for 145-subdivided sky (Figure 11h) and 577-subdivided sky (Figure 11i), respectively. This comparison highlights that the proposed method was able to obtain more accurate results with a SHS value of 40 than the standard Tregenza sky with 145 subdivisions. In addition, the concept of SHS gives users an easy control and high flexibility of assigning any intended resolution to the sky as long as SHS is set as an integer number, while Tregenza-based method follows a more complicated subdivision scheme that offers users limited options such as Tregenza 145 or 577 sky subdivision.

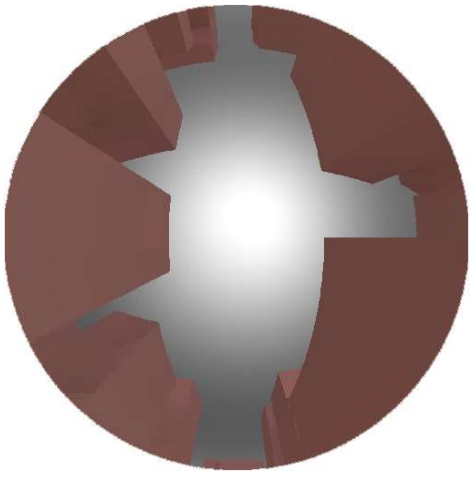

(a) Rendered skyline; SVF value: 0.396

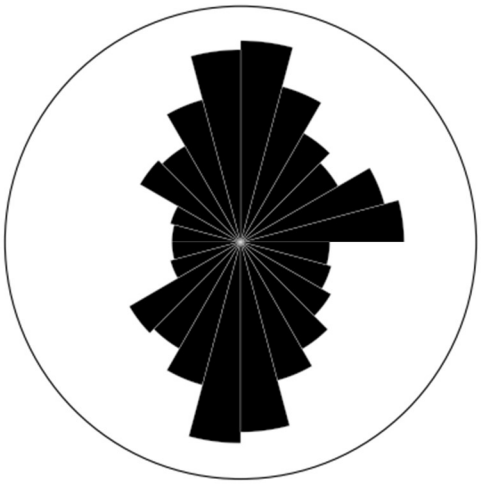

(b) SHS: 24; SVF value: 0.372

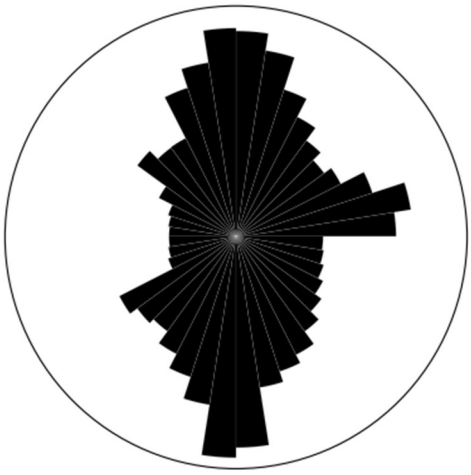

(c) SHS: 40; SVF value: 0.385

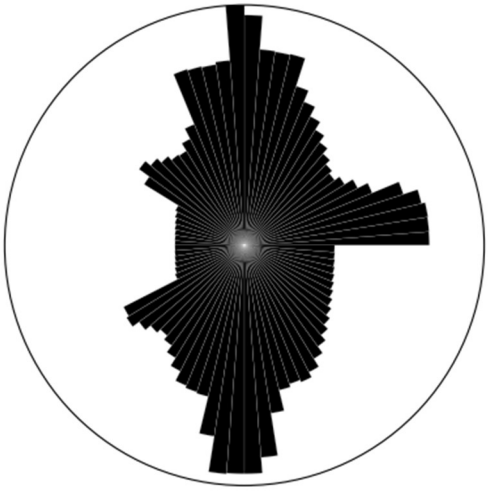

(d) SHS: 80; SVF value: 0.390

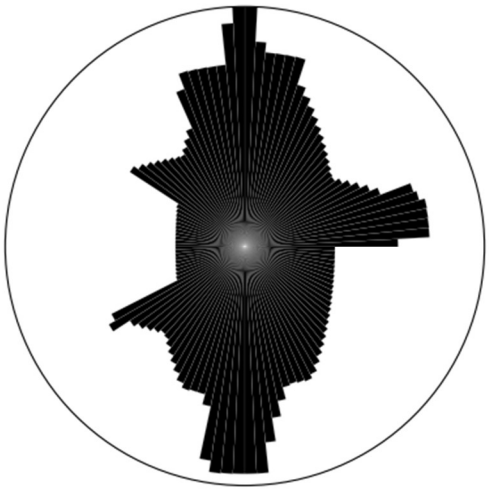

(e) SHS: 120; SVF value: 0.392

(f) SHS: 500; SVF value: 0.396

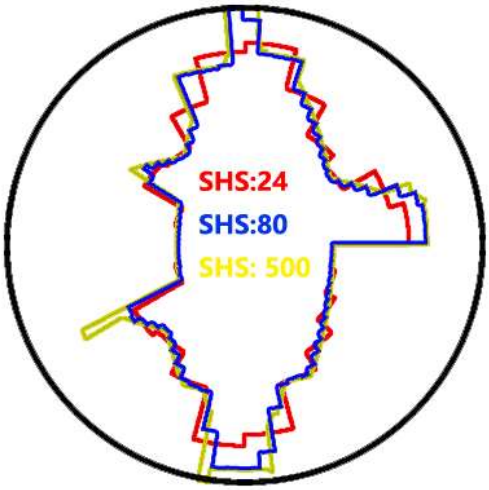

(g) Overlap of three captured skylines

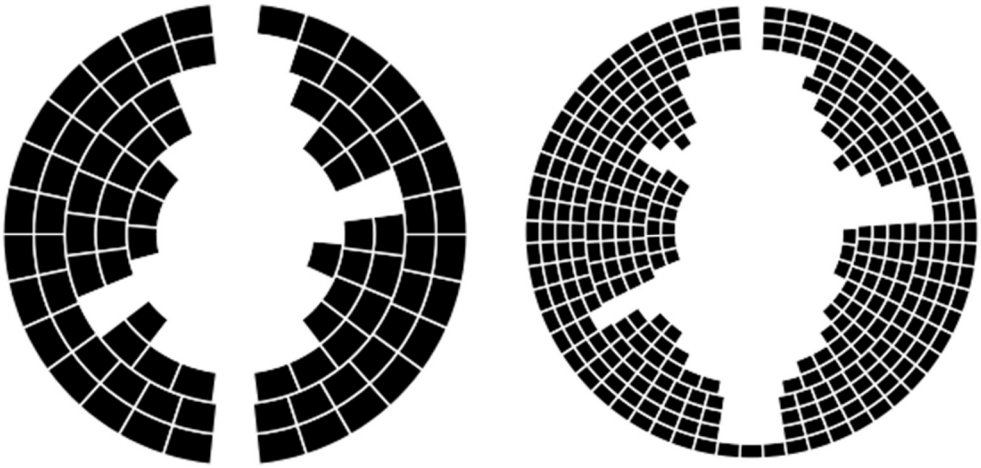

(h) Tregenza 145 subdivision; SVF value: 0.379

(i) Tregenza 577 subdivision; SVF value: 0.391

Figure 11. Captured skylines using the proposed method with different SHS settings against Tregenza-based methods

For dense urban areas in which many buildings have different heights, one may need to increase SHS to correctly capture the obstructed skyline at the expense of increased computational costs. Instead of increasing SHS, the proposed method includes an optional step that calculates an average altitude of the highest blocked point and SVF per sky strip subject to the consideration of varying building heights within one sky strip. This step further subdivides each sky strip into *K* number of slices. Here, *K* is referred to as the strip inside the subdivision (SIS). The highest block point of the i^{th} sky strip is given as,

$$\xi_{\text{avg},\,i}=(\sum_{j=1}^{K}\xi_j)/K \tag{2}$$

and the average SVF of the i^{th} sky strip is defined by,

$$SVF_{avg,i} = (\sum_{j=1}^{K} SVF_j)/K \tag{3}$$

SIS was introduced to make the proposed method with a relatively low SHS capture a more accurate representation of the skyline. SVF results shown in Figure 11 are based on

different SHS values and the fixed SIS value of 3. To demonstrate the effects of SIS, another viewpoint in the relatively high-density area was selected. Figure 12 exhibits the captured skylines with the same SHS value of 40 and varying SIS values set at 1(Figure 12a), 2 (Figure 12b) and 3 (Figure 12c). As it is hard to see differences among different SIS settings at first glance, key differences in the results were highlighted in three locations. It was observed that an increase in the SIS settings helped correct a sudden change of skyline. Especially, when the SIS changed from 1 (indicating no SIS) to 2, the absolute error significantly improved from 0.053 to 0.025 and further improved to 0.014 when SIS was set at 3.

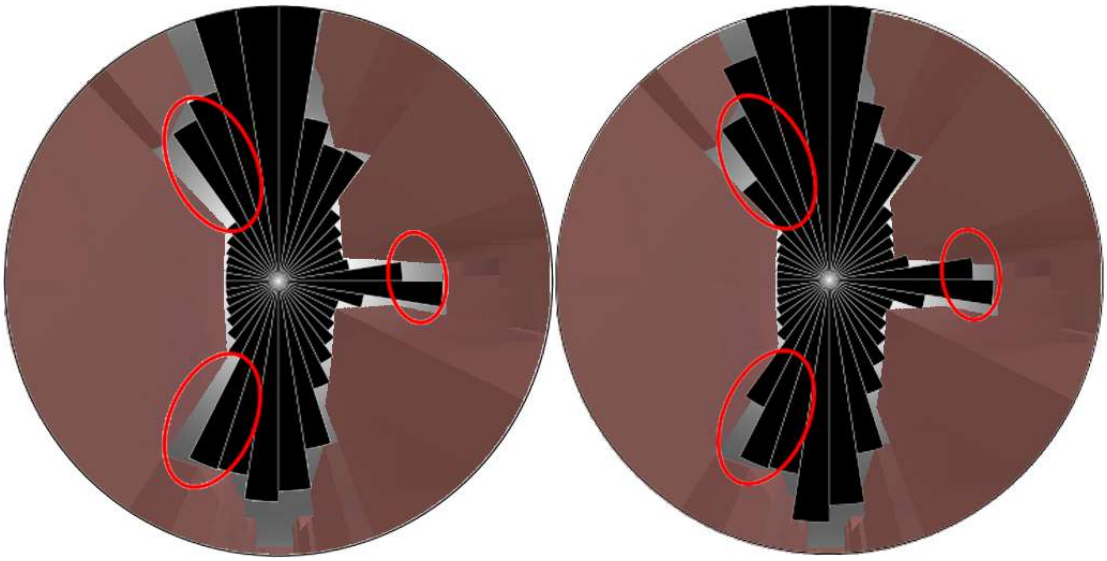

(a) SIS: 1 (no SIS); SVF value: 0.270 (b) SIS: 2; SVF value: 0.298

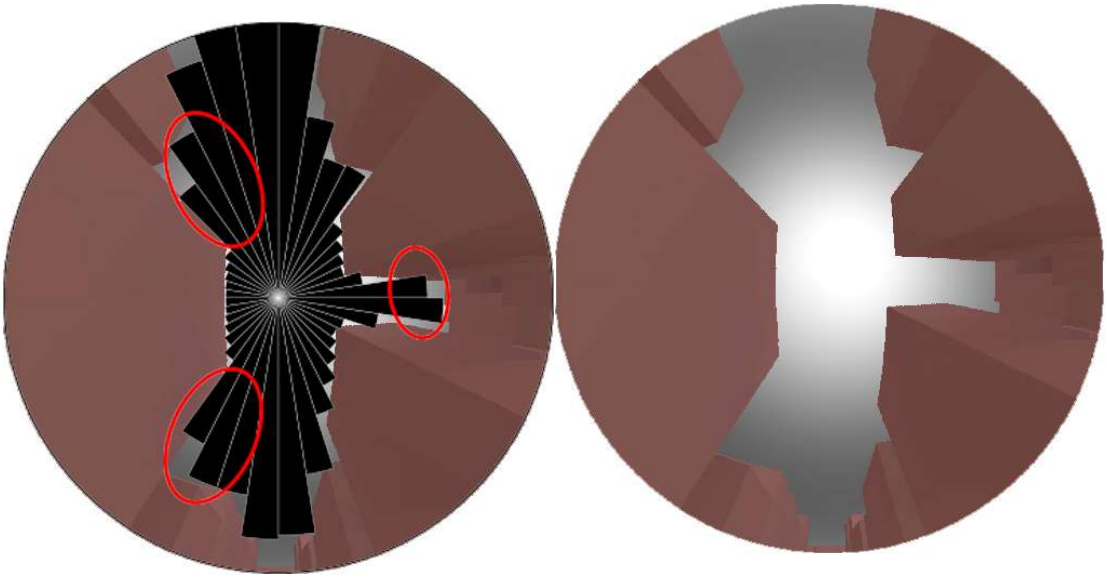

(c) SIS: 3; SVF value: 0.309 (d) Rendered skyline; SVF value: 0.323

Figure 12. Captured skylines using the proposed method with different SIS settings against

the rendered image.

For the calculation of the non-uniform irradiance received from the visible sky, each sky strip is assigned to *M* sampling points, referred to as sky radiance sampling subdivision (SRSS) as shown in Figure 13. A higher setting of SRSS leads to a higher resolution of vertical subdivisions for each sky strip. Different from Tregenza-based methods, the SRSS is a semi-independent subdivision in relation to SHS. Although the azimuth bandwidth is pre-determined after SHS is decided, it is completely up to the user to determine the number of SRSS along each sky strip. With a defined SRSS, each sampling point is given one single sky radiance value calculated by the Perez (1993, 1987) all-weather sky model. Each SRSS point represents a sky patch with a uniform radiance. For example, radiance sample points shown in Figure 13 are based on the SRSS value of 8 and the SHS value of 36. Only visible sampling points that fall within unblocked segments are selected for further skylight calculations. A higher SRSS setting discretises the visible sky into more patches and, therefore, more accurately captures the variation of the anisotropic sky. Each received diffuse sky irradiance from the selected q^{th} SRSS sampling point on the i^{th} sky strip, $G_{diff,q,i}$, can then be calculated on the basis of (Robinson and Stone, 2004),

$$G_{diff,q,i} = R_{q,i} \cos(\alpha_{diff,q,i})(\sin\phi_{up,q,i} - \sin\phi_{low,q,i})\, \psi \quad (4)$$

where $R_{q,i}$ is the sky diffuse radiance of the sampling point calculated by the Perez model (Perez et al. 1993, 1987), $\alpha_{diff,q,i}$ is the incident angle between the normal at the viewpoint and the q^{th} sampling point, ψ is the azimuth bandwidth of sky strips described previously, and $\phi_{up,q,i}$ and $\phi_{low,q,i}$ are the altitude of the upper and lower bounds of each patch where one sampling point is positioned. For the patch where the highest blocked point falls into, the lower bound altitude ϕ_{low} equals to the altitude ξ_i of the highest block point. A received surface is discretized into a grid depending on the size of the grid set by users. Then, each point in a grid is an individual viewpoint in which received radiation is calculated. The case study in the later section used a 3 meter ×3 meter grid to calculate the total direct irradiance of individual urban surfaces.

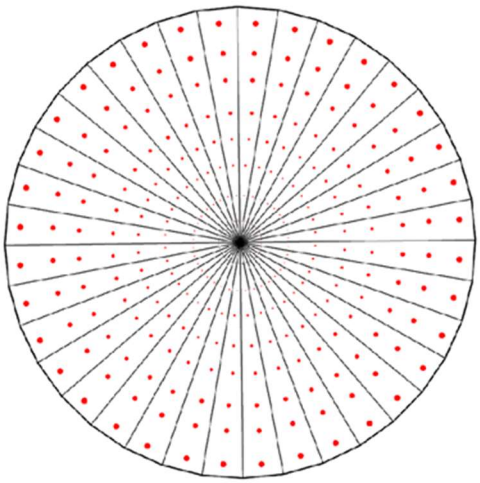

Figure 13. Illustration of radiance sampling points of the proposed method.

Direct sunlight on a viewpoint is calculated by first checking whether the sun is visible from that viewpoint. If the solar altitude is higher than the altitude of the highest blocked point on the sky strip in which the sun is located, direct irradiance is calculated by,

$$G_{direct} = \cos(\alpha_{direct})\, G_{DNI} \quad (5)$$

where G_{DNI} is the direct normal irradiance derived from the weather data, α_{direct} is the incident angle between the direct beam and the normal at the viewpoint.

One of performance indicators often used for solar potential analysis is the total solar energy harvested during a certain period of time (e.g., monthly or annual). One way to obtain aggregated solar energy production is to run the simulation for each time step (e.g. hourly) given the weather data and then accumulate hourly results for a final outcome. Alternative way is to pre-process the sky diffuse radiance to output a cumulated sky radiance map. By doing so, only one iteration of final calculation is required and thus reduces the computational load. By using this approach, existing daylight simulation enhances the computational efficiency, and so does the proposed method. The proposed method can be easily integrated with a cumulative sky model to further enhance the computational efficiency.

2.2.2 Obstruction model

2.2.2.1 Current standard model

The ray-tracing method has been commonly used to detect surfaces that obstruct daylight, starting from either the light source (forward raytracing) or from the view point (backward raytracing). This method relies on the ray intersection algorithm (Möller and Trumbore, 2005). In analytic geometry as an example shown in Figure 14, the ray intersection algorithm detects the intersection between a line drawn between a specific viewpoint to a target area and a plane (i.e., potential obstruction) by computing a) the empty set (i.e., indicating the absence of any intersections), b) a point (i.e., where intersection occurs), or c) a line (i.e., the case at which the ray and plane are parallel such that they do not intersect). An alternative is the radiosity method that does not account for specular reflections (i.e., it only handles diffuse reflections) to reduce the computational load of tracing specular reflections. However, ray tracing or ray interception technique is still necessary to determine whether a viewpoint can see a sky patch of interest. For example, the image-based approach using rendered fisheye image was applied to check obstruction at the viewpoint (Grimmond et al., 2001), but rendering images essentially require ray tracing. Another more practical technique is using the ray interception method. In this method, the total number of ray interception iterations equals to the number of viewpoints multiplied by the number of potential obstructed surfaces, and further multiplied by the number of sky patches. Figure 15 on the left side illustrates the basic concept of the ray interception method. As ray interception can take up to 95% of the total simulation time (Amanatides and Woo, 1987), it is not an efficient calculation approach for large-scale problems.

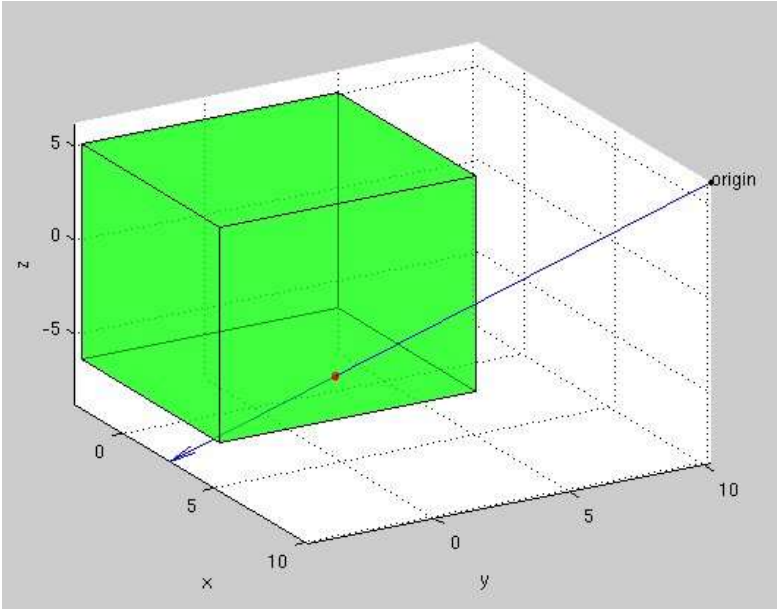

Figure 14. Illustration of ray interception between a ray with origin and a surface on an object of interest.

2.2.2.2 Proposed model

As an alternative to the ray-tracing method or shadow calculation algorithm, this dissertation proposes a computationally efficient approach that identifies and computes the highest blocked point in buildings from a specific viewpoint. Figure 15 (right-subfigure) illustrates the basic concept of the proposed method in comparison with the ray interception approach (Figure 15 left-subfigure). First, building edge lines are divided by building edge subdivision (BES) in terms of the distance between subdivided points. For example, if BES is set at three, there will be a subdivided point every three meters along the building edge. After calculating all the altitude angles of the subdivided points from the specific viewpoint under consideration, calculated angles are grouped for each sky strip. For the i^{th} sky strip, the highest block-point altitude, ξ_i, is the maximum value of the i^{th} group of angles. Similarly, the lowest block-point altitude of the i^{th} sky strip, β_i, is the minimum value of the group, which will be used to calculate the reflected radiation in the next section. The proposed method requires a much smaller number of calculation iterations than the ray intersection method given that the required number of iterative calculations for the proposed method is the product of the number of viewpoints and the number of subdivided points. Furthermore, the proposed method allows

users to flexibly set up (adjust) the subdivision level.

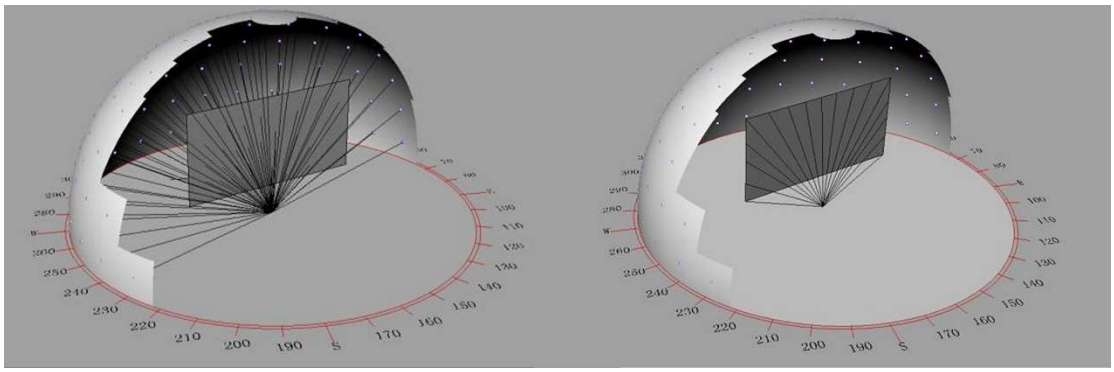

Figure 15. Ray interception method (left) and edge angle detection method (right).

The resolution of BES should be paired properly with SHS, meaning that a high setting of SHS requires a relatively high resolution of BES. If the sky is subdivided into a high number of strips, each sky strip's azimuth bandwidth is small. If the BES setting is not high enough for that SHS setting, it may lead to some building edges not being properly recognized as there is no BES point projected onto some sky strips. Figure 16 shows such error due to the mismatch in the two settings as an example. Figure 16 (left-subfigure) demonstrates the result of sky obstruction with setting SHS at 180 and BES at 1 meter. It was observed that one building edge was broken due to several missing BES points. By increasing the resolution of BES to 0.5 meters, this problem was solved (Figure 16 right-subfigure). But, it should be noted that this example used a very high number of SHS to demonstrate the potential problem and a much lower SHS was found to be suitable for dense urban areas as shown in the case study in the later section. In order to avoid misrepresentation of sky obstruction, different pairings of SHS and BES was examined in various viewpoints, and recommended BES settings are given in Table 2 according to the SHS setting.

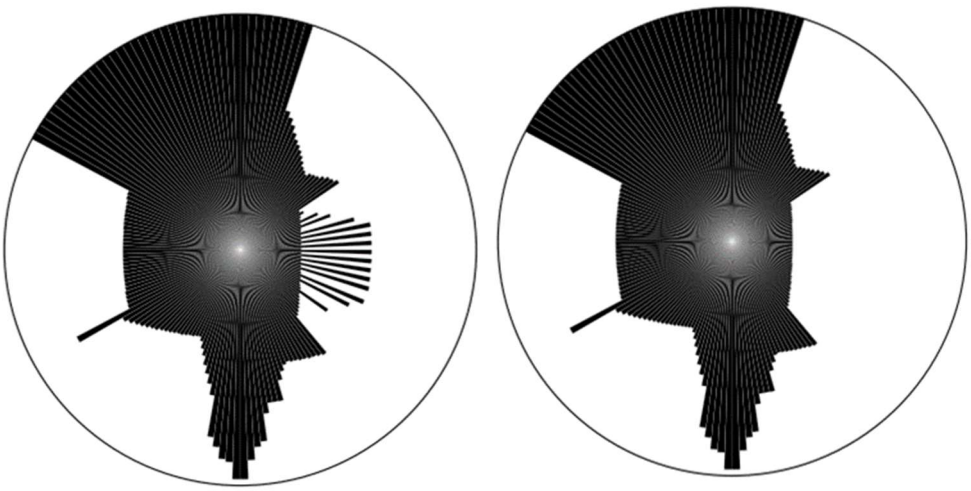

Figure 16. Misrepresentation of sky obstruction (left); proper representation of all building edges (right).

Table 2 Recommendations of recommended BES settings according to the SHS setting.

SHS	< 24	24 – 40	40 - 80	80 – 200	> 200
BES (meters)	< 8	< 5	< 3	< 1	< 0.5

2.2.3 Reflection model

2.2.3.1 Standard model

In urban areas, building surfaces and roads reflect both direct beams and diffuse radiations. In the commonly used backward ray-tracing method, multiple rays are sent out from a viewpoint tracing back to light sources (e.g. the skydome), and if a ray hits a surface, then more rays are generated from the hit point to compute the amount of reflected radiation. This computationally aggressive "bouncing" process is repeated until a certain satisfying convergence is achieved. Robinson and Stone (2004) developed a simplified radiosity algorithm (SRA) based on the assumption that surfaces are Lambertian. Since the radiosity method only handles diffuse reflections, the need for propagating reflected specular rays at exponential growth is avoided. Although SRA substantially reduces the number of iterations in the reflection calculation, this simplified method is still computationally demanding as it iteratively detects where reflection takes place on every surface. On the other hand, existing research showed evidence that prediction improvement from calculating multiple inter-reflections may not be substantial for solar analysis in urban environment. One recent study

(Waibel et.al., 2017) examined the effects of specular reflection bounces in urban environments with multiple test points sampled on every surface of a case building in Zurich, Switzerland using computational simulations. The study showed that on average, less than 5W/m^2 differences were observed, and up to 20W/m^2 marginal differences were observed in comparison to the annual value of around 250W/m^2. It is worth mentioning that errors due to ignoring multiple-bounce reflections might be higher for urban areas with a significant amount of glazed buildings. Additionally, north-facing surfaces located in an urban canyon may likely receive more reflected daylight from the opposite buildings with relatively high reflective surfaces, and the error for north-facing surfaces is likely to be higher particularly for cities in warm dry climates. Additionally, high-fidelity simulation of reflection does not guarantee accurate results for urban-scale solar analysis as detail information about individual surface properties (e.g. albedos) is usually unavailable and urban-scale applications often apply the assumed surface properties to all building surfaces. Using building typologies for classifications according to building age, form and function might provide more information about variation in surface properties.

2.2.3.2 Proposed model

The proposed method follows the methodology formulated in the previous study by Robinson and Stone (2004) that assumes that all surfaces are Lambertian. In addition, two major simplifications are implemented in the proposed method. First, the proposed method uses only two average solar reflectance values: one for all building surfaces and the other for ground surfaces. Second, only solar irradiances reflected in the first bounce are considered. Based on these major assumptions, reflected irradiance can be calculated simply by using the solid angle to the buildings and the ground. The concept of the building's view angle (BVA) and ground view angle (GVA) is illustrated in Figure 17.

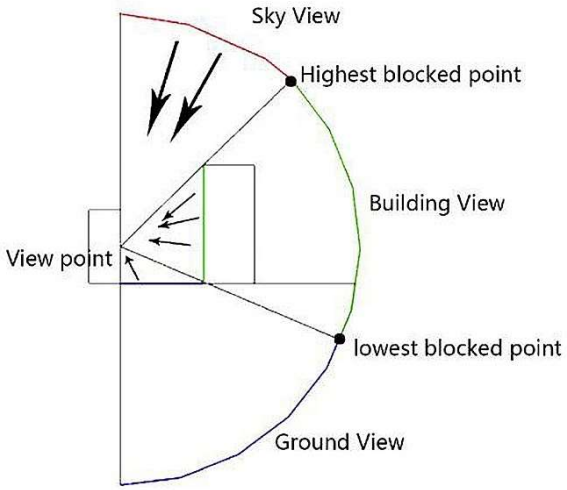

Figure 17. Illustration of the use of building and ground view for the calculation of reflected radiation. (Image adapted from Liao and Heo, 2017)

BVA and GVA are defined as the solid angles of a particular viewpoint to either the building or ground surfaces, respectively. In the i^{th} sky strip, BVA_i and GVA_i are given as,

$$BVA_i = 2\pi N \left(\sin(\xi_i) + |\sin(\beta_i)|\right) \quad (6)$$

$$GVA_i = 2\pi N \, |\sin(\beta_i)| \quad (7)$$

where N is the SHS, and ξ_i and β_i are the altitudes of the highest and lowest blocked points on the i^{th} sky strip, respectively. Once the *BVA*s and *GVA*s are obtained, the proposed method calculates the reflected irradiance based on the following three-step process. First, average reflectance values are estimated for buildings (ρ_b) and for the ground (ρ_g) on the basis of a general observation of a case study area. It would be ideal to obtain the measured albedos of all buildings inside the case area. However, as such a detailed level of data is usually unavailable, measured surface albedos for certain types of buildings in the case area can be useful to estimate an average albedo value for buildings. Second, the first-received irradiance on every sampling point of building and ground surfaces is calculated. For example, in the case study described in Section 3, the study used a 3 meter × 3 meter grid on every surface of all urban surfaces, which was used as the grid for the entire analysis process. By doing so, the method avoids creating a separate grid for calculating first received irradiance. In this step, the first-received irradiance

of each sampling point is then calculated by adding received skylight from equation (4) and received sunlight from equation (5), denoted as $R_{b,i}$ and $R_{g,i}$, respectively, for the i^{th} sky strip. Then, the method calculates a view angle to the buildings and ground, BVA_i and GVA_i, for the i^{th} sky strip to calculate the amount of reflected irradiance from the surroundings viewed by the sampling point. The first-received irradiance $R_{b,i}$ on the nearest building surface to the viewpoint of interest for the i^{th} sky strip is then passed on to calculate first-bounce irradiance. If there are multiple sampling points on the nearest building surface, an average $R_{b,i}$ of all the sampling points on that surface is used as the first-bound irradiance of the surface. It is computationally convenient to identify the nearest surface as the distance array was generated as a by-product from calculating view angles using the BES technique and there is no need for another iteration of distance calculation. As the unified view-angle based method accounts for all urban surfaces to calculate the building view angle, it is likely to cause overestimation of received diffuse reflected irradiance if there is a very tall building in distance from a view point. However, in most relatively dense urban areas, building-view angles for a view point is likely to dominantly depend on surrounding buildings near the view point. The total first-bounce irradiance reflected to a viewpoint from buildings $G_{building,i}$ and that from the ground $G_{ground,i}$ for the i^{th} sky strip are then formulated as,

$$G_{building,i} = R_{b,i} BVA_i \cos(\sigma_b)\rho_b \tag{8}$$

$$G_{ground,i} = R_{g,i} GVA_i \cos(\sigma_g)\rho_g \tag{9}$$

where $\sigma_{b,i}$ and $\sigma_{g,i}$ denote the angles between the normal at the viewpoint and the line which connects the viewpoint to the centre point of the building and the ground view, respectively, for the i^{th} sky strip.

Because the proposed method considers only one bounce of reflection, it may likely underestimate the reflection prediction. Given that reflected irradiance is commonly considered as much less than the directly received irradiance, several research studies (Redweik et al., 2013; Lindberg et al., 2015) also used the one-time reflection approach for ground reflection and

ignored reflections among buildings completely. Lindberg et al. (2015) compared their model outputs against measurements and showed a good agreement between predictions with considering only one-time reflection and measurements. Studies above suggest the relatively limited impact of adopting one-time reflection assumption on the prediction accuracy.

2.3 Surface subdivisions

Partial shading is one key problem when it comes to predicting solar potential on a large surface, such as an entire building façade. Partial shading refers to the uneven distribution of solar radiation caused by the changing Sun path and the relative position of a receiving surface against a daylight obstructer, such as the opposite building across a street. The method follows a standard procedure of surface subdivision where a surface of interest is divided into patches in a grid form. At each centre point of a subdivided patch is where the proposed method can be applied to calculate the received solar irradiance (W/m2) accordingly. The predicted received solar irradiance on each patch is then assumed to be the same as that of its centre point. Here, the centre points act as sampling test points and the density of the test points on a surface can be determined by a user. A higher density of sampling test point gives a more accurate prediction in terms of reflecting the variation of received solar irradiance on a surface. The study uses 3 *3 meters grids on all the buildings in the latter case studies in Chapter 3 and Chapter 4. Figure 18 shows the prediction of the annual solar radiation in an urban case visualised by using the software Grasshopper as an example. The density of 3*3 grids properly reflects the variation of received solar energy within a building façade in such a case.

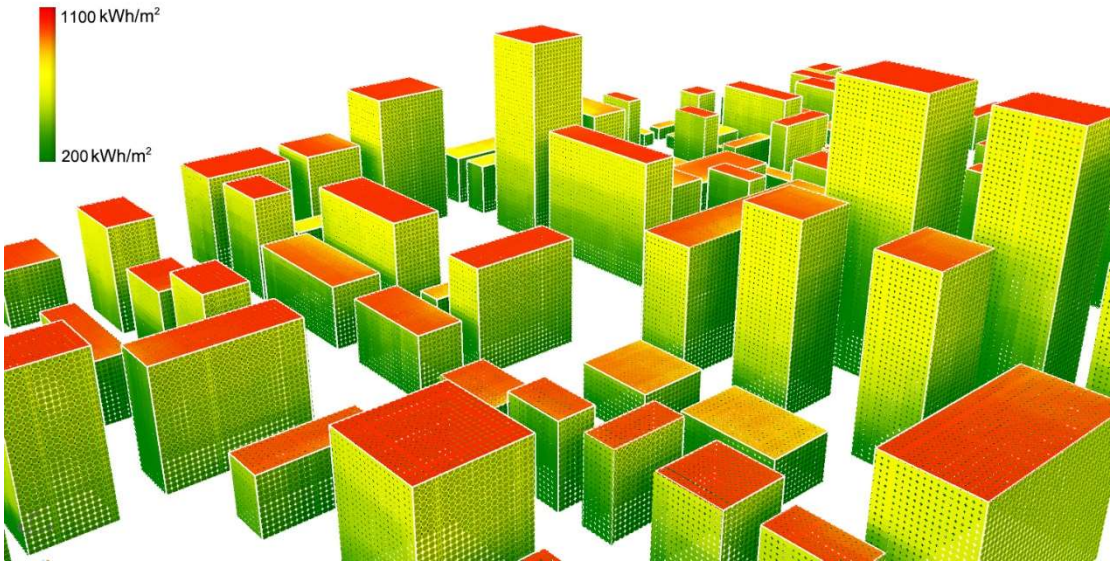

Figure 18. Visualisation of the annual prediction of received solar radiation based on a surface subdivision in 3 *3 meters grids.

2.4 Implementation

The method was implemented in the programming environment of Python 2.7. In this section, key steps in the implementation of the proposed method are described.

In the first step, urban 3D geometry consisting of building surfaces and ground surfaces in the form of .obj file are imported to create an 2D array that stores all the information of surfaces as vertices and their normal vectors. Then, a surface subdivision is carried out where all the surfaces are divided into patches in a grid form where the density of the grids in the unit of meter can be set accordingly, such as 3, 5 or 10, meaning a 3m * 3m, 5m * 5m and 10m * 10m mesh grid, respectively. The new sets of the centre points of the grids are then stored in a new 2D array that will be used as the points where solar irradiance was calculated for. Building edge subdivision is also carried out in this process where a new set of 2D array is created to store all the vertices of the subdivided BES points given the setting of BES in the unit of meters, such as 3,5 or 10, meaning one BES point every 3 meters, 5 meters and 10 meters, respectively. Next, the proposed sky discretisation method was implemented where the sky horizontal azimuth boundary is stored as a 1D array for each sky strip given the setting of SHS and SIS. After the sky strips are defined, Perez all-weather sky model is then implemented given the

imported hourly weather file in the .txt format, the imported geographical location as longitude and latitude, and the defined time period for calculation. An accumulated skydome technique is used where only one radiance skymap is created by accumulating the calculated hourly sky radiance by Perez model into each SRSS point given the setting of SRSS and the previously generated sky discretisation 1D array. Following that, we now have a new 2D array that stores the brightness (i.e. radiance) for each SRSS point given in each sky strip and its sky horizontal altitude.

Given the above processing, we now have three key sets of 2D array that stores the information of sky brightness, surface subdivision centre points and BES points. Next, the proposed obstruction model is implemented where each surface subdivision centre point is looped to calculate their angles to each BES points. In the process, the identified highest blocked point and lowest block points are stored as sky altitude angles for each surface subdivision centre point in a new 2D array sorted by each sky strip. Then, SVF, BVA and GVA and their according solid angles are calculated using the stored sky altitude angles. Next, the first received solar irradiance is calculated by accumulating the radiance from all the visible sky SRSS points determined by the SVF, and a 2D array is created to store the first received irradiance for each surface subdivision centre point. In the final step, the proposed unified view-angle based method is implemented by looping each surface centre point for their received first-bounce irradiance given the BVA and GVA for each sky strip. The final results are then stored in a 2D array where each surface subdivision centre point is paired with its first received irradiance, first-bounce irradiance (i.e. received reflected irradiance) and the sum of the two.

Besides the implementation of calculating the accumulated solar energy given a period of time, if the hourly prediction is required, there is no need to calculate the obstruction map since the method calculates the SVF, BVA and GVA first hand and therefore it is time efficient for calculating hourly prediction using the proposed method as well.

2.5 Summary

The chapter identified limitations of current standard approach at handling urban shading and reflection, the study then developed and presented a simplified, physics-based method that allows the efficient modelling of the solar potential in urban areas. The proposed method consists of three model components: (a) two-segment sky discretisation method, (b) edge-angle-detection obstruction method, and (c) unified view-angle-based reflection method, as improved alternatives in regard to the current standard models.

With the reflection of the urban context, the two-segment sky discretisation method is supposed to reduce the unnecessarily large number of sky patches required for the prediction of irradiance on urban surfaces. Also, the edge-angle detection method together with the view angle-based reflection method could substantially reduce the number of iterations in the calculation process. The new method also provides users with a flexible control parameter setting related to the analysis setup, including Sky Horizontal Subdivision (SHS), Strip Inside Subdivision (SIS), Sky Radiance Sampling Subdivision (SRSS), and Building Edge Subdivision (BES) for various requirement of prediction accuracy. Compared to the standard Tregenza sky discretisation model at two different resolutions, the tested two-segment sky discretisation more accurately captured the urban skyline with less required number of discretisation. The optional SIS setting can better capture the sudden change of skyline while keeping the same number of required discretisation SHS and therefore avoiding unnecessary computational load. The resolution of BES should be paired properly with SHS to avoid possible misrepresentation of the skyline. A range of pairing resolutions of the two settings was suggested and given in the chapter. The chapter also demonstrated the suitability of the procedure of surface subdivisions in use with the proposed method. Key steps of the implementation of the proposed method were described.

Chapter 3: Model validation

3.1 Model validation framework

This chapter investigates the performance of the proposed model in comparison to both high-fidelity simulation results and measurements from controlled experiments. Two sets of comparisons were designed using the urban area which spans 0.72 km^2 (1.2 km×0.6 km), located in the Hankou district in Wuhan, China. Figure 19 illustrates the model validation framework on the basis of the two sets of comparisons. First, the predictions of the proposed method were compared against those of the existing high-fidelity simulation tool RADIANCE. An urban geometry model of the study area was generated and used for both the proposed model and RADIANCE with the input of a Chinese standard weather data (CSWD) created by the China Meteorological Bureau (China Meteorological Administration, 2018). Second, irradiance predictions by the proposed method were compared against measurements from physical experiments. Two sets of physical micro urban models of the selected urban area were designed and constructed to collect data during the summer in 2017 in Wuhan. The collected solar measurements with quantified measurement uncertainties were used to validate the proposed method. On-site weather data were carefully collected and used as the weather input for

simulation. In addition to the prediction accuracy, the computational performance of the proposed model was also tested against the standard ray interception algorithm.

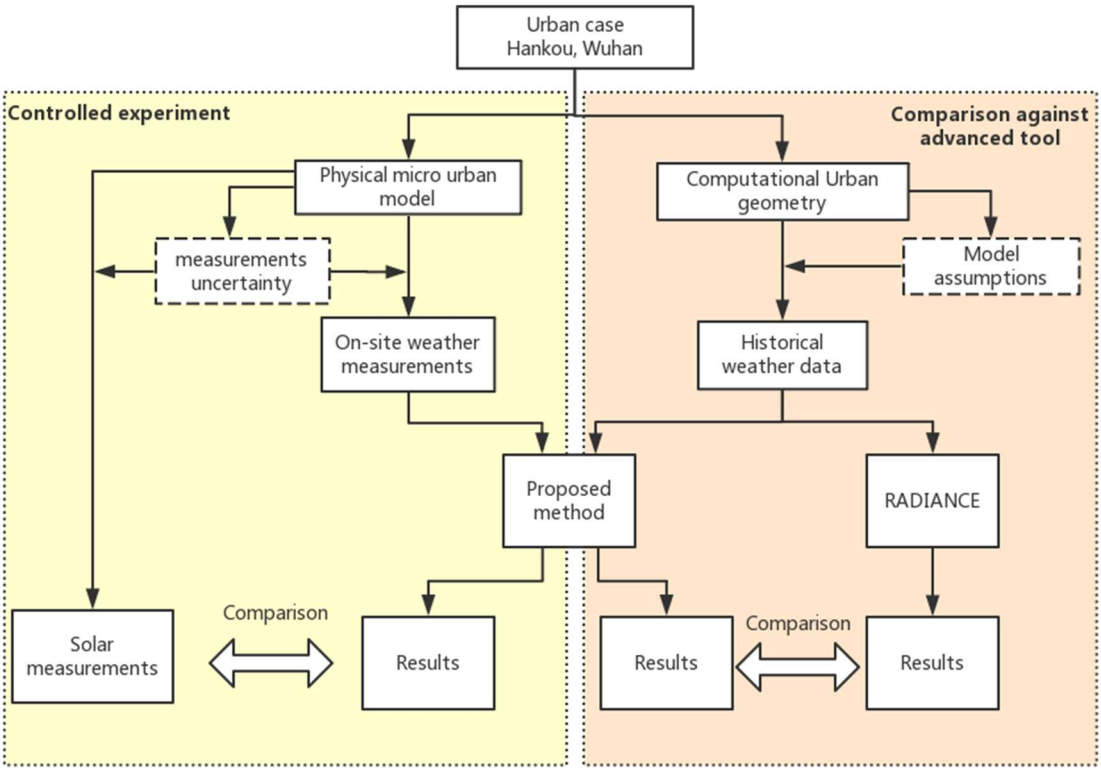

Figure 19. Framework of the two comparisons in the study

3.2 The studied urban area

The studied area is part of a city area that spans 0.72 km^2 (1.2 km×0.6 km), located in the Hankou district in Wuhan, China, as shown in Figure 20. This area is part of the city centre of Wuhan where a mixture of commercial, office and residential buildings exist. Building heights and sizes vary significantly in the studied area, creating complex urban shading and reflecting effect. This urban area represents a commonly seen urban landscape in major cities in Asian countries and is used as an example of medium-to-high density urban environment.

The computational urban model of this urban area was constructed based on the urban data provided by Wuhan Planning and Design Institute and Google Map. As the GIS data of Wuhan is not currently well developed like most of the Chinese cities, on-site visits were also carried

out to help achieve a better representation of the real urban environment. The resulting urban geometry data were used for the proposed method, RADIANCE and controlled experiments. Figure 20 shows three locations chosen in terms of the relative urban density in the studied area for comparison of the proposed model against RADIANCE. Locations in the studied area used for comparison against measurements are different and will be described in Section 3.4.1.

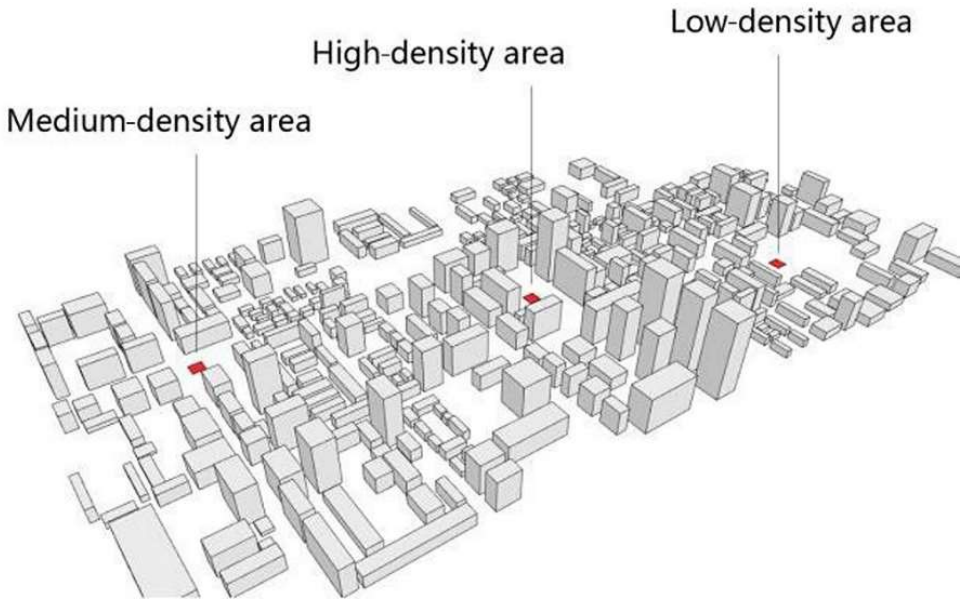

Figure 20. Studies area indicating the three tested locations.

3.3 Comparison against RADIANCE

In the comparison against RADIANCE, Ladybug and HoneyBee were used to create an urban model and predict solar radiation on the three tested locations with different urban densities, as shown in Figure 20. In each location, a flat plane was used at different tilted angles to generate accumulated irradiances during the test hours (8:00 am to 4:00 pm). The sizes of the flat planes were identical and set to be 20 m × 20 m, and the accumulated radiation during the test hours was calculated by averaging the solar radiation of 36 test points spaced by a 3 m × 3 m grid. All building envelopes and ground albedo values were set to be 0.2 and 0.1, respectively, for both the RADIANCE and the proposed model. The CSWD weather file was used to provide hourly direct and diffuse radiation and dew-point temperature data. March 1st was selected as a simulation period as this day presents both direct and diffuse daylight with changes within a day while representing typical weather conditions as shown in Figure 21. A

RADIANCE simulation setting was made “medium” defined by Ladybug and Honeybee with the following parameter settings: number of ambient bounces = 3; ambient divisions = 2048; ambient resolution = 64; number of ambient super-samples = 2048. The same urban geometry model and weather data used in the proposed model were imported into Grasshopper as inputs to generate comparable results.

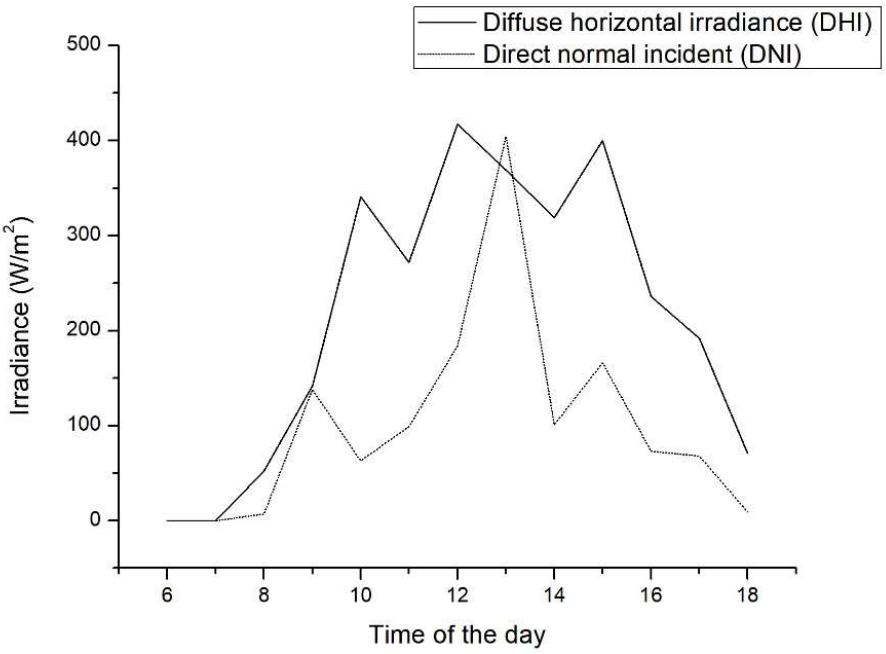

Figure 21. Daylight conditions of the tested day used in the simulation comparison between the proposed method and RADIANCE.

3.3.1 Effect of model setting parameters

As a necessary step before the intended comparison, the effects of the model setting parameters were investigated in terms of both the prediction accuracy and computational efficiency. The resolution-control parameters include the sky horizontal subdivision (SHS), strip inside subdivision (SIS), sky radiance sampling subdivision (SRSS), and building edge subdivision (BES). Table 5 shows the ranges of the four control parameter values. Differential sensitivity analyses were performed to examine the effects of individual control parameters by changing one parameter value at a time, while keeping the rest of the parameters fixed at the base value. The resulting outcomes is a stability test for optimising the control parameter settings in order to achieve a balance between prediction accuracy and computational efficiency. Table 5 provides chosen settings based on the sensitivity results, which were used in the case

study for comparisons of the proposed model against RADIANCE and measurements.

Table 5. Ranges of values for the control parameters.

Setting parameter	Range	Chosen value
SHS	3 - 36	24
SIS	1 - 4	2
SRSS	3 - 18	9
BES	1 - 11	3

Figure 22 shows the cumulated solar radiation (Wh/m^2) during the test hours and associated computational costs with different parameter settings for the three urban locations shown previously in Figure 20. Overall, SHS (Figure 22 a) is the most dominant parameter that has the highest impact on the prediction accuracy in comparison to the other parameters. For SHS, incremental changes up to 18 significantly impacted the prediction results, especially for the high-density scenario. Further increases in SHS did not impact the prediction accuracy despite the linear increase in the computational time. SIS (Figure 22 b) exhibited a similar trend, and the prediction accuracy noticeably improved until SIS increased to the value of two. SRSS (Figure 22 c), however, did not elicit a substantial impact on the prediction accuracy, and did not noticeably increase the computational cost. Because the computational cost did not change much with the increase of SRSS, SRSS was set to be nine for further analyses. Additionally, changes in BES (Figure 22 d) did not change the prediction accuracy although the use of the finer resolution of 1 m for BES exponentially increased the computational cost. Hence, BES was set to be three for the following case studies. Overall, the results suggest that for the low-density case crude control settings provided prediction outcomes as accurately as some of the refined control settings. For high-density urban areas, however, the control settings need to be carefully designed to provide sufficiently accurate predictions with minimal computational cost.

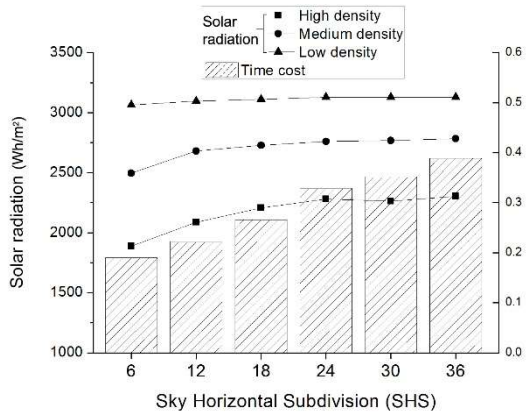

Figure 22 a. Effect of SHS.

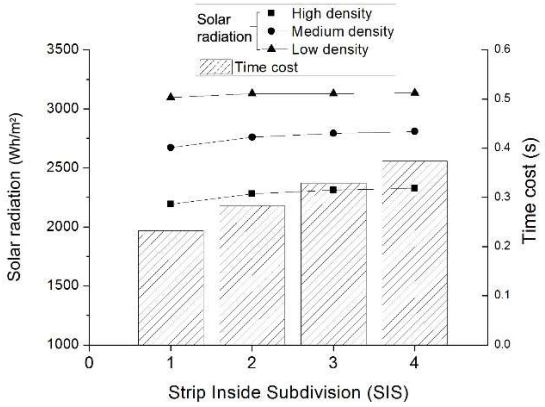

Figure 22 b. Effect of SIS.

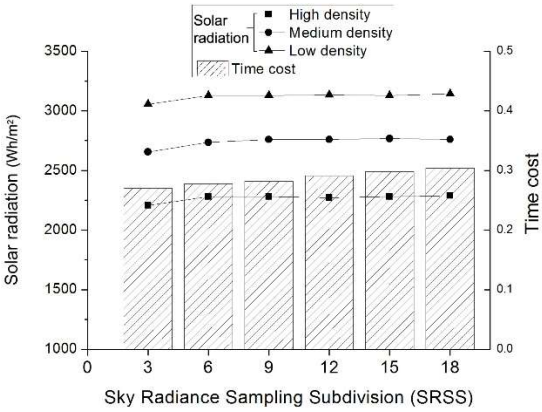

Figure 22 c. Effect of SRSS.

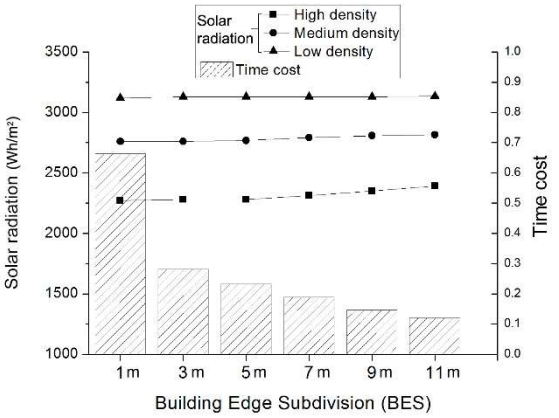

Figure 22 d. Effect of BES.

3.3.2 Results

This section evaluates the predictive power of the proposed method in comparison to RADIANCE through the case study of the urban area described in Section 3.3. Tables 6-8 summarize cumulated solar radiation (Wh/m^2) during the test hours predicted by the proposed method and RADIANCE for the three urban density areas. Overall, the proposed method yielded predictions that were in good agreement with RADIANCE. The proposed method yielded predictions with average differences of 3%, 4%, and 6%, in comparison to RADIANCE for the low-, medium-, and high-density areas, respectively. The differences in the irradiance prediction between the two methods increased within a small range for the studied urban area with a higher density. In addition, the proposed method tended to overestimate the total irradiance on the horizontal or slightly tilted planes and underestimate that on the vertical or

nearly vertical surfaces. As the proposed method approximated the contours of the buildings, the method may likely ignore details in the real contour that obstruct the irradiance on the test point and, consequently, cause an overestimation of the total irradiance. Nevertheless, the magnitude of the overestimation can be regarded as negligibly small. Underestimated irradiance predictions for vertical surfaces may be due to the simplified reflection model that considers only the first-bounce reflection. Indeed, vertical surfaces (mostly walls) receive increased radiation from multiple reflections by the surrounding surfaces than horizontal surfaces. Nevertheless, the absolute magnitude of the underestimation is small.

Table 6. Comparison of the predictions of the two tested models for the high-density area.

Tilted angle (°)	RADIANCE (Wh/m^2)	Proposed method (Wh/m^2)	Absolute difference (Wh/m^2)	Difference
0	2176	2295	119	5.47%
20	2422	2593	171	7.06%
40	2437	2621	184	7.55%
60	2189	2325	136	6.21%
80	1693	1702	9	0.53%
90	1392	1261	-131	-9.41%

Table 7. Comparison of the predictions of the two tested models for the medium-density area.

Tilted angle (°)	RADIANCE (Wh/m^2)	Proposed method (Wh/m^2)	Absolute difference (Wh/m^2)	Difference
0	2711	2795	84	3.10%
20	2986	3132	146	4.89%
40	2979	3086	107	3.59%
60	2657	2712	55	2.07%
80	2082	1971	-111	-5.33%
90	1715	1588	-127	-7.41%

Table 8. Comparison of predictions of the two tested models for the low-density area.

Tilted angle (°)	RADIANCE (Wh/m^2)	Proposed method (Wh/m^2)	Absolute difference (Wh/m^2)	Difference
0	2941	3133	192	6.53%
20	3267	3372	105	3.21%
40	3353	3412	59	1.76%
60	3079	3125	46	1.49%

80	2463	2434	-29	-1.18%
90	2142	2081	-61	-2.85%

Table 9 shows the root mean square errors (RMSE) between hourly predictions by the proposed method and those by RADIANCE for the medium-density area. RMSE values ranged between 11.41 Wh/m^2 and 21.02 Wh/m^2 for the different tilted planes. The percentages of the RMSE values to their average hourly predictions ranged between 3% and 9%. Further correlation analysis on the basis of the Pearson's coefficient gives the R-squared value of 0.993 between the two sets of hourly predictions as illustrated in Figure 23.

Table 9. RMSE of the proposed method against that of RADIANCE for the medium-density area.

Tilted angle (°)	0	20	40	60	80	90
RMSE (Wh/m^2)	11.41	21.77	20.99	9.04	21.02	18.51
Percentage	3.37%	5.83%	5.64%	2.72%	8.08%	8.63%

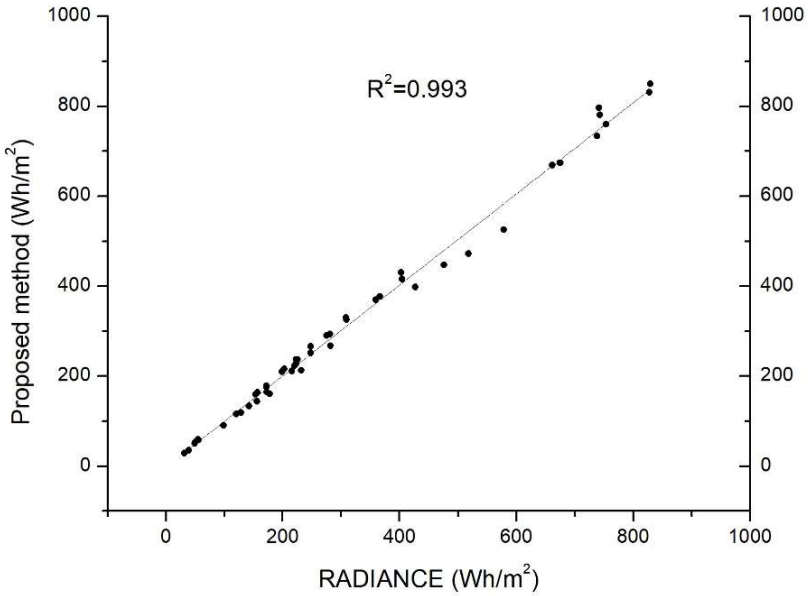

Figure 23. Correlation between the hourly predictions by the proposed method and those by RADIANCE.

In addition, the accuracy of predictions was evaluated in the context of large-scale applications, whereby the total or average amount of solar energy obtained in the entire urban area was the core interest. The entire case study area included 337 buildings, and the total radiation of all the building surfaces during the testing day was selected as a performance indicator for large-scale applications for model comparisons. Table 10 compares the total solar

radiation predicted and the according computational time cost by the two methods for the entire set of building surfaces. The calculation time was recorded on a PC system geared with Intel i5 4590 CPU, 12 Gigabytes dual-channel DDR3 RAM, implemented on a 64-bit Windows 10 operating system. The predicted results of the proposed method were in close agreement with RADIANCE. The total calculation time for our method is 266 seconds, a relatively low run time given the scale of the studied case compared to the much longer calculation time in RADIANCE. It should be noted that computational time cost heavily relates to several factors, including parameter settings in the software, the used programming language, programmer efficiency. In order to compare the computational efficiency of the proposed methods with existing methods that rely on the ray-tracing technique in a fair manner, an elementary comparison of key computational steps against the ray-tracing technique was carried out and presented in the Section 3.5.

Table 10. Total irradiance of a large-scale urban area.

	RADIANCE	Proposed method	Difference
Irradiance (kWh)	1,574,473	1,515,531	3.74%
Time cost	21643s	266 s	

3.4 Comparison against controlled experiments

3.4.1 General design

A physical micro urban geometry model was constructed in a scale of 1:150 of the case urban area. Figure 24 (upper-right sub-figure) shows the physical urban model used for the controlled experiments. Owing to the limited budget, part of the case study area described previously was created as the physical model. The physical model was made of thin wood boards cut by a digital laser cutting machine. The physical model was placed on the roof of a four-story building located in the campus of the Huazhong University of Science and Technology, Wuhan, China. The building avoided most of the shading from surrounding

environments. However, two main surrounding objects may potentially impact the results of the experiments: an annex room built on the roof and trees located close to the roof, as seen in Figure 24. As they are close to the experiment site, they may impact both the shading and the reflection on the physical model. Thus, they were included in the 3D urban geometry model used for predictions. The size of the annex room and trees were measured using photo-based three-dimensional scanning, as shown in the bottom of Figure 24. The surrounding trees to the north of the site were approximated as a rectangular box in the model.

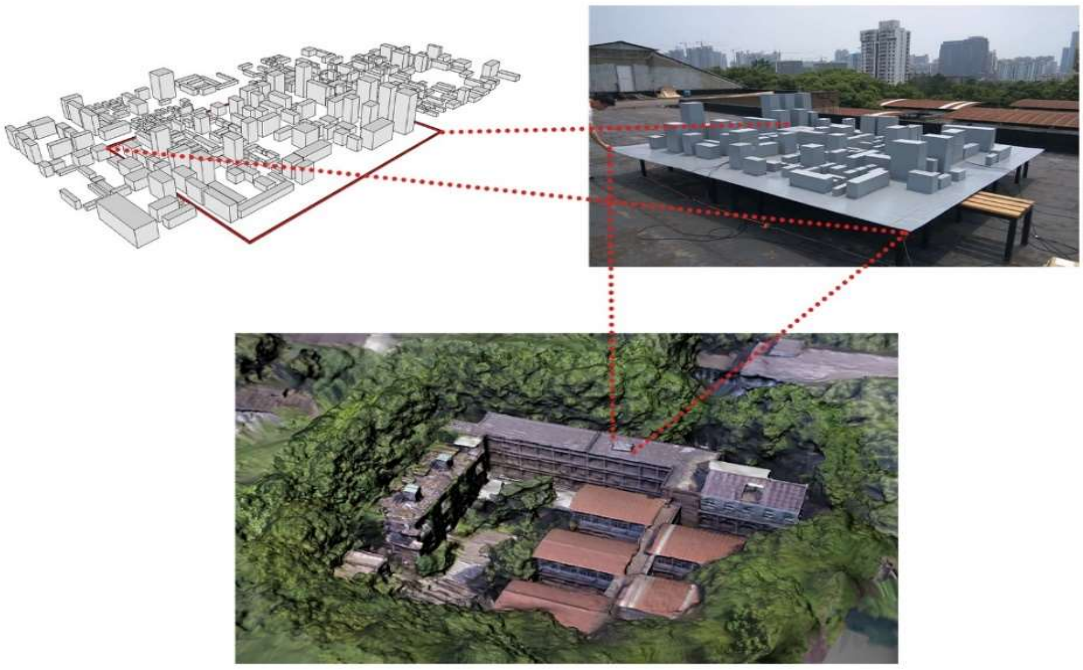

Figure 24. The physical urban model used for controlled experiments.

Two sets of controlled experiments were designed to investigate the model performance in terms of the total irradiance prediction with and without reflected irradiance. Figure 25 shows one urban geometry model with different surface albedo values. Set 1 (left) has black-painted surfaces to minimize the reflection among surfaces as much as possible. Set 2 (right) has light grey-painted surfaces for the buildings and darker grey-painted surfaces for the roads to appropriately represent real albedo values of urban surfaces in urban environments. A comparison of the proposed model against the two sets of measurements allowed the investigation on whether the reflection model based on significant simplifications suitably

capture major reflection phenomena.

Figure 25. Two urban geometry models. Model for Set 1 (left), and model for Set 2 (right).

Four full-range spectrum radiometers (Jinzhou Sunshine TBQ-2) were used in the experiments to collect solar irradiance measurements on selected test points. They were installed inside building boxes, as shown in Figure 26. The radiometers were carefully installed to ensure that they were parallel and aligned to the installed building surface, and that they properly collected the irradiance on test points. To include more test points in the model evaluation, the radiometers were installed in different locations on each day of the measurement period. Figure 27 shows test points used for data collection in the two sets of experiments, including 11 test points for Set 1, and 14 test points for Set 2.

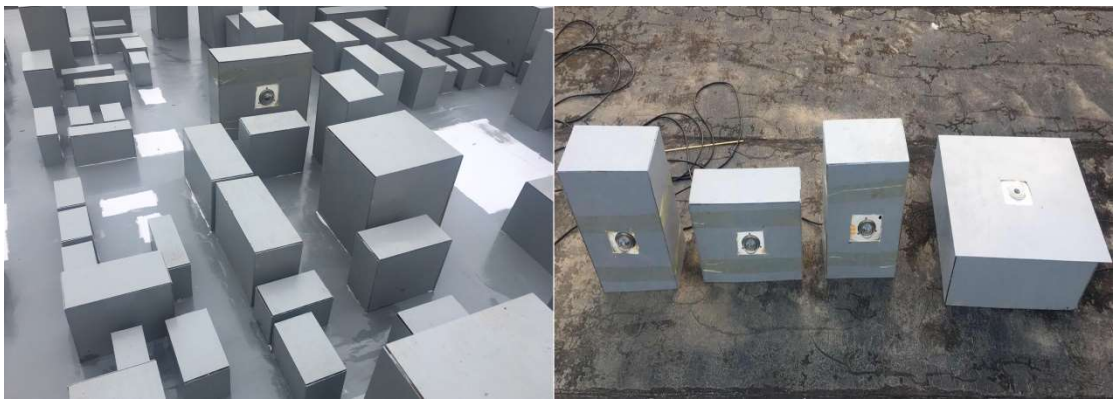

Figure 26. Photos of the TBQ–2 radiometers installed in the physical model.

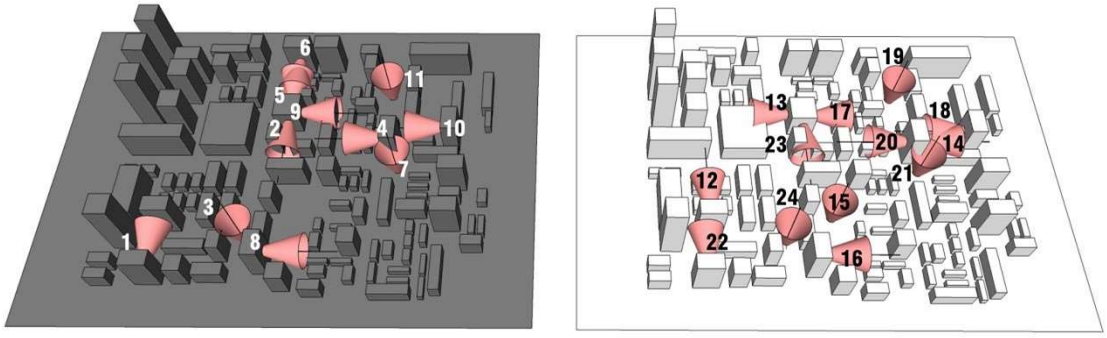

Figure 27. Test points used in Set 1 (left) and Set 2 experiments (right).

3.4.2 Construction of the physical urban geometry

As the physical urban geometry is a physical representation of the urban case to collect solar measurements for result comparison, it is important to make sure the representation is correct and matches the 3D computational geometry model in the simulation using the proposed method.

To construct the physical model, CAD file of the computational geometry model was exported to a digital laser cutter. Then, a total number of thirty-two 2mm thick A0 size wood boards were printed, cut and labeled with numbers for each piece that resembles each roof and wall of the buildings in the study urban area. Figure 28 (left-subfigure) shows the wood boards before dissembling them for reconstruction. After each piece from the wood boards was retracted, each building (Figure 28 right-subfigure) was manually assembled with the number-labeled pieces of wood board in superglue to make sure the correct pieces are assembled for the correct building. After this process, all the initial building “boxes” were ready for further assembling as Figure 29 shows.

Fig 28. Wood boards cut by digital laser cutter (left); the process of reassembling the buildings from pieces of the cut board.(right)

Figure 29. Building “boxes” of the physical geometry model.

The next step is to apply paint to control the albedos of the building models (Figure 30). As previously described, there are two sets of controlled albedos for the two comparisons. This was simply done by first applying the physical model with grey paint. After measurements for the set were collected, black paint was then applied to the same physical geometry model and carried on to collect the measurements the other set.

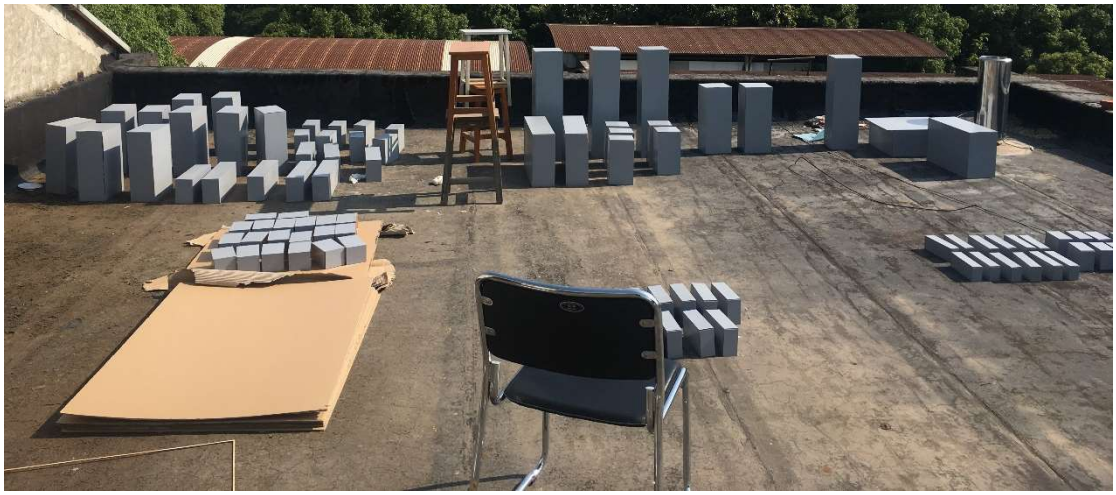

Figure 30. Building “boxes” painted in light grey.

The next step is to create a plan for the urban layout. This was done by printing out the building footprints from the CAD file and attached the prints on top of another layer of corrugated fiberboard as Figure 31 shows. Next, a controlled albedo for the ground surface was applied onto the board and left out the building footprint area so that building models can be correctly placed on top of the baseboard. After the baseboard was painted, each building box was placed and glued on to the board. Additionally, an elevated surface was placed under the physical model to eliminate the shading effects from the parapet on the roof as Figure 32 shows.

Figure 31. Printed sheet of urban layout on top of the baseboard.

Figure 32. Painting process of the ground of the physical urban model.

Another important step of the model construction was making sure the facing direction is correct. A GPS device was used to draw the absolute south on the ground as a reference to adjust the facing direction of the physical model. Finally, the finished physical urban geometry model (Figure 33) was ready for further installing the solar collectors on to the test points.

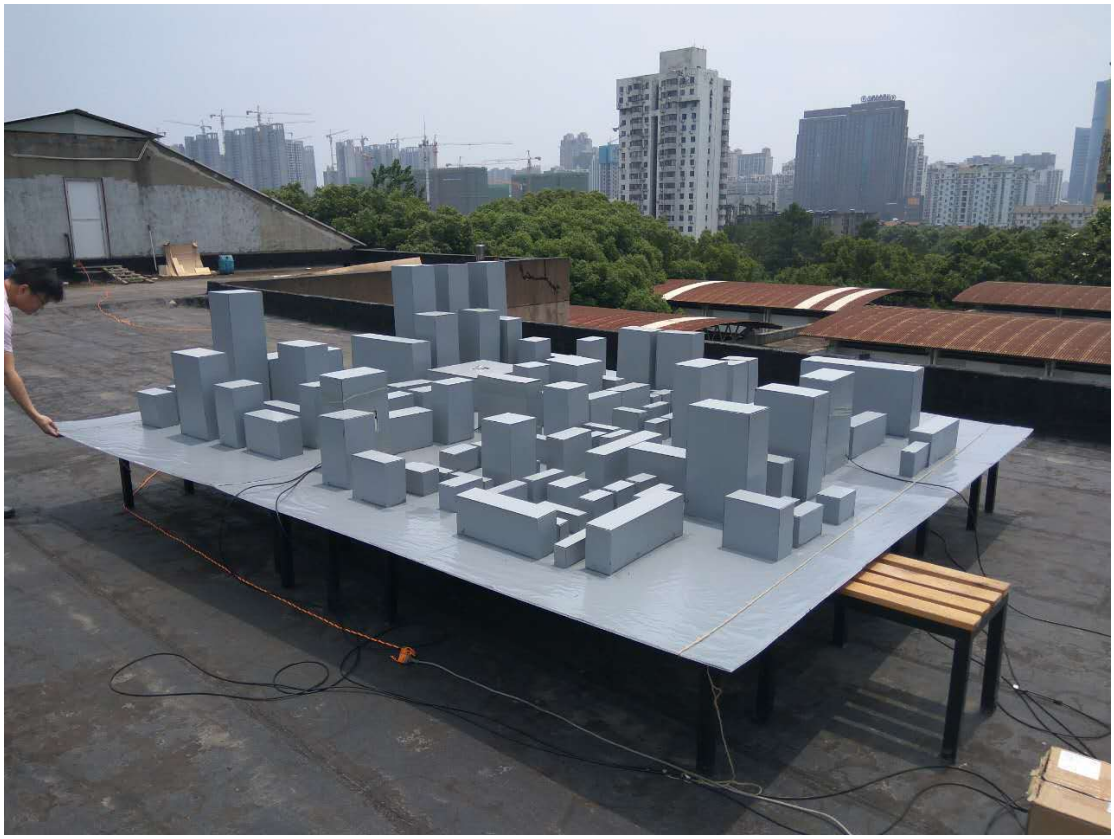

Figure 33. Image of the physical urban geometry model.

3.4.3 Weather measurements

Three weather variables are required as weather inputs to the proposed model, namely the diffuse horizontal irradiance (DHI), direct normal incident (DNI), and dew-point temperature. In a typical weather file such as TMY2 and TMY3, DHI and DNI are calculated by the common standardized procedure described in (Vignola et al., 2016) using the measurements from a pyranometer (i.e. solar meter) with a shadow band (Figure 34, left-subfigure) and a pyranometer without any obstruction (Figure 34 right-subfigure). First, a shadow-band radiometer that obstructs the direct sunlight measured a raw horizontal diffuse irradiance. The raw diffuse irradiance was then calibrated with an additional shadow-band correction factor to make up the

loss of sky diffuse radiance blocked by the shadow-band and allowed computation of the DHI. The global horizontal irradiance directly measured by a pyranometer (Figure 34, right-subfigure) was used to compute DNI on the basis of the location of the sun.

Figure 34. Radiometers used in the experiments for weather input measurements.

In addition, the proposed model used dew point temperature data measured by a mini-weather station located on the roof next to the location of our experiment setup, which was provided by the School of Architecture of the Huazhong University of Science and Technology. The experiments spanned two weeks, and were carried out from May 26th 2017 to June 8th 2017. However, measurements were not collected during rainy days owing to the unavailability of waterproof equipment. Thus, measurements were obtained only during sunny or cloudy days. Table 3 lists the weather conditions for different test points during the experimental period.

Table 3. Weather conditions during the measurement period.

Test points		Date	Measurement duration	Weather condition	Temperature range (°C)
Set 1	1, 2, 3	June 6th	6:00 – 10:00; 13:00 – 18:00	Partly cloudy	18.6 – 25.2
	4, 5, 6, 7	June 7th	6:00 – 18:00	Sunny	20.9 – 31.3
	8, 9, 10, 11	June 8th	6:00 – 18:00	Partly cloudy	23.6 – 32.5

Table 3. (Continued)

Set 2	12, 13, 14, 15	May 26th	6:00 – 18:00	Sunny	21.5 - 31.3

	16, 17, 18, 19	May 28th	6:00 – 18:00	Sunny	24.0 - 33.7
	20, 21	May 29th	6:00 – 18:00	Sunny	24.4 – 34.1
	22, 23, 24	May 30th	6:00 – 16:40	Cloudy	27.7 – 31.9

3.4.4 Measurements uncertainty

Two major sources of uncertainties associated with the process of generating the weather inputs are the radiometer measurement error and the shadow-band correction factor. The measurement error of the solar radiometer was provided by the manufacturer and quoted to range between ±2%. The shadow-band correction (*F*) factor depends on the algorithm used to compensate for the obstructed diffuse irradiance owing to the shadow band, according to the shading bandwidth, solar position, and geographic location. Even though the two algorithms (Drummond, 1956; Robinson and Stoch, 1964) are extensively adopted in practice, Zhang et al. (1997) found that the *F* values from the referred methods did not match the observations in the Chinese weather stations. Correspondingly, they developed a statistical model to generate monthly average *F* values for different geographic locations of major cities in China. All the three methods were used to calculate *F* values, and the resulting values ranged between 1.23 and 1.27, as summarised in Table 4. Given that dew-point meters measure dew point temperature with high accuracy, and the dew point temperature has a much smaller impact on the irradiance than the other two weather variables, the measurement uncertainty of the dew-point temperature was ignored in the model evaluation process. Additionally, the maximum and minimum values of surface albedos were obtained by measuring them multiple times in different locations of the physical model (Figure 35). In total, six uncertain model inputs were considered, as listed in Table 4.

Figure 35. Albedo values measured using the PLKCN C84–III reflectivity meter.

Table 4. Listed ranges of parameter uncertainties.

	F-value	Radiometer error	Albedos of buildings in Set 1	Albedos of ground in Set 1	Albedos of buildings in Set 2	Albedos of ground in Set 2
Maximum	1.27	+2%	0.023	0.029	0.29	0.22
Minimum	1.23	-2%	0.009	0.013	0.27	0.20

The ranges of parameter uncertainties in Table 4 were used in the proposed model to compute the maximum and minimum predictions. As all the parameters listed above were found to be positively correlated with the model output, the model predicted two outputs: one with all the parameters set to their minimum values and the other with all the parameters set to their maximum values.

3.4.5 Impact of parameter uncertainty on the prediction

Table 11 shows the ranges of total average irradiance predictions due to the identified input uncertainties for all the test points in terms of both the absolute differences of the maximum and minimum outputs and the percentage of the difference compared to the maximum output. The table also presents the orientation and obstruction level of the test points represented by SVF, calculated by the proposed method. The differences between the maximum and minimum

outputs ranged between 4–30 W/m^2 and between 4–13%. As the ranges of the predictions due to the input uncertainties are relatively small, averages of the maximum and minimum outputs were used for the comparison against the measurements.

Table 11.
Differences in maximum and minimum model output given considerations of the input uncertainties.

Sets of viewpoints	Orientation	Obstruction level (by SVF)	Difference of maximum and minimum outputs	
			W/m^2	%
Set 1				
Test point 1	South	0.37	7.08	8.94%
Test point 2	North	0.36	8.34	11.71%
Test point 3	Horizontal	0.61	15.36	4.97%
Test point 4	East	0.44	17.44	6.91%
Test point 5	South	0.39	11.79	13.22%
Test point 6	North	0.43	13.47	12.97%
Test point 7	Horizontal	0.68	22.86	4.36%
Test point 8	West	0.34	10.97	5.20%
Test point 9	West	0.38	11.23	5.37%
Test point 10	East	0.44	12.73	7.24%
Test point 11	Horizontal	0.72	22.00	4.61%
Set 2				
Test point 12	South	0.42	15.19	10.66%
Test point 13	East	0.40	17.32	5.97%
Test point 14	West	0.37	18.33	7.02%
Test point 15	Horizontal	0.72	26.38	4.39%
Test point 16	West	0.34	14.16	4.94%
Test point 17	West	0.38	15.11	5.46%
Test point 18	East	0.44	17.69	6.43%
Test point 19	Horizontal	0.72	26.32	4.26%
Test point 20	East	0.44	20.06	6.48%
Test point 21	Horizontal	0.68	25.44	4.15%
Test point 22	South	0.37	4.69	7.82%
Test point 23	North	0.36	5.82	9.06%
Test point 24	Horizontal	0.61	11.37	5.89%

3.4.6 Results

Figure 36 compares hourly irradiance predictions (W/m^2) against measurements during the test day period (6 am – 5 pm) for the 24 test points. There are missing measurements for rainy days and for the specific two-hour intervals of 11 am – 12 pm owing to equipment failure. Overall, the proposed method was able to reproduce the actual measurements accurately and elicited only a small range of discrepancies. The magnitude of discrepancies showed variations depending on the position of the test point and weather conditions. For horizontal surfaces with a high sky view factors (test points 7, 11, 15, 19, and 21), the method tended to overpredict the irradiance noticeably when the irradiance increased at the middle of the day. For all the vertical surfaces, the magnitude of the predicted errors did not seem to be time-dependent. The method tended to underpredict the irradiance, but the differences were relatively small. Figure 37 plots the hourly predictions in comparison to measurements for all the test viewpoints. A Pearson's coefficient of the two datasets was the R-squared value of 0.974. Higher differences between hourly predictions and measurements were observed when the magnitude of irradiance increased. Nevertheless, overall the high correlation coefficient indicates a good agreement between the hourly predictions and measurements. It is worth mentioning that the correlation between the predictions and the measurements (R^2=0.974) is slightly lower than that (R^2=0.993) between the proposed method's predictions and RADIANCE's predictions shown in the previous section. A key difference between the two sets of comparisons is that both the prediction models are based on the Perez Sky model (Perez et al., 1993) whereas the measurements are based on the actual sky radiance conditions that may differ from the Perez model outcomes. To exclude the possible errors due to the Perez model in the comparison, advanced equipment, such as an artificial sky or sky scanner that directly measures the sky radiance, can be adopted in physical experiments in the future study.

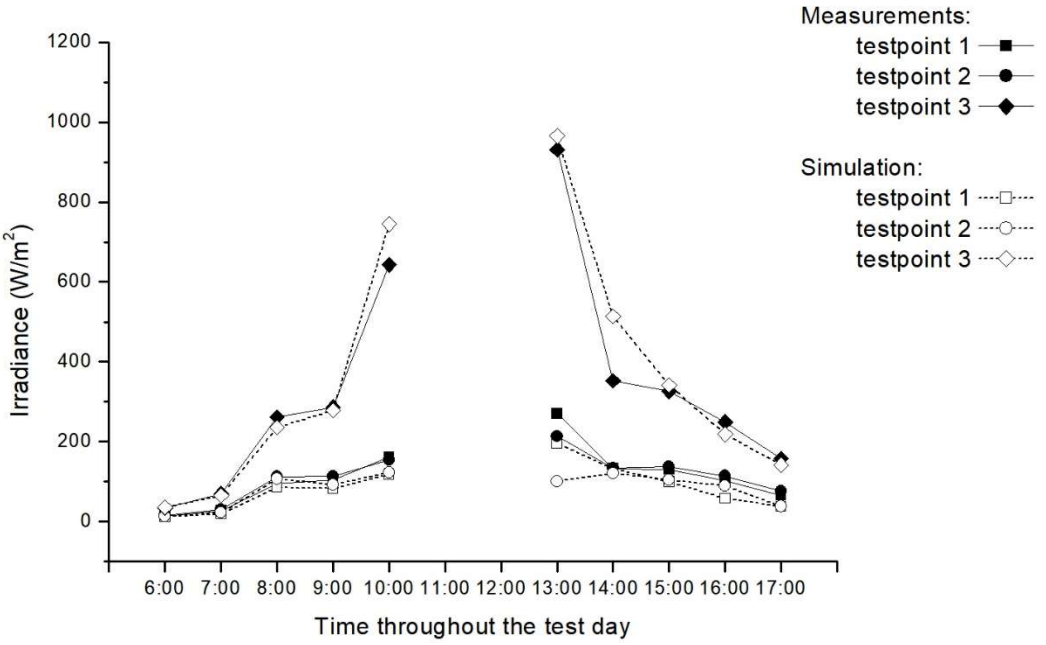

Figure 36 a. Comparison of hourly model predictions against measurements for test points 1–3

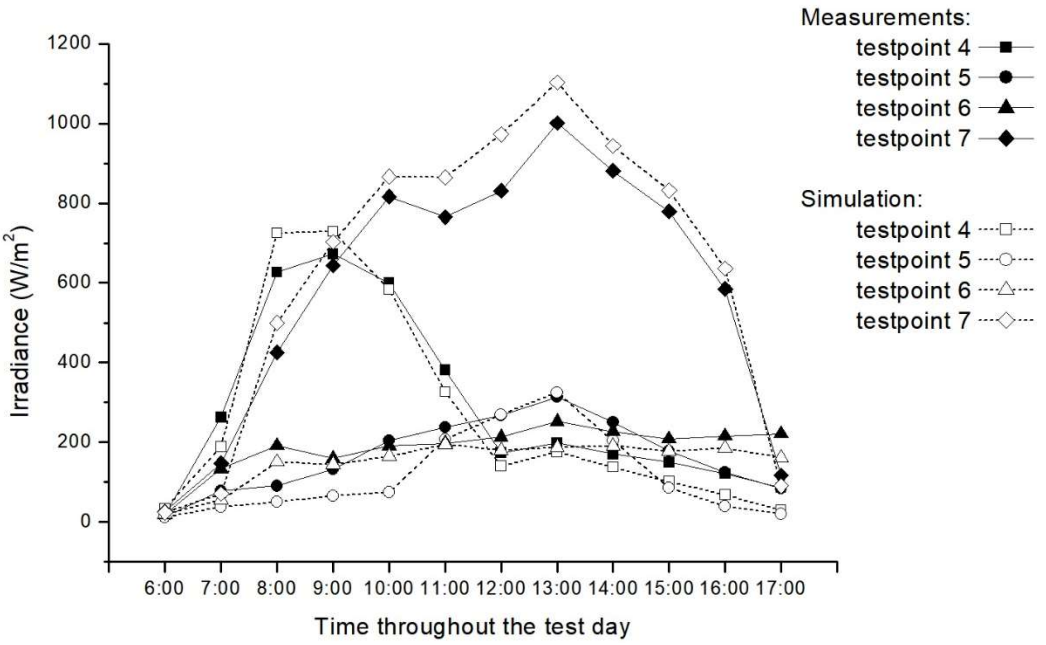

Figure 36 b. Comparison of hourly model predictions against measurements for test points 4–7.

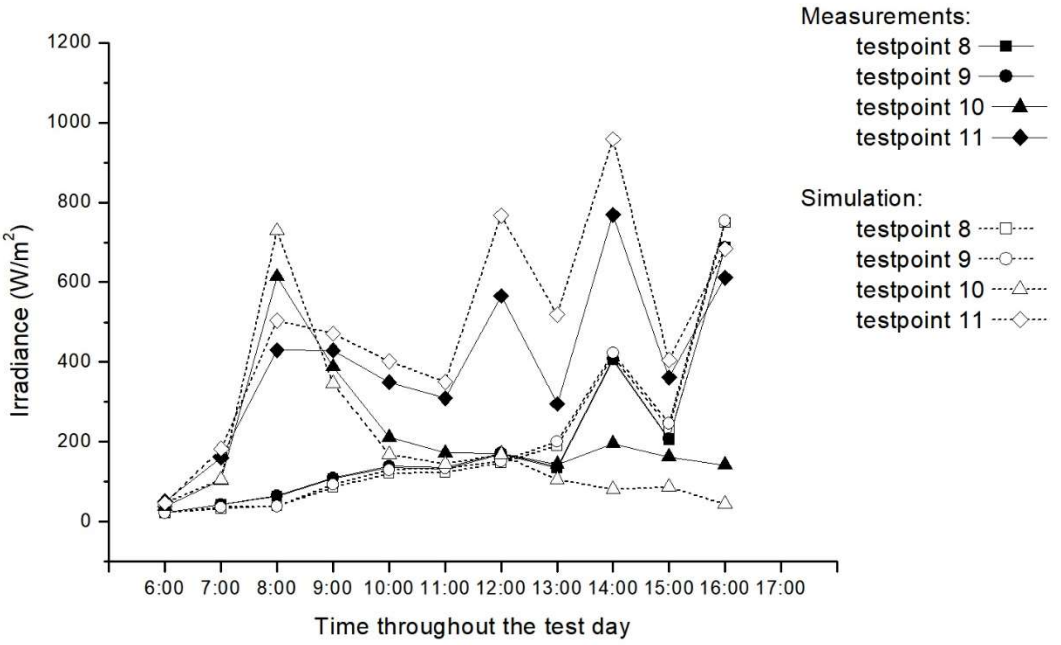

Figure 36 c. Comparison of hourly model predictions against measurements for test points 8–11.

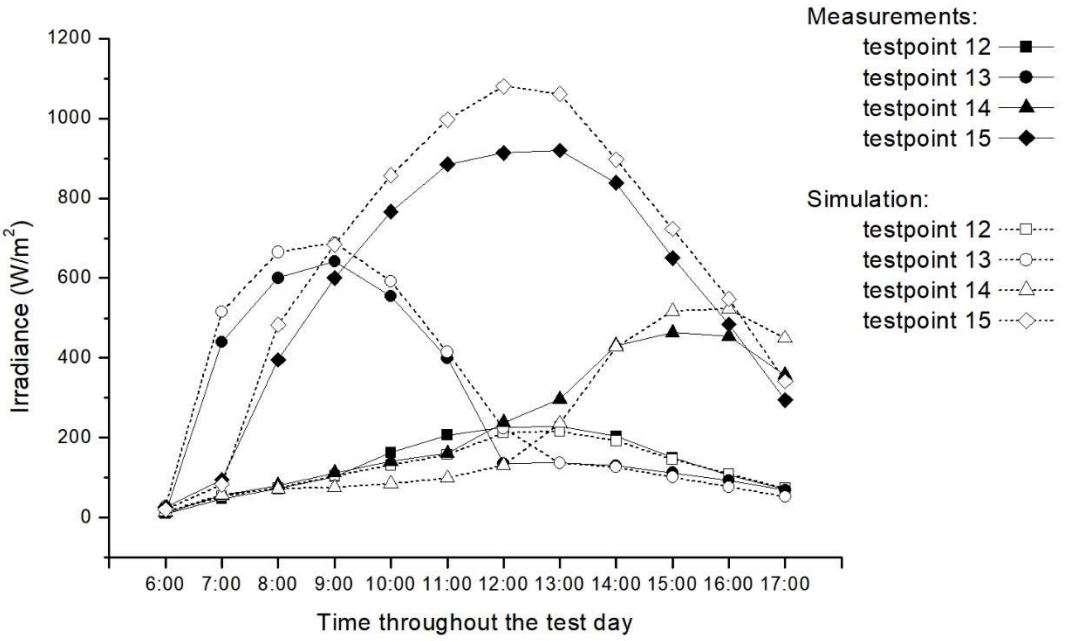

Figure 36 d. Comparison of hourly model predictions against measurements for test points 12–15.

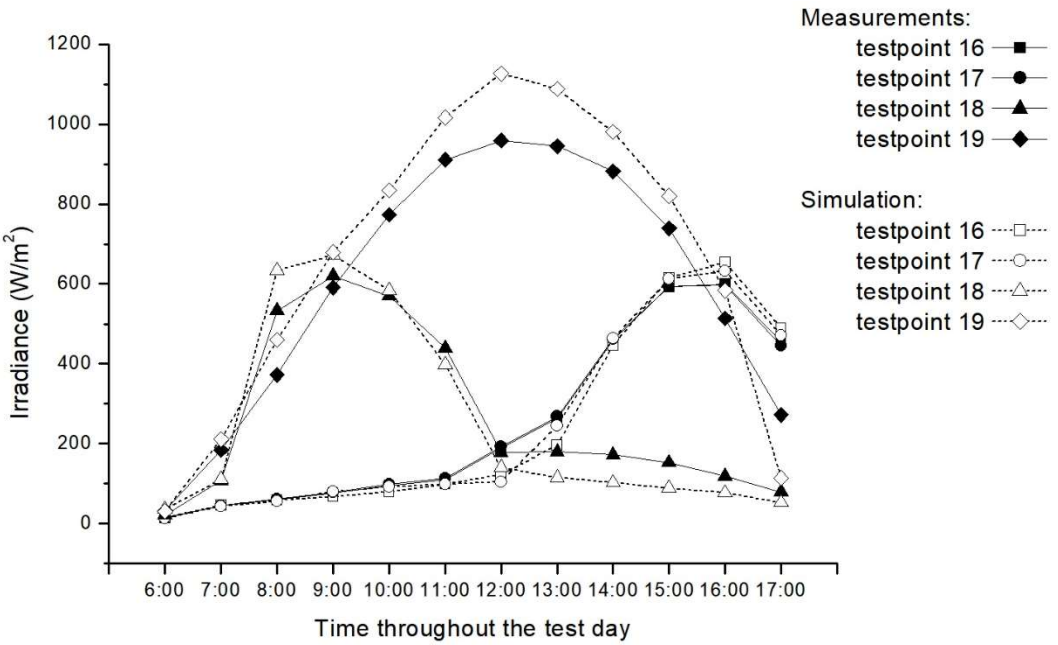

Figure 36 e. Comparison of hourly model predictions against measurements for test points 16–19.

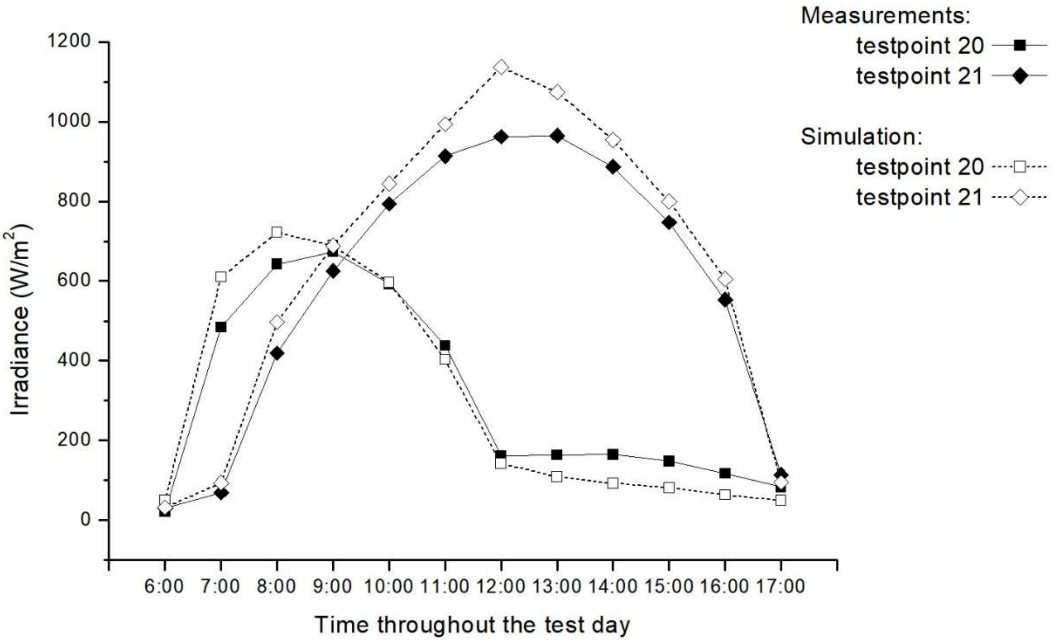

Figure 36 f. Comparison of hourly model predictions against measurements for test points 20–21.

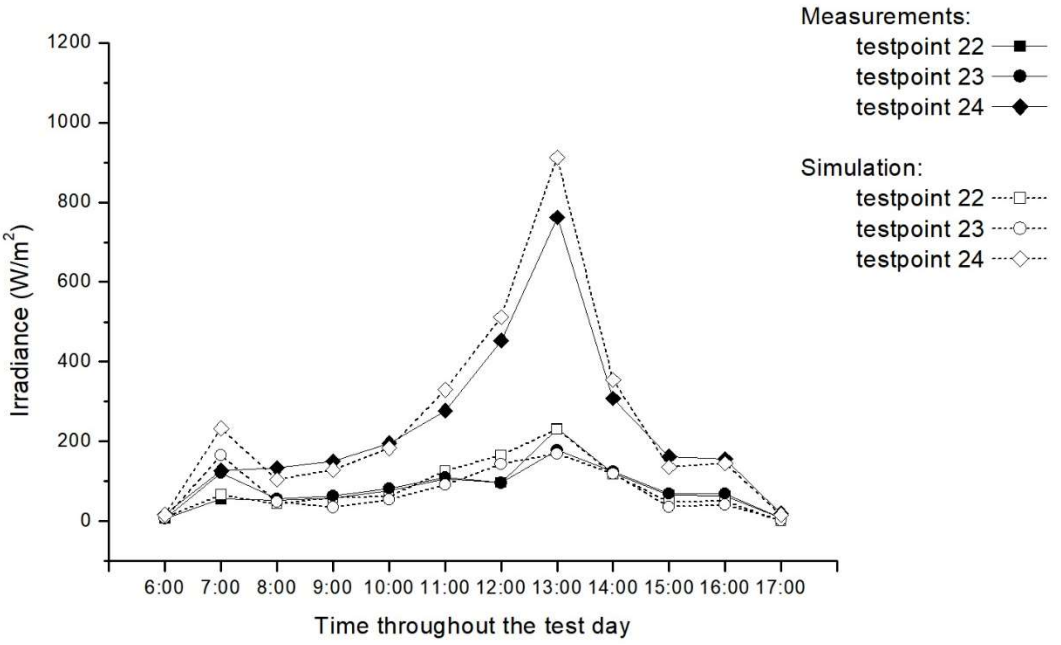

Figure 36 g. Comparison of hourly model predictions against measurements for test points 22–24.

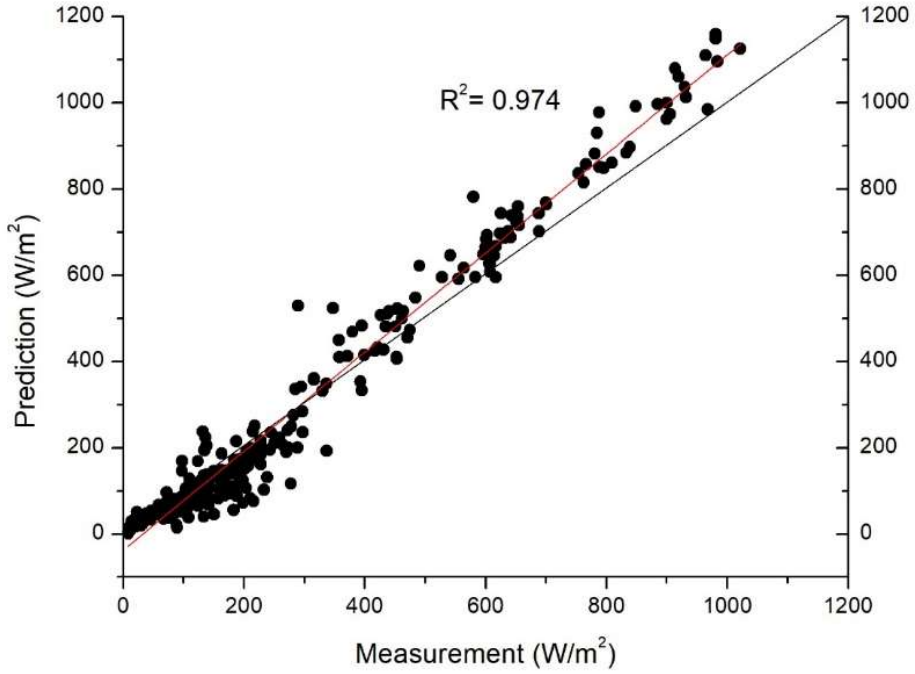

Figure 37. Correlation between hourly predictions and measurements.

Furthermore, the differences between the predictions and measurements were investigated in terms of the cumulated solar radiation during the tested day period, as presented in Table 12. In general, the differences between model outputs and measurements ranged from 3.31 Wh/m^2 up to 87.14 Wh/m^2 (from 0.96% to 14.79%), and most test points resulted in a deviation of approximately 5% or less. For vertical surfaces, no consistent trend was observed in the

recorded differences when the model predictions were compared against Sets 1 and 2. It was expected that the simplified reflectance model may result in a higher difference for vertical walls which received reflected irradiance from reflective surrounding surfaces. However, Set 1 (black-colored surfaces) yielded increased differences in some cases (test points 1, 2, 5, and 6) than Set 2 (grey-colored surfaces). Noticeably, the proposed model tended to overpredict the irradiance on the horizontal surfaces. In contrast, for vertical surfaces, the differences between the predictions and measurements varied for different test points.

Table 12. Differences between cumulated solar radiation prediction and measurements.

Set 1	Absolute error (Wh/m^2)	Percentage	Set 2	Absolute error (Wh/m^2)	Percentage
Horizontal roofs and ground					
Test point 3	20.9	3.4%	Test point 15	75.2	6.7%
Test point 7	49.0	4.2%	Test point 19	64.2	5.4%
Test point 11	87.1	11.1%	Test point 21	61.4	5.2%
			Test point 24	25.7	5.6%
Vertical walls					
Test point 1	-24.0	-11.8%	Test point 12	-3.9	-1.6%
Test point 2	-26.9	-13.2%	Test point 13	26.3	4.9%
Test point 4	-18.3	-3.2%	Test point 14	-5.8	-1.3%
Test point 5	-48.8	-14.8%	Test point 16	-5.9	-1.2%
Test point 6	-34.8	-9.4%	Test point 17	-4.8	-1.0%
Test point 8	5.2	1.4%	Test point 18	-13.2	-2.5%
Test point 9	9.2	2.4%	Test point 20	-6.9	-1.1%
Test point 10	-28.8	-6.7%	Test point 22	3.3	2.1%
			Test point 23	-5.9	-3.6%

To further investigate major factors that determine the trend of prediction errors, the prediction discrepancies for all test points were correlated to the SVFs of the test points (Figure 38). The prediction discrepancy was defined in terms of the absolute prediction discrepancy and the percentage of discrepancy. Results showed that the absolute discrepancy was highly and positively correlated ($R^2 = 0.69$) with SVF, indicating that the proposed model tended to overpredict the irradiance for test points with lesser obstruction, such as the roofs. For the walls for which there was increased shading, the proposed model had a tendency to underpredict the irradiance. In terms of the discrepancy reported as a percentage, the results also led to the same conclusion, but the correlation was smaller ($R^2 = 0.39$). Overall, the irradiance predicted by the

proposed model yielded average absolute differences of 6% and 5% in comparison to the measurements for the horizontal and vertical surfaces, respectively. Although there is the gap between the predictions and measurements, the proposed method with significant simplifications promised to be a suitable approach to achieve a satisfactory accuracy for urban-scale solar analyses, and concurrently complied with the required computational efficiency.

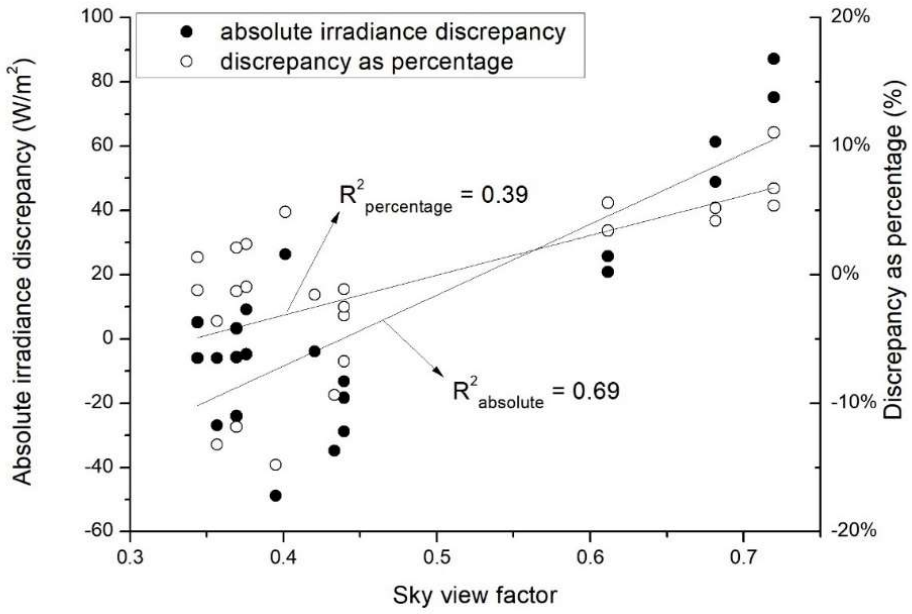

Figure 38. Correlation R^2 between SVF and prediction discrepancy.

3.5 Computational efficiency

This section examines the computational efficiency of the proposed method in a programming environment Python 2.7. The computer hardware platform was a laptop with an i7 8700 CPU, running on 32G DDR4-2666 Ram in a Windows 10 operating system. Using the study case and the settings described previously, the computational process was decomposed into several key steps and the calculation time of key steps was recorded in terms of their shares of the total calculation time, as shown in Table 13. Calculating view angles for obstruction detection took up the highest portion of 60%, followed by calculating first received irradiance, and calculating the first-bounce reflection. The rest of the steps in the process took very little time in comparison to the three steps.

Table 13. Shares of key steps in total computational time.

Reading geometry	<0.01%
Geometry subdivision	0.11%
Calculation of view angles	59.97%
Reading weather file	<0.01%
Creating sky radiance	0.17%
Calculation of first received irradiance	36.10%
Calculation of the first-bounce reflection	3.65%

This section also tested the computational cost of the method in calculating view angles for two different numbers of viewpoints in the same studied urban area to compute obstructed skylines. Table 14 shows the total run time, run time per viewpoint for two cases with a different number of viewpoints. The total calculation time is in linear relation to the number of viewpoints. With 100,000 viewpoints, the method completed the calculation for around 8 minutes. It is worth mentioning that Python is not necessarily the most efficient programming language in terms of computational cost, especially compared to C languages. The computational cost of the method can be improved further by using a more efficient programming language in the future.

Table 14. Run time of the proposed edge angle detection obstruction model

Number of viewpoints	Total runtime (s)	Runtime per viewpoint (s)
1,000	5.49	0.0055
100,000	532.02	0.0053

For comparison against ray-trace/ray interception, a ray tracer was implemented in Python 2.7 on the basis of the Möller-Trumbore ray interception algorithm (Möller and Trumbore, 2005). It is a fast and popular method for calculating the intersection of a ray and a triangle in three dimensions without needing precomputation of the plane equation of the plane containing the triangle. Standard codes for implementation can be found in (Scratchpixel, 2018). Using the case study area and settings described in Section 3.3, first the average time cost was obtained per elementary operation for obstruction detection. As the proposed method and ray interception fundamentally have a different approach for obstruction detection, an elementary

operation in the proposed method is calculations between a viewpoint and BES points on a surface edge whereas an elementary operation in the ray interception method is ray interception between a viewpoint and a sky patch where the Tregenza 145 sky was used in this comparison. Second, the number of required iterations (elementary operations) for one viewpoint against the entire case area was compared for both the methods. In the view angle method, the total number of iterations for one viewpoint is the number of surfaces, and in the ray interception method it is the product of the number of sky patches and that of the urban surfaces. Table 15 shows that the proposed method has a slightly lower time cost per iteration and a much lower number of required iterations for detecting obstruction than the ray interception method. Furthermore, the proposed method uses a very simplified approach for reflection calculation that only takes up less than 5% of total calculation time, overall the computational efficiency of the proposed method cost is considered to be improved for large-scale urban applications. However, it needs to be pointed out that computational cost depends on not only the algorithm, but the nature of programming environments, programmer's proficiency in addition to the complexity and scale of a testing urban area. None the less, the comparison provides evidence of a better computational efficiency offered by the proposed method against the ray interception approach.

Table 15. Elementary time cost for obstruction determination for one viewpoint.

	View angle method	Ray interception
Time cost per elementary operation (s)	3.03E-06	3.81E-06
Number of elementary operations(iterations)	1691	245195
Total time cost for one viewpoint (s)	0.0051	0.9330

3.6 Summary

This chapter examined the hypothesis: Simplified, vector-based model, tailored to urban applications, predicts accurate solar radiation on urban surfaces to effectively support urban-scale analysis.

The developed simplified vector-based model is texted in sets of comparisons using the case study of an urban case in Wuhan, China. The comparison study proved that the new method provides reasonably accurate predictions with flexible control settings and fewer model inputs

to effectively support large-scale solar analyses. In comparison to RADIANCE, the new method yielded predictions with the average differences of 3%, 4%, and 6%, for the low-, medium-, and high-density areas, respectively. The second comparison against measurements revealed that the method tended to overpredict the irradiance received on surfaces with a high sky view factor such as roofs and underpredict that on vertical surfaces with a low sky view factor. However, the average absolute differences between predictions and measurements were relatively small and of the order of 6% and 5% for horizontal and vertical surfaces, respectively. The computational efficiency of the new model was proven to be sufficiently improved in comparison to the current ray interception algorithms. The new model greatly reduced the iterations required for obstruction calculation that consumes most of the computational load and, therefore, greatly reduced the computational cost for large-scale solar simulation.

Chapter 4: Relevance of the new model in the urban solar energy planning process

4.1 Introduction

The chapter demonstrates the usability of the proposed vector-based method by examining the relevance of the developed method in the urban solar energy planning process, specifically, in the distributed PV planning process. The two modelling features crucial to the fidelity of distributed PV yield prediction at urban scale are a level of fidelity for modelling urban shading and solar reflection, and a level of fidelity for modelling PV system operation. Therefore, two key modelling features associated with solar potential evaluation are investigated in the solar energy planning process: (a) a level of fidelity for calculating urban shading and solar reflection and (2) dynamic PV system model.

The relevance of the models with different fidelity levels in decision-making was investigated through a case study of an urban area in Wuhan, China under three decision-making contexts: setting a solar target, place-making, and economic assessment for urban-scale distributed PV integration. The chapter examined the hypothesis: Solar analysis with full

representation of urban surroundings is necessary for the calculation of urban shading and solar reflection to correctly support distributed PV planning. Predictions and decisions by the developed method are compared against those of a lower fidelity models to investigate the importance of modelling urban shading and reflection with full representation of urban surroundings. Additionally, the hypothesis is furthered examined and highlighted by investigating the effect of an additional dynamic PV model on decision-making in comparison with the effect of the high-fidelity model for urban shading and solar reflection.

Figure 39 illustrates the study framework used to evaluate the effects of the key modelling features on decision support for three major decision-making contexts associated with the solar planning process.

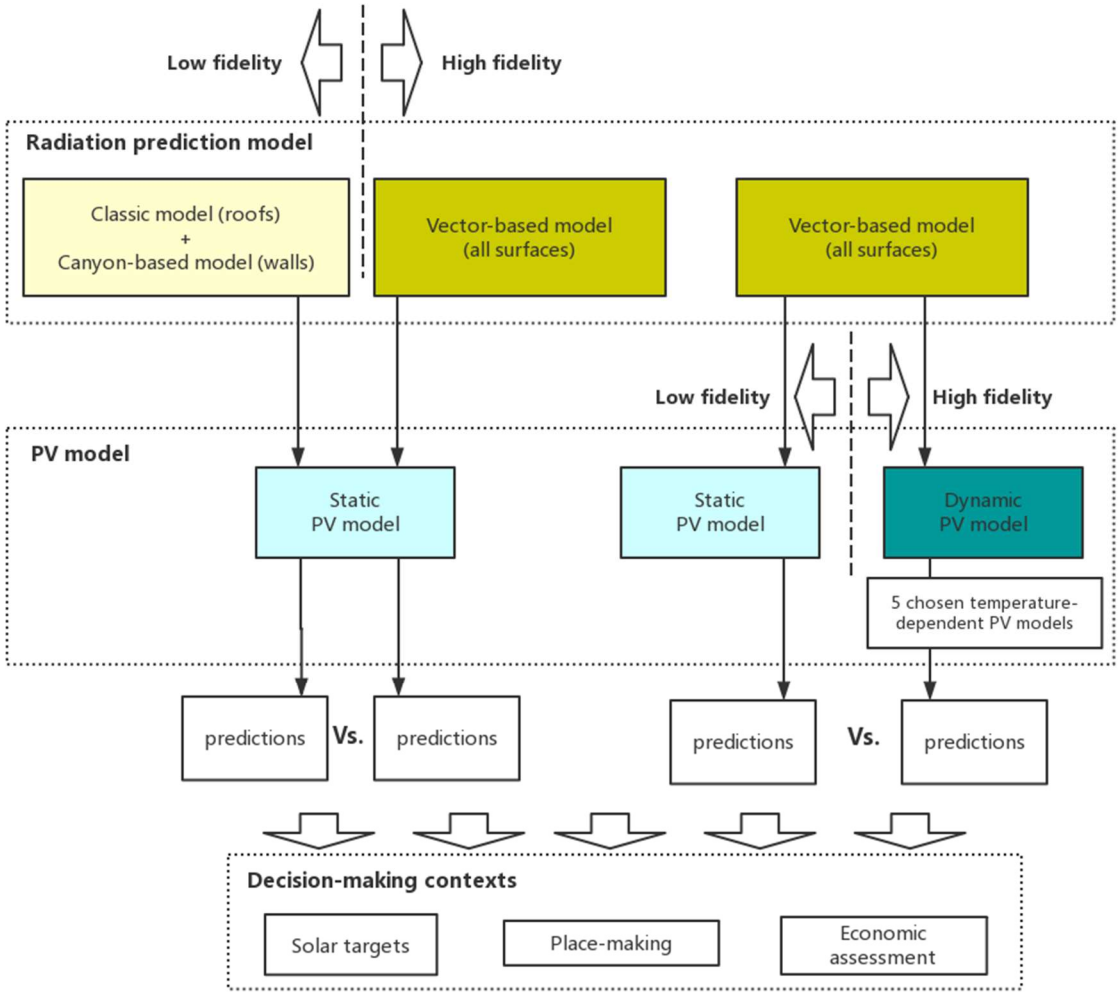

Figure 39. The study framework.

For examination of the level of fidelity of calculating urban shading and solar reflection with full representation of urban surroundings, two levels of relatively low- and high-fidelity models were selected to account for urban shading and solar reflection from surrounding buildings for comparison. For predicting received solar radiation on roofs, a classic model (Freitas, et al., 2015) without any consideration of urban shading was chosen as a low-fidelity model. As the classic model does not predict substantial shading on vertical walls, its applicability has been limited mainly to roofs. As vertical walls suffer a much worse daylight obstruction than roofs (Liao et al., 2018), the canyon-based approach (Robinson and Stone, 2004) was selected to roughly represent urban surroundings for daylight obstruction and reflection, as a relatively low-fidelity model for walls. The vector-based model tailored for urban applications proposed in the dissertation was selected as a high-fidelity model. The two levels of models were deployed in the three decision-making contexts to predict received solar radiation on surfaces of interest in a studied area in Wuhan, China. In this comparison, the two levels of models use the same static PV model to convert their predictions into PV yield. Therefore, differences in the results in this comparison are only due to whether urban shading and solar reflection are properly reflected.

For examination of the level of fidelity of a dynamic PV system model, two PV yield models were chosen for comparison. The static PV model assumes the PV system performs at a constant PV conversion rate regardless of its dynamic working conditions and corresponding PV cell operational temperature. In contrast, the dynamic PV model accounts for dynamic working conditions and, accordingly, yields dynamic conversion rates. 5 temperature-dependent PV models were used to generate a range of plausible PV yield predictions as the result of dynamic working conditions. In this comparison, the solar radiation predicted by the proposed vector-based model was used to evaluate the effect of modelling dynamic PV system operation in relation to the effect of the high-fidelity model for urban shading and reflection.

4.2 Urban distributed PV planning process

Distributed PV technology has been rising in urban areas where individual PV systems are integrated in buildings instead of a conventional centralized PV station in a distant location. The advantage of the distributed PV system in urban areas is that it provides energy directly in the building where energy is consumed. As a result, it reduces the need for extending infrastructure to transmit PV yield through long distances to consumers and avoids line losses of electricity during distribution. Besides, the distributed PV system can be grid-connected to sell the excess PV yield to the city grid as part of the urban energy system, and thus reduces the need of investing an energy storage system individually at the individual building level.

Models for solar potential evaluation at urban level have been developed to inform decision makings during various design phases for PV integration in urban buildings. For example, urban solar maps have been used to assist in selecting locations with high solar availability for PV installation by providing information about predicted PV yield, estimated investment cost, and potential carbon emission reduction (Mapdwell, 2018; Berlin Solar Atlas, 2018; Solarkataster, 2018). Some researchers further incorporated additional parameters, such as historical urban data including building types and ages for a comprehensive evaluation of solar applications in urban environment (Amado and Poggi, 2014; Berlin Environment Atlas, 2018). Researchers have also explored the electricity network compatibility to adopt the predicted PV yield electricity in urban areas. Wall (2012) generated hourly and monthly PV yield predictions and coupled them with three different distribution grids at one planned urban area in Sweden to identify the maximum PV hosting capacity and accordingly the resulting overload capacity given a maximum PV yield potential in the urban area. These studies above have demonstrated the importance of the methods in evaluating solar projects for a large audience of planners, developers and property owners in terms of economic and environmental benefits.

In the process of solar planning and design, various methods have been used to support solar potential evaluation. Kanters and Wall (2016) described a process map of solar energy

planning for buildings in the urban environment. The planning process consists of the following phases: political phase, urban design phase, building design (new buildings) and renovation (existing buildings) phase, implementation and monitoring phase. Based on a vast literature review on existing research and projects, Kanters and Wall (2016) pointed out that different levels of tools are necessary to provide useful information in different design phases. They also highlighted that the level of detail in the analysis model required for design phases increases as the design process goes from top (e.g., political phase and urban phase) to bottom (e.g., individual building and implementation phase).

4.2.1 Political phase

For the political phase that often requires solar potential at a national or regional scale, one of the key interests is the total amount of solar yield at large scale rather than individual building scale. For instance, the Chinese government set the solar target of reaching installed PV capacity of more than 110 GW, in which 60 GW should be distributed PV by 2020 in its 13th five-year plan for energy (Gosen et al., 2017). However, the plan does not specify how the national goal is broken down to the lower provincial and city levels. EU proposed a 7 Mtoe (1 Mtoe is equivalent to 11,630 GWh) target for total PV installation by 2020 (INEN, 2013). In its renewable energy directive, EU also set up a target in which renewable energy will provide 20 and 27 percent of the total energy consumption by 2020 and 2030, respectively (EU, 2009), along with individual renewable energy targets for all EU countries in their national action plans (Beurskens et al., 2011). By estimating energy demands and exploring possible alternative renewable energy options for different sectors in each EU member, the EU established the shares of each renewable technology responsible to meet the final targets.

Several research studies have performed analyses for solar potential evaluation at large scale. Wiginton et al. (2010) evaluated the potential of rooftop PV systems in a large-scale residential area by comparing the total estimated electricity demands against the total peak PV yield calculated on the basis of annual meteorological solar radiation data for roofs and static PV conversion rates of different PV technologies. The study showed the relevance of solar

potential analyses to inform policy-making decisions. Particularly, the study pointed out one key consideration for large-scale deployment of rooftop PV is prioritisation of roofs for PV integration with the additional consideration of the existing city grid capacity to receive additional PV yield. In the European Commission, Šúri et al. (2007) estimated the required PV capacity for producing a certain amount (e.g., 1%) of total energy consumption through PV systems installed on both roofs and facades in the EU member states. They used the tool r.sun (Hofierka and Suri, 2002) for predicting solar radiation without consideration of urban shading and corresponding PV yield with a static PV performance ratio of 0.75 given the output power of a PV module operating at standard test condition. This study (Hofierka and Suri, 2002) predicted the theoretical potential of PV yield at both state scale and regional scale to identify the potential region for future PV installations while taking into account geographical variability. Byrd et al. (2013) investigated the maximum PV potential using the simulation tool Ecotect (Roberts and Marsh, 2001) with a static PV conversion rate for building envelopes in study areas located in the central business district (CBD) and low-density suburbs in Auckland, New Zealand. The study demonstrated that the energy generation capacity designed on the basis of PV yield analysis contributes to reducing the electricity load of a city, supplying energy for a mixture of building types and the charging of electric vehicles, and reducing peak electricity demand.

4.2.2 Urban design phase

In the urban design phase, the key task is “place-making: creating a vision for an area and then deploying the skills and resources to realise that vision” (Yeang, 2000). In the context of integrating PV, place-making can be interpreted into two types of decision making; (1) for new development, it is optimisation of urban design to maximise solar availability by using zoning methods to control the physical characteristics of developing landscapes by imposing restrictions on variables such as maximum building height and density, extent of open space, and land use types and activities (Wilson et al., 2003); (2) for existing urban areas, it is identification of the most potential areas for solar applications and integration. For type (1), several studies (Cheng et al, 2006; Sarralde et al., 2015; Compagnon, 2004) investigated the

relationship between urban form and solar potential and found that urban parameters related to density such as plot ratio, building height, and site coverage strongly impact solar availability. Some studies developed methods of optimising urban form and building layouts to increase the solar potential of a site (Montavon, 2010; Amado and Poggi, 2014; Kanters and Horvat, 2012). Tools such as Solar Envelop are based on the pixelized sunlight shadow volume method for forming and optimising a group of buildings' envelopes over urban sites in terms of the least obstruction of sunlight to the designing buildings and the surrounding buildings (Knowles, 2003; Morello and Ratti, 2009). For type (2), solar maps have been developed to assist designers, developers, and property owners in PV investment decision-making by providing information about the solar energy potential, economic and environmental gains of a targeting area for PV installation (Mapdwell, 2018; Berlin Solar Atlas, 2018; Solarkataster, 2018). So far, existing solar maps are limited to provide solar potential evaluation of roofs as solar potential evaluation of walls and facades requires detailed consideration of urban shading and reflection. Several studies have developed analysis tools that predict solar irradiance on walls and façades in urban environments with consideration of mutual shading (Redweik et al., 2013; Lindberg et al., 2015). Existing tools such as Ladybug and Honeybee, using RADIANCE (Compagnon, 1997) as the simulation engine, and Solar Analysis in AutoCAD (formerly known as EcoTect) based on ray-tracing method were developed to generate received solar radiation on all building surfaces on the basis of hourly weather data and detailed urban geometry.

4.2.3 Building design phase

In the building design and renovation phases, performance-based design (Lewis, 2004) for sustainable buildings requires a detailed analysis of PV system performance and economic assessment. In the phases, the payback time of the PV investment is a key interest for developers and building owners to decide their investment in PV systems. Since the PV conversion rate directly determines the amount of electricity yield from a certain amount of received solar radiation, factors affecting the conversion rate have been considered in the economic analysis of PV investment at the individual building scale. Among all variables of PV system characteristics, an increased PV cell operational temperature during PV operation was found to

be the second most influential factor that creates PV yield losses (NREL, 2018), following the shading factor due to surrounding buildings. Other factors such as PV inverter losses, cable losses and solar loss due to improper maintenance (e.g., dust accumulation on the solar panel) were found to be less influential.

4.2.4 Summary of decision-making contexts selected for analysis

Following the solar planning roadmap proposed by Kanters and Wall (2016), three decision-making contexts were selected to evaluate the role of the new method: (a) solar targets: setting a solar target of a studied urban area on the basis of its maximum solar potential, (b) place-making: prioritising buildings and locations for an intended PV integration, and (c) economic assessment: assessing the economic viability of PV integration for developers, individual property owners and designers.

Table 16 lists performance indicators used for the three decision-making contexts. For evaluating the maximum solar potential, the total amount of annual PV yield potential (GWh) over the urban area of interest was selected as the indicator. As mentioned earlier in the literature review, the percent of energy production to the total energy consumption has been used as an indicator in many policies worldwide. The total PV yield potential is an essential information to calculate this indicator. For place-making, annual PV yield per area (kWh/m^2) on building surfaces, including both roofs and walls, was used to identify and prioritise the most potential buildings in a studied urban area for PV installation. For economic assessment, a common cost-effectiveness measure, simple pay-back time (year) for returning initial investment, was used to inform the economic viability of intended PV integrations.

Table 16. Typical decision-making contexts and associated decision indicators.

Decision-making contexts	Decisions	Indicator
Solar targets	Maximum PV potential	The total amount of annual PV yield (GWh)
Place-making	Prioritised buildings for PV installation	Annual PV yield per area (kWh/m^2)
Economic assessment	Economically viability of an intended PV installation on buildings	Simple payback time (year)

An urban area located in the Hankou district in Wuhan, China was used as a studied area to compare the results generated by the selected models and their effects on decision-making in the three contexts. Figure 40 shows the studied area that spans 320,000 m^2 (800m×400m). Urban geometry was simplified and assumed to be flat as slope roofs or curved envelopes are not common in the chosen area. This studied area represents a medium-to-high density form of typical urban layouts commonly seen in Asian countries.

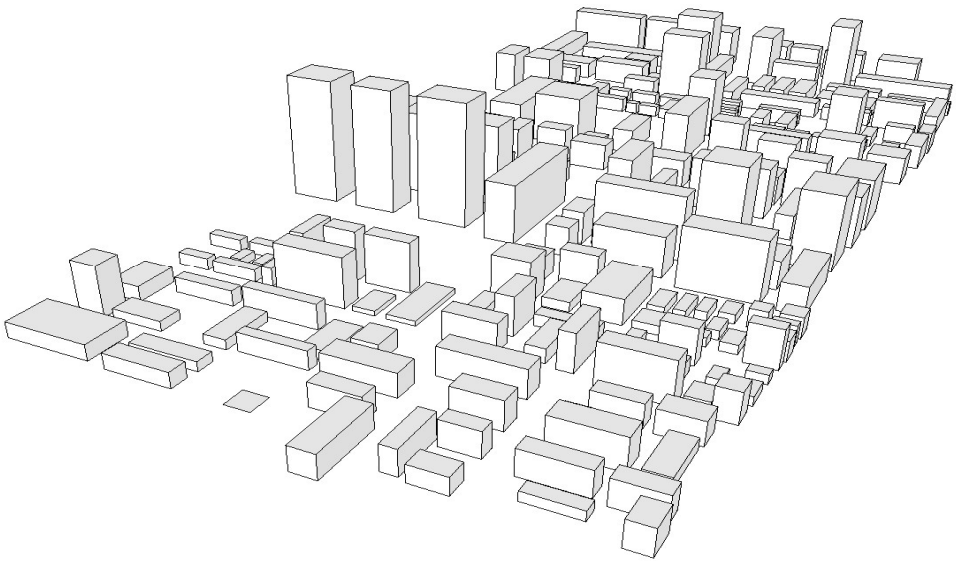

Figure 40. Urban geometry of the studied area.

4.3 Radiation prediction model

A key part of solar potential evaluation in urban areas is a solar radiation model responsible to predict solar irradiance on individual urban surfaces. Existing models can be grouped into three types in terms of their modelling considerations: (a) no consideration of urban shading; (b) crude consideration of urban shading and solar reflection among buildings with a simplified representation of urban morphology; (c) high-fidelity urban shading and solar reflection with accurate representation of surrounding buildings.

4.3.1 Classic model

Classic approaches (Fortin et al., 2008; Freitas et al., 2008; Besharat et al., 2013) that ignore urban shading and solar reflection from surrounding buildings have been long used for a quick estimation of PV yield on roofs where usually shading and reflection is less significant than those on walls. For a flat roof, the received solar irradiance equals to global horizontal irradiance I_g that is directly provided in most of the available weather files. The global horizontal irradiance (GHI) is calculated through the following expression (Freitas et al., 2015):

$$I_g = I_{norm} \mathrm{Cos}Z + I_{dh} \tag{10}$$

where I_{norm} is the direct normal irradiance or sometimes referred to as direct normal incident, I_{dh} is the diffuse horizontal irradiance, and Z is the Sun′s zenith angle. If tilted roofs are the surfaces of interest, usually an additional isotropic sky radiance model is applied to calculate the received diffuse irradiance from the partly visible sky and ground reflection (Freitas et al., 2015). As roofs are flat in the studied urban area, the classic model used in the case study is therefore in its simplest form. Nonetheless, for all urban surfaces, the model does not consider urban shading and solar reflection from the surrounding buildings and, therefore, represents the simplest approach in the studied models.

4.3.2 Canyon-based model

Several studies (Arnfied, 1990; Robinson and Stone, 2004; Bozonnet et al., 2005) adopted the concept of an urban canyon that approximates the urban form for calculating obstructions and reflected radiation due to nearby buildings in urban environment. The canyon-based model assumes that buildings that contribute to radiation obstruction and reflection have the same height without skyline variation. They only consider the surrounding buildings within the canyon while ignoring variation in the building height in an urban area. A key assumption in these studies is that radiation obstruction and reflection in regard to a view point is calculated by translating 3-dimensional urban surroundings into a 2-dimensional canyon elevation. This gives a great advantage in terms of model simplicity as there is no need to model and process a complete 3D urban geometry and, therefore, greatly reduces the modelling and computational cost. Robinson and Stone (2004) described a canyon-based method in which an obstructing wall from a view point is calculated in terms of urban horizontal angle (UHA) u for calculating solar irradiance given a Perez's anisotropic sky (Figure 41). The method computes diffuse irradiance I_{db} on a plane sloped with an angle γ and nearby obstructions defined as u as follows:

$$I_{diff} = I_{dh}[(1-F_1)\ [1 + \cos(\gamma + u)]/2 + B\ F_1 a_0/a_1 + S\ F_2 \sin \gamma] \quad (11)$$

where F_1, F_2 are Perez's coefficients responsible for the brightness of circumsolar and horizon region in relation to that of sky background, a_0 and a_1 are the relative solid angles of the circumsolar region (refer to Perez's work (Perez et al., 1993) for details). B is the Boolean operator that accounts for whether the solar disc can be seen from a view point, S is a scaling coefficient according to the proportion of the Perez's horizon band. A detailed description of the model can be found in (Robinson and Stone, 2004). As the procedure for detecting an obstructing wall (e.g. adjacent obstructions) was not clearly provided, a horizontal azimuth band of 1/9 $\boldsymbol{\pi}$ (i.e., 1/18 of the sky azimuth 2 $\boldsymbol{\pi}$) was used in the case study to calculate the UHA for each view point.

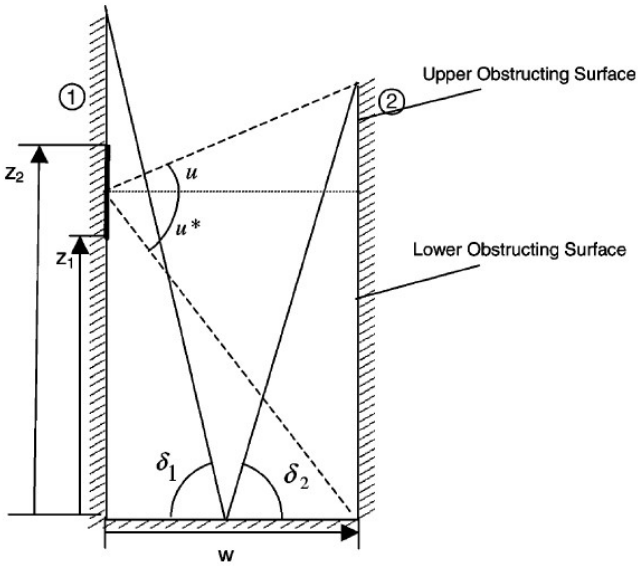

Figure 41. Concept of using an urban canyon for nearby obstruction and reflected radiation. (Image adapted from Robinson and Stone, 2004)

4.3.3 High-fidelity vector-based model

3D-vector-based approach is based on a full representation of surrounding buildings and allows for an accurate calculation of urban shading and solar reflection in a unified manner as 3D points with vector information (i.e., knowing the facing direction) do not need to be pre-classified and can be passed on for calculating daylight obstruction and reflection in the exact same manner. For instance, the previously mentioned tool, RADIANCE, uses an urban geometry model in a complete 3D format with information of surface vectors and uses computational techniques such as ray tracing or ray interception for complex calculation of detailed obstruction and reflection. However, as such a high-fidelity approach tends to cause an expensive computational cost, the simplified radiosity algorithm was developed by Robinson and Stone (2004) to improve computational efficiency for solar analysis in urban contexts.

The model proposed in the dissertation is chosen as the high-fidelity model that considers urban shading and solar reflection with an accurate representation of surrounding buildings. Detailed model description can be found in Chapter 2.

4.4 PV system model

Another part of the model for solar potential evaluation is a PV system model for estimating PV output power on the basis of PV system operational characteristics. Existing PV system models can be grouped into two types: (a) static PV system models and (b) dynamic PV system models. The PV conversion efficiency decreases when the PV cell operational temperature rises due to heat gains from the sun and the surrounding ambient environment. Radziemska (2003) found that different PV operational temperatures affect the amount of PV yield as much as 30% in extreme conditions. However, large-scale solar planning projects often deploy static PV system models that use pre-determined static PV yield conversion rates without considering dynamic PV operational characteristics depending on PV working conditions. Dynamic PV system models, on the other hand, are based on either physic-based or statistical models to calculate the dynamic PV conversion rate according to the PV cell operational temperature.

4.4.1 Static PV model

Static PV models assume the PV module operates at a fixed temperature all the time regardless of dynamic PV working conditions. Using a constant temperature always yields a fixed PV conversion rate throughout the year. The most commonly used constant temperature models are standard test condition temperature (STC) and nominal operational cell temperature (NOCT).

Standard test conditions are specific laboratory conditions that represent peak sunshine on a surface directly facing the sun in a day without clouds. PV modules are tested under STC as follows: irradiance of 1000W/m^2; a surface temperature of 25℃; a light spectrum that closely simulates sunlight; air mass at 1.5G given a standard temperature and water vapour content (Munoz et al., 2011). These idealized conditions do not reflect real PV system operation conditions. Indeed, PV systems often operate at a different temperature due to the heat received from the sunlight and heat exchange with surrounding ambient environments. An alternative method, NOCT, was established to better reflect actual PV operation conditions. A NOCT is

measured under a test irradiance of 800 W/m^2, which takes into account the fact that PV modules don't always face the sun. The test conditions also consider atmospheric or geographic conditions that may diminish sunshine. Heat convection is also considered with a wind speed of 1 m/s at 20°°C ambient temperature (Koehl, et al., 2011). Under the conditions, the measured cell temperature of a testing PV module is then defined as NOCT, which is reported by PV manufacturers as part of manufacturer's catalogues. The reported NOCT is a lot higher than STC and common NOCT values are between 40°C to 50°C (HOMER, 2017).

Although NOCT was developed to reflect more realistic PV cell operational temperature than STC temperature, it ignores actual dynamic weather conditions such as solar radiation and ambient temperature and, as a result, undermines the predication accuracy under dynamic weather conditions that vary from the assumed standard conditions. A study measured the PV cell operational temperatures of four different types of insulated PV panels for 9 months in Gaithersburg, Maryland, and revealed the unsuitability of using NOCT to predict the PV cell operational temperature under varied irradiance conditions as shown in Figure 42. (Davis et al., 2002). NOCT did not represent the dynamic behaviour of PV systems, and the discrepancy between NOCT and measured temperatures was up to 20 °C. As STC is still dominantly used in the industry and studies, the STC was selected as a static model, and obtained a pre-determined static PV conversion rate of 0.13 on the basis of the STC value for the case study.

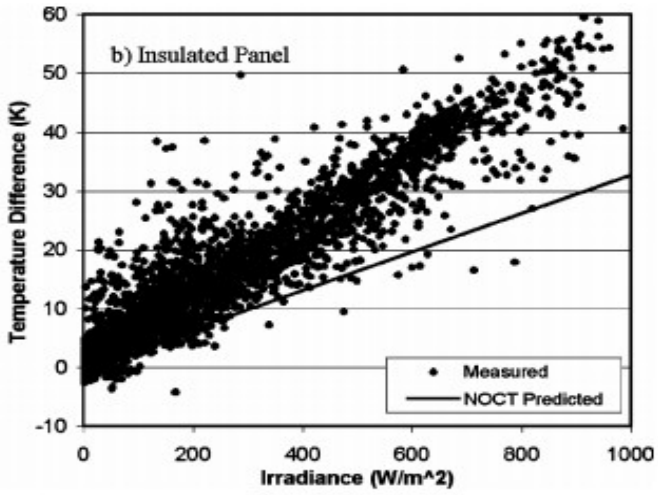

Figure 42. Temperature difference using NOCT compared to measurements. (Davis et al., 2002)

4.4.2 Dynamic PV model

A key element for the prediction of dynamic PV yield is predicting PV cell operational temperature that impacts PV system efficiency. Different models, ranging from high-fidelity physics-based models to simplified models, have been developed to predict PV cell operational temperature (Skoplaki et al., 2009; Dubey et al., 2013). Existing models can be grouped into two types: (1) physics-based models, and (2) statistical models. Physics-based methods are the most studied in the field, and a large number of models have been published in existing research papers. These models are based on a simplified form of the physical model and include correlation coefficients that capture the effect of key physical variables to simplify certain parts of the physical model. Statistical models, on the other hand, require fewer inputs as they are typically based on the simplest mathematical equation, often derived from the physical model, and derive unknown model coefficients by fitting the model to the measured PV yield data. Some of the latest statistical models use artificial intelligent methods to predict the PV cell operating temperature. Therefore, a key difference between the physics-based models and the statistical models is whether input parameters of the specific PV module are required. Physic-based models either demand detailed parameters such as solar transmittance and solar absorptance of the PV module, or require semi-empirical coefficients depending on the specific PV modules. Meanwhile, statistical models do not require any input of PV module-related parameters and usually only demand inputs of the surrounding weather conditions. Further discussion of these models and methods will be provided in the subsections.

Before investigating different PV cell operational temperature models, it is worth describing the role of PV cell operational temperature in computing the dynamic PV output power as defined in the equation (12):

$$\mathrm{P} = G_T \, \beta_{ref} \, (1 + \eta_{ref}(T_c - T_{ref})) \tag{12}$$

where, G_T is the received solar irradiance, β_{ref} is the PV conversion rate under the reference (STC) temperature (T_{ref} = 25°C). η_{ref} is the temperature coefficient of the PV module. Common values for β_{ref} and η_{ref} are summarised in Table 17, T_c is the PV cell operational temperature calculated by the models compared in this study.

Table 17. PV module properties

	T_{ref}	η_{ref}
polycrystalline-silicon PV	13.0%	-0.48 %
amorphous-silicon PV	5.5%	-0.20%

(Values provided through a survey by HOMER (2017))

4.4.2.1 Physics-based methods

Physics-based models have been developed to compute dynamic PV operational cell temperatures. For a detailed analysis of PV systems, high-fidelity dynamic simulation models have been used to accurately predict PV surface temperatures (Lobera and Valkealahti, 2013). However, for urban-scale analysis, relatively simple physics-based models are more suitable given the scale of analysis and limited data about individual buildings. Thus, three simplified physics-based models on the basis of the steady-state energy balance concept were investigated.

Skoplaki et al. (2008) developed a physics-based algorithm to calculate actual PV cell operational temperatures in relation to NOCT that is measured and provided by the manufacturers' catalogues. They developed the formula below, adopted by many studies, that predict PV cell operational temperatures on the basis of physical properties of the cell and weather conditions (i.e., ambient temperature, solar irradiance, and wind speed):

$$T_c = \frac{T_a + \left(\frac{G_T}{G_{NOCT}}\right)\frac{h_{w,NOCT}}{h_w}\left(T_{NOCT} - T_{a,NOCT}\right)\left[1 - \frac{\eta_{nef}}{\tau\alpha}\left(1 + \beta_{nef}T_{ref}\right)\right]}{1 - \frac{\beta_{nef}T_{ref}}{\tau\alpha}\left(\frac{G_T}{G_{NOCT}}\right)\left(\frac{h_{w,NOCT}}{h_w}\right)\left(T_{NOCT} - T_{a,NOCT}\right)} \quad (13)$$

Where, GNOCT and $T_{a,NOCT}$ denote standard settings used to measure NOCT; the first refers to the irradiance of 800W/m^2, and the latter refers to the ambient temperature of 20°C. $T_{a,NOCT}$ indicates NOCT (46.5 °C used in the case study). The solar transmittance of the PV panel is denoted as τ, and the solar absorptance of the panel is denoted as α. $\alpha \times \tau$ value is commonly assumed to be 0.9 (Duffie and Beckman, 1991). GT indicates the magnitude of solar irradiance on the PV panel, which can be obtained by daylight simulation or provided by existing solar maps. Ambient temperature T_a is obtained from publicly available hourly weather data, but using this data assumes that ambient temperature in the entire urban area is the same. h_w indicates convective heat transfer coefficient, which heavily depends on the wind speed. Among a wide range of convective heat transfer coefficient equations in the literature (Palyvos, 2008), Skoplaki et al. (2008) used a linear regression model that correlates the coefficient to wind speed (Loveday and Taki, 1996) as below:

$$h_w = 8.91 + 2.0 V_f \quad (14)$$

where V_f is the free-stream wind speed. Similar to the ambient temperature, publicly available wind speed data for the meteorological region corresponding to the case study area is used for the entire urban area. Hence, the equation (14) only captures the effect of regional weather conditions on the PV performance, but does not present different PV performances within the urban area due to varying microclimate conditions.

Another model, simplified from the formula above, was developed by Duffie and Beckman (1991) as defined in equation (15). The model assumes the same convective heat transfer coefficient as the nominal conditions throughout the year. Except this assumption, the formula is almost identical to the Skoplaki's model, and presents the effect of the PV system characteristics, solar irradiance, and ambient temperature on the PV operational temperature. Further description of the model is provided in (HOMER, 2017).

$$T_c = \frac{T_a + \left(\frac{G_T}{G_{NOCT}}\right)\left(T_{NOCT} - T_{a,NOCT}\right)[1 - \frac{\eta_{nef}}{\tau\alpha}(1 + \beta_{nef}T_{ref})]}{1 - \frac{\beta_{nef}T_{ref}}{\tau\alpha}\left(\frac{G_T}{G_{NOCT}}\right)\left(T_{NOCT} - T_{a,NOCT}\right)} \quad (15)$$

The third chosen model is another semi-empirical model with a Ross coefficient:

$$T_c = T_a + kG_T \quad (16)$$

In this linear expression, the Ross coefficient *k* expresses temperature rises above the ambient temperature due to the increasing solar flux (Ross, 1976):

$$k = \Delta(T_c - T_a)/\Delta G_T \quad (17)$$

The Ross coefficient value suggested by existing studies ranges between 0.02–0.04 K·m^2/W (Buresch, 1983; Ross, 1976). An IEA study provides standard Ross coefficient values depending on the level of integration and mounting types (Nordmann and Clavadetscher, 2003). Table 18 lists typical coefficient values for different mounting types provided by the IEA study.

Table 18. Standard values of the Ross coefficient k for various mounting types

PV array mounting type	*k* (K·m^2/W)
Free standing	0.021
Flat roof	0.026
Sloped roof: well cooled	0.020
Sloped roof: not so well cooled	0.034
Sloped roof: highly integrated, poorly ventilated	0.056
Façade integrated: transparent PV	0.046
Façade integrated: opaque PVs	0.054

4.4.2.2 Statistical models

In general, existing statistical models can be categorised into three types: artificial intelligence methods, semi-empirical models, and linear models. Artificial intelligence methods include artificial neural networks (Ceylan et al., 2014) or adaptive neuro Fuzzy inference system (Bassam et al., 2017). The main advantages of these methods are their versatility to capture complex trends, but as they are black-box models, they do not explicitly show relationships between explanatory variables and the dependent variables. Semi-empirical methods are created by estimating the model coefficients associated with a simplified version of the physics-based model. The simplified formula reduces the number of explanatory variables such as PV material properties and system-dependent properties while still keeping the intrinsic relationships between the key environmental variables and PV cell operational temperature. Linear models, on the other hand, are the simplest approach that captures linear trends between the key environmental variables and PV cell operational temperature.

Two statistical models were chosen in this dissertation for comparison. The first one is the Skoplaki's semi-empirical model, simplified version of the formula (13) mentioned previously:

$$T_c = T_a + \left(\frac{0.32}{8.91 + 2.0V_f}\right)G_T \quad (18)$$

The formula correlates the PV cell operational temperature to the three environmental variables: ambient temperature (T_a), free-stream wind speed (V_f), and solar irradiance received on the PV cell (G_T). The temperature estimated by the model showed a difference of less than 3 °C in comparison to its original formula (13) (Skoplaki et al., 2008). However, as this statistical model was derived on the basis of the data collected from free-standing PV systems, its applicability to other forms of PV mounting needs to be investigated.

The second statistical model chosen in this study is Muzathik's model (Muzathik, 2014):

$$T_c = 0.943T_a + 0.0195G_T - 1.528V_f + 0.3529 \quad (19)$$

The model correlates T_c with the same set of three environmental variables. It was developed by fitting a linear regression model to measured data from a polycrystalline silicon PV module mounted on the wooden frame on a flat roof in Malaysia. This model was demonstrated to show less than 1.5 ℃ difference compared to measurements (Muzathik, 2014). However, unlike the semi-empirical models, the performance of the linear regression model without explicit expression of underlying physics highly relies on the training data used for model development. Hence, the applicability of the linear model to other climate conditions needs to be tested.

4.4.3 Comparison among different PV cell temperature models

Table 19 summarises the dynamic PV models described in the last section. The two different sets of methods predicted PV cell operational temperature T_c on the urban surfaces using the case urban area described in section 4.2.4. Results of the predicted PV cell operational temperatures are discussed in this section.

Table 19. Existing models and methods

Type	**Model**	**Reference**
Physics-based	Skoplaki's model (a)	(Skoplaki et al., 2008)
	HOMER model	(HOMER, 2017)
	Empirical Ross coefficient method	(Ross, 1976)
Statistical	Skoplaki's model (b)	(Skoplaki et al., 2008)
	Muzathik's model	(Muzathik, 2014)

Figure 43 shows the average irradiance at noon throughout the year (365 noons) for individual roofs and walls in the studied urban area, predicted by the proposed vector-based radiation prediction model. The noon time represents the peak solar irradiance, which is used

as standard test conditions for constant temperature models. The standard solar intensity conditions (i.e., 1000 W/m^2 for STC and 800 W/m^2 for NOCT) are far higher than the range of solar radiation for roofs and walls in the studied urban area. More interestingly, the urban shading caused by surrounding buildings results in wide variation in the received irradiance for both roofs and walls. Especially for walls, received irradiances vary from 50W/m^2 to 400W/m^2. Differences in the received irradiance for roofs are relatively smaller since roofs are usually less shaded than walls.

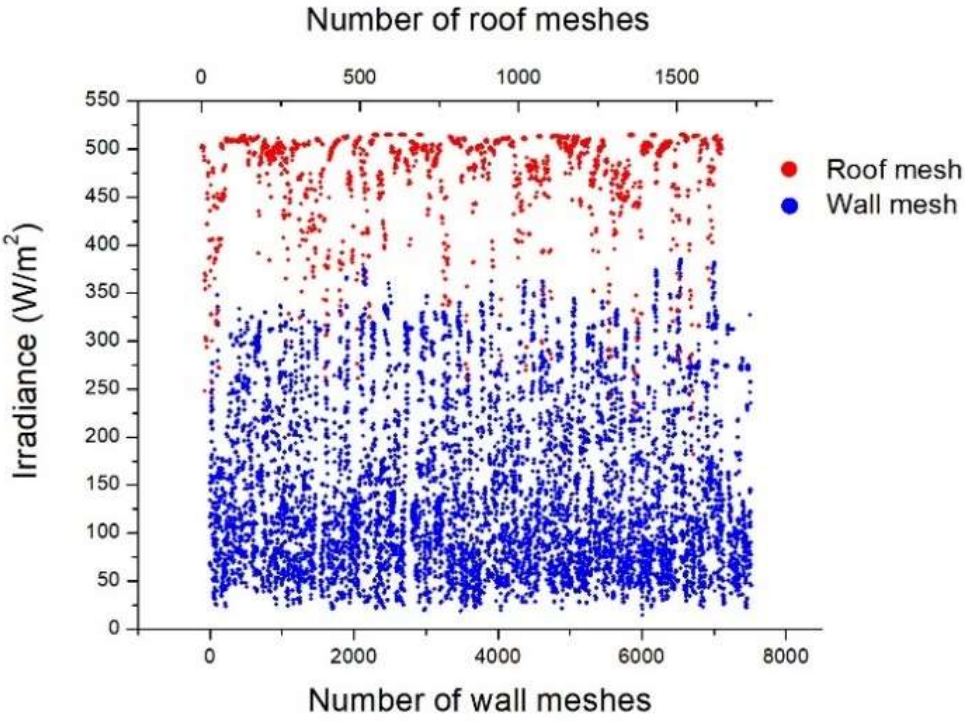

Figure 43. Average irradiance on all roofs and walls at noon.

Given these various irradiance conditions, PV cell temperature was calculated using both the static model and dynamic model. Figure 44 shows the box plot of PV cell temperature of all building surfaces at noontime, calculated by among the different methods. Results show that NOCT is much higher than all the other predictions while STC is close to the average temperatures (denoted as *) calculated by the non-constant methods. Among the non-constant methods, Empirical Ross computes the highest value with an average of 28.2°C, followed by HOMER (Tc=25.9°C) and Skoplaki's (b) (Tc=24.7°C). Muzathik linear model yields much lower values (Tc=18.72°C) than the other methods. This may be due to the inability of the

statistical model to extrapolate from the Malaysia weather data used for model development to Wuhan weather conditions. In addition, significant differences are observed in the range of PV cell temperatures predicted by the non-constant methods. Empirical Ross method results in a difference of 20℃ in the PV cell temperature whereas the other methods result in a difference of around 10 ℃. Since the same hour data of ambient temperature and wind speed is used for the entire studied area, differences in the predicted PV cell temperature at noon time are due to the differences in the received solar intensity as a result of different orientations and mutual shading conditions. However, for monthly and yearly predictions, the temporal variation in the ambient temperature and wind speed can be accounted for the prediction of the cell temperature depending on the choice of the model.

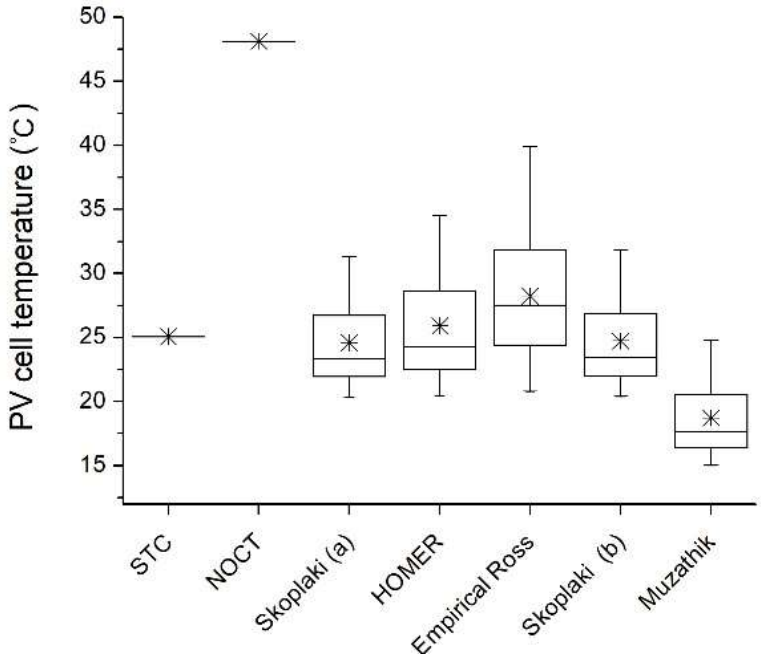

Figure 44. predicted PV cell operational temperature of all urban surfaces at noon.

As roofs and walls receive quite different levels of irradiance, results of predictions are presented separately for roofs and walls. PV cell temperature predictions at noontime for the roofs are shown in Figure 45. All the non-constant methods except Muzathik method yields cell temperatures approximately 5 to 10 C^{o} higher than STC, but still much lower than NOCT. For the roofs, the variation in the cell temperature is very small (around 3 ºC). The differences in the average PV cell temperature predicted by the non-constant methods are also very small. The

prediction results for the walls are shown in Figure 46. As the walls take up more than 70% of the total surfaces, the predictions of the PV cell temperature for the walls are quite similar to the overall results. A significant variation in the PV cell temperature is observed for the walls due to the shading effects of surrounding buildings in urban environments. In addition, Empirical Ross method results in a much wider range of the cell temperature predictions than the other methods as it uses a different coefficient depending on the PV mounting type. In general, STC seems a reasonable value used to predict PV peak yield for walls, but for roofs, neither STC nor NOCT reflects the results calculated by the non-constant models.

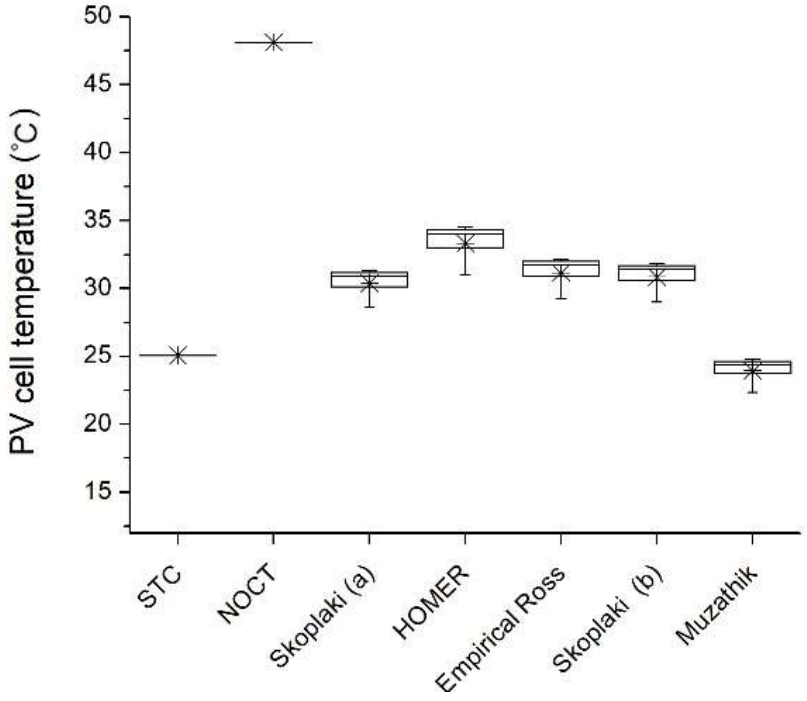

Figure 45. predicted PV cell temperatures of roofs at noon.

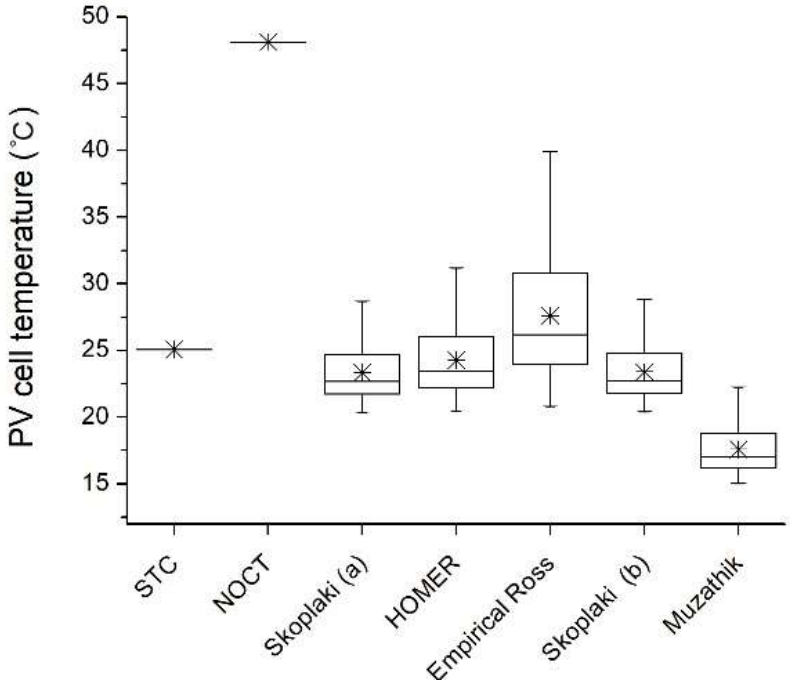

Figure 46. predicted PV cell temperatures of walls at noon.

So far, methods in terms of their predictions for the peak irradiance period were compared. However, one of the key performance indicators used for urban-scale solar analysis is the total PV yield throughout the year. Hence, monthly PV cell temperature and PV output power are used for further analysis. Figures 47 and 48 illustrate the monthly average PV cell operating temperature predictions during day time. The pattern of monthly temperature variations is quite similar between roofs and walls. However, the cell temperatures for roofs are constantly higher (2 - 8ºC) than those for walls. The magnitude of differences in the temperature prediction between different methods for both walls and roofs is similar: approximately 7 ºC and 10 ºC difference for the summer and winter, respectively. In general, differences in the monthly prediction by the non-constant methods are much larger than the peak-time prediction. This is expected as solar radiation intensity, ambient temperature, and wind speed substantially vary depending on the season. Except for Muzathik's method, all temperature-dependent methods compute similar PV cell operating temperature predictions. Muzathik's method computes lower temperatures than the other methods, which are even lower than the ambient temperature. PV cell operating temperature is very unlikely to be below ambient temperature during day time due to solar heat gains. As Muzathik's method is a linear regression model based on the hot

climate data, it does not properly predict the cell temperature for other locations with milder climate conditions.

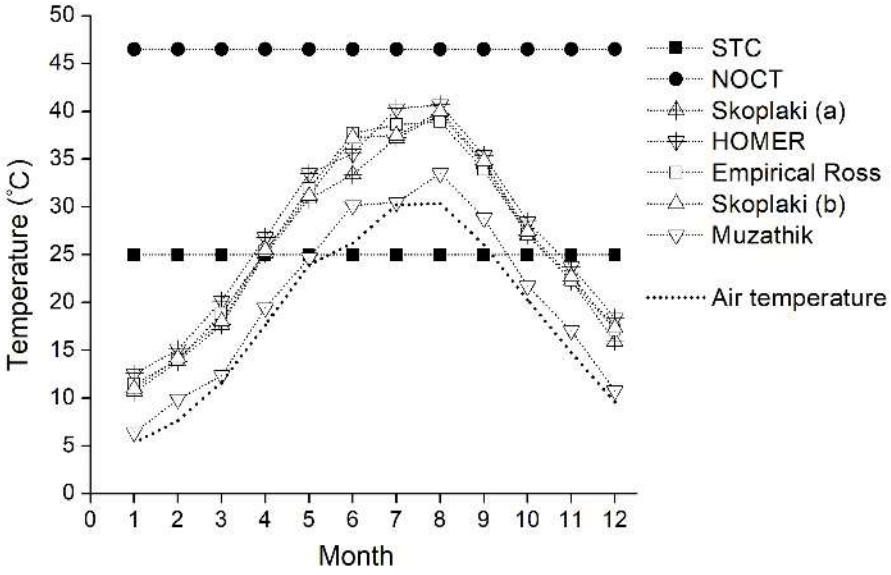

Figure 47. Monthly average PV cell temperatures for roofs.

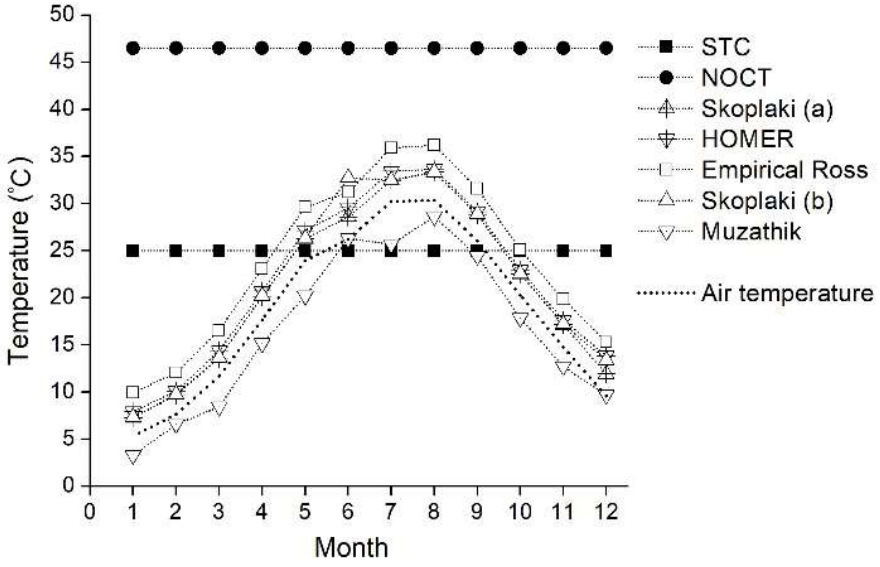

Figure 48. Monthly average PV cell temperatures for walls

Figures 49 and 50 illustrate the predicted monthly average PV output powers (W/m^2) for roofs and walls, respectively. It is obvious that PV power outputs for roofs are a lot higher than for walls if one assumes all walls, including heavily shaded ones, are implemented with PV. However, it does not mean that walls are not suitable for PV applications as a considerable

number of walls receive sufficient irradiance (Figure 43). This suggests that the solar potentials of walls should be carefully examined with consideration of the mutual shading for the selection of wall areas and the design of PV systems. Owing to the low average irradiance on walls, different methods do show very little difference in the PV power prediction. However, for roof predictions, they result in the difference, ranging between 4 to 10 W/m^2. In general, STC yields PV power predictions close to the non-constant methods except the summer season where STC prediction is higher than the others. As NOCT uses a much higher cell temperature than the non-constant methods, it substantially under-predicts the PV yield in comparison to the non-constant methods. Differences in the PV power predicted by the different non-constant methods are approximately between 1 - 4 W/m^2. The differences are smaller during the winter than during the summer.

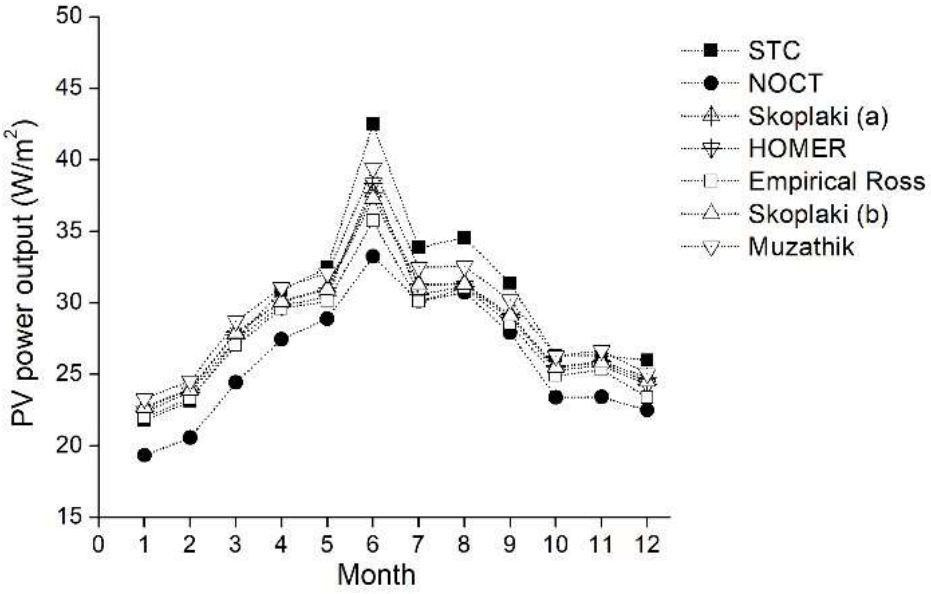

Figure 49. Monthly average PV yields for roofs

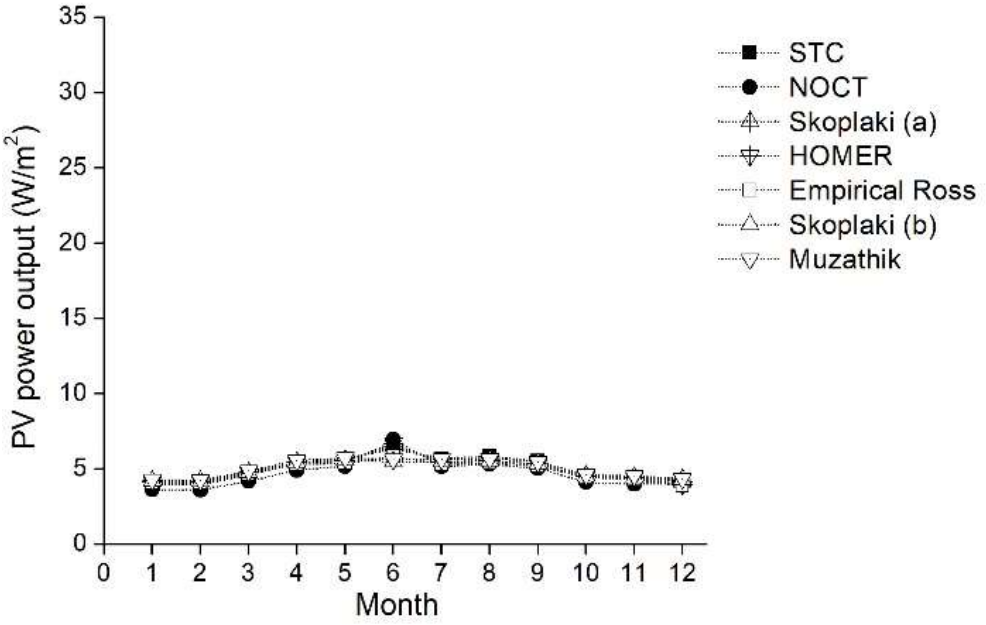

Figure 50. Monthly average PV yields for walls

Figure 51 and 52 show the relationship between and two key environmental variables (i.e., ambient temperature and received irradiance) and the PV cell temperature, respectively, using the Skoplaki's model (a) as an example. Each plot presents the average cell temperature predictions of all urban surfaces in the studied area at noon (i.e. 365 data points). The model showed highly positive correlations between the ambient temperature and the PV cell temperature. Indeed, as PV modules work in the outdoor environment, convective heat transfers between the air and PV panels significantly impact the PV cell temperature. A positive correlation was seen between the received irradiance and PV cell temperature due to part of the received solar radiation heating up the PV cell. However, the magnitude of this correlation was smaller than that of the ambient temperature. It is worth mentioning that the typical weather file recorded in a weather station was used as the ambient temperature without the consideration of microclimate conditions in the urban area. Nevertheless, the results highlight differences between the static and dynamic PV models in taking into consideration the dynamic working conditions of a PV system.

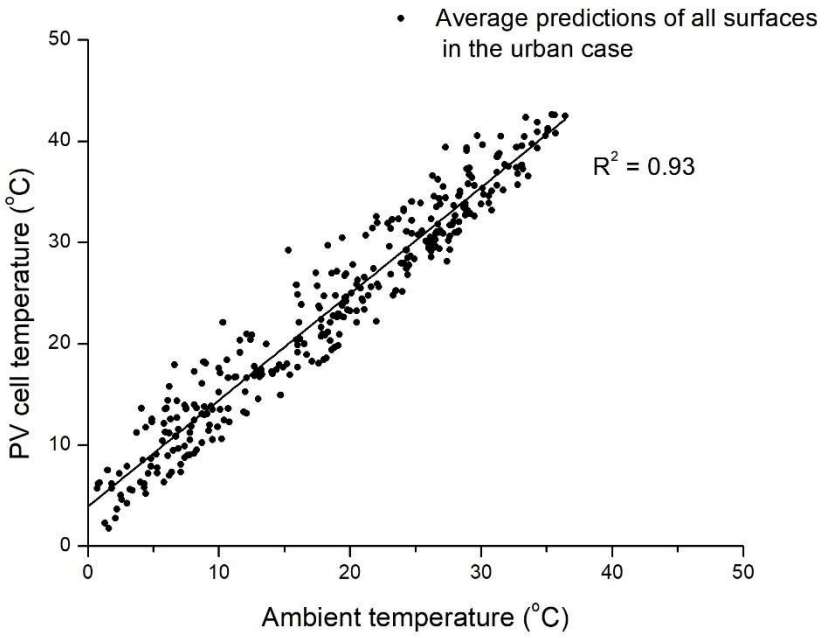

Figure 51. Relationship between ambient temperature and predictions of PV cell temperature generated by the Skoplaki's model (a).

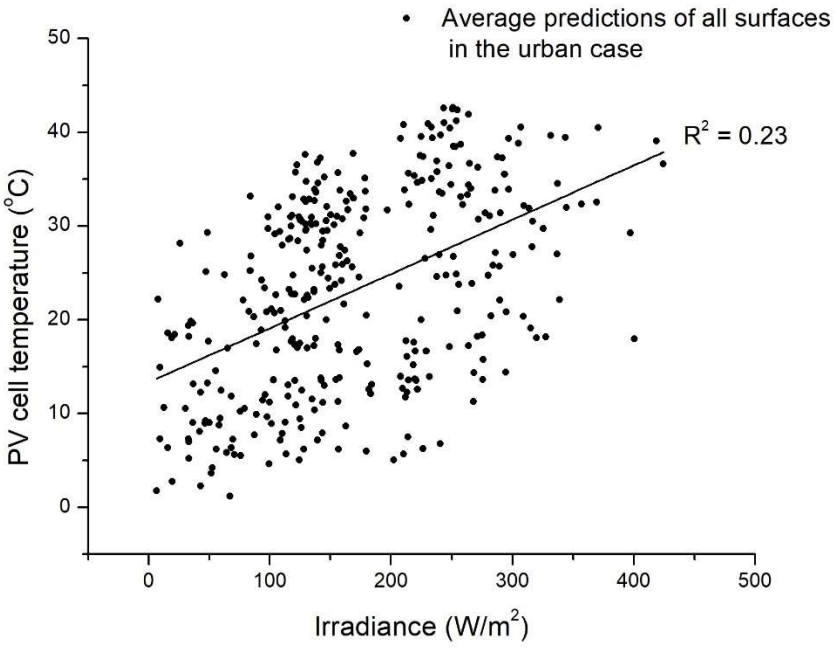

Figure 52. Relationship between received irradiance and predictions of PV cell temperature generated by the Skoplaki's model (a).

Both the Static PV model (i.e., constant temperature) and Dynamic PV model (i.e. physics-based and statistical methods) were compared in terms of the PV cell operating temperature and PV electricity yield prediction. STC yields the monthly PV power prediction in good agreement with the non-constant methods but over-predicts the monthly PV power during the summer time. On the other hand, as NOCT was much higher than PV cell temperatures predicted by the non-constant methods, it substantially under-predicted the monthly PV yield throughout the year. The non-constant methods resulted in quite similar results except Muzathik's method, which highlighted the usefulness of maintaining underlying physics in a simplified empirical model. Results also showed the predicted PV cell temperature was highly correlated to ambient temperature and considerably correlated to received solar radiation. In general, the case study showed relatively significant differences in the PV cell temperature prediction but smaller impacts on the PV output power.

4.5 Comparison in decision-making contexts

This section compares predicted performance indicators and corresponding decisions derived by the chosen models in the three decision-making contexts. The first part of the section investigates the relevance of the high-fidelity urban shading and solar reflection model on decision-making, and the second part investigates the relevance of the dynamic PV system.

4.5.1 Selected models for comparisons

Table 20 summarises the list of models used for comparison and their key data requirements.

Three solar prediction models are chosen to represent two levels of model fidelity. All solar radiation models require basic solar measurements, including global horizontal irradiance, direct normal irradiance and diffuse horizontal irradiance. They are typical data commonly accessible from the current weather files such as TMY2/3. Both the canyon-based model and vector-based model require an anisotropic sky model for generating radiance inputs across the skydome, and both use the Perez's all-weather sky model (Perez, et

al., 1993). A key difference between the two models is that the canyon-based model only demands partial urban geometry information such as canyon-related angles of an opposing street from viewpoints of interest while the vector-based model requires a complete 3D urban geometry with surface vectors to properly account for urban shading and solar reflection.

As regards the PV yield model, both static and dynamic models require received solar radiation as the base value for converting solar radiation into PV yield. STC was chosen as the static model. The static model only requires a pre-determined static PV conversion rate, and typical conversion rates are those measured under the standard test condition assuming the PV panel operating at 25°C (STC model). In contrast, the dynamic model embraces the dynamic PV cell operational temperature due to heat gains in the PV cell and consequently changing the conversion rate. As different dynamic PV models resulted in a varying range of PV cell temperatures as the previous section has suggested, all the five dynamic PV models discussed in the previous section were used to compute the plausible range of PV yields with consideration of dynamic working conditions for assessing maximum PV potential. However, one deterministic PV output generated by Skoplaki's model (a) was used for place-making and economic assessment decision contexts.

Table 20. List of models and their key data requirements.

Solar radiation model		Key data requirements for model inputs
Low-fidelity	Classic model (for roofs)	(1) Solar measurements* (2) Isotropic sky** (3) Roof tilt angle
High-fidelity	Canyon-based model (for walls)	(1) Solar measurements* (2) Anisotropic sky diffuse radiance (3) Urban canyon information
	Proposed vector-based model (for all surfaces)	(1) Solar measurements* (2) Anisotropic sky diffuse radiance (3) Complete 3D urban geometry with surface vectors
PV yield model		
Low-fidelity	Static PV model	(1) Received solar radiation (2) PV conversion rate under standard test condition (STC)
High-fidelity	Dynamic PV model	(1) Received solar radiation (2) PV temperature coefficient (3) PV system parameters*** (e.g., solar transmittance and absorptance of the PV panel) (4) Environmental measurements of the located solar panel (e.g. ambient temperature, wind speed)

*required solar measurements vary according to specific models.

**required if tilted roofs are the surfaces of interest.

***required in some physic-based PV models.

4.5.2 Examination of radiation prediction models

4.5.2.1 Solar targets: maximum PV potential

Table 21 shows the total annual PV yield potential (GWh) of all the roofs generated by the classic model and vector-based model. The two models resulted in a difference of 1.6 GWh, which corresponds to 9.8% in terms of the percentage difference. Generally speaking, roofs receive less shading from the surrounding buildings in comparison to walls. Although the complex urban landscape of the case study inevitably affected and reduced the received radiation on certain roofs, a majority of the roofs still received a high amount of solar radiation in comparison to walls. Nevertheless, buildings' heights in the studied area vary substantially

and caused observable shading on roofs. The prediction difference between the two methods may be smaller in urban landscapes where buildings have similar heights, such as cities in Europe. Given less than 10% of the difference between the two models, the results suggest that the classic model have the potential to give a reasonable prediction for evaluating the maximum PV yield of roofs at urban scale.

Table 21. Total PV yield of all roofs in the studied urban area.

	Classic model	Vector-based model
Total PV yield potential （GWh）	17.8	16.2

Table 22 shows the total annual PV yield (GWh) of all the walls in the case area by the canyon-based and vector-based models. The two models resulted in a difference of 5.9 GWh, which corresponds to 21.5% difference in terms of percentage. Table 23 summarizes the average PV yield of walls per building, computed by the two models and the standard deviation of differences between the two predictions. For individual buildings, differences in the two predictions amounted to a standard deviation of 0.061 GWh in comparison to average values of 0.179 GWh and 0.147 GWh by the two method. This comparison indicates predicting the accumulated PV yield by canyon-based model on all walls diminishes prediction discrepancies at the individual building level and leads to the total yield with a reduced prediction error. Despite the reduced prediction error at large scale, the results confirm the importance of the high-fidelity urban shading and reflection model for evaluation of maximum PV potential on walls.

Table 22. Total PV yield of all walls in the studied urban area.

	Canyon-based model	Vector-based model
Total PV yield potential （GWh）	33.3	27.4

Table 23. Standard deviation of differences between the two predictions in comparison to the Average PV yield predictions for each building.

	Canyon-based model	Vector-based model	Standard deviation of differences
Average PV yield of each building's walls (GWh)	0.179	0.147	0.061

4.5.2.2 Place-making

Figure 53 plots the predictions of annual PV yield per area (kWh/m^2) on each roof in the urban area by the classic and vector-based models. As the classic method does not consider urban shading, it yielded the same PV yield of 146 kWh/m^2 for all the roofs. The vector-based approach, on the other hand, produced varying results ranging from 92 kWh/m^2 to 145 kWh/m^2, with a calculated average of 131 kWh/m^2 and a standard deviation of 11.9 kWh/m^2. On the basis of Compagnon's work (Compagnon, 2004) that set the minimum received radiation on roofs to be 1000kWh/m^2 required for PV, a minimum yield of 130kWh/m^2 (PV conversion rate of 0.13) was used as a threshold to consider PV as a suitable option. In the figure, all the predictions by the classic model are above the threshold since only one single prediction applies to all the roofs and, therefore, all the roofs are considered suitable for PV installation. On the other hand, the vector-based approach suggests that many roofs with severe shading did not pass the threshold and got rejected. Table 24 lists the number of roofs suitable for PV determined by each of the methods. The results show that almost half of the roofs were rejected by the vector-based approach while the classic method informed that all the roofs are suitable for PV installation. This indicates the importance of modelling urban shading for identifying roof areas with high potential for PV installation. Therefore, the classic method without consideration of urban shading is not sufficient to support place-making decisions for roofs.

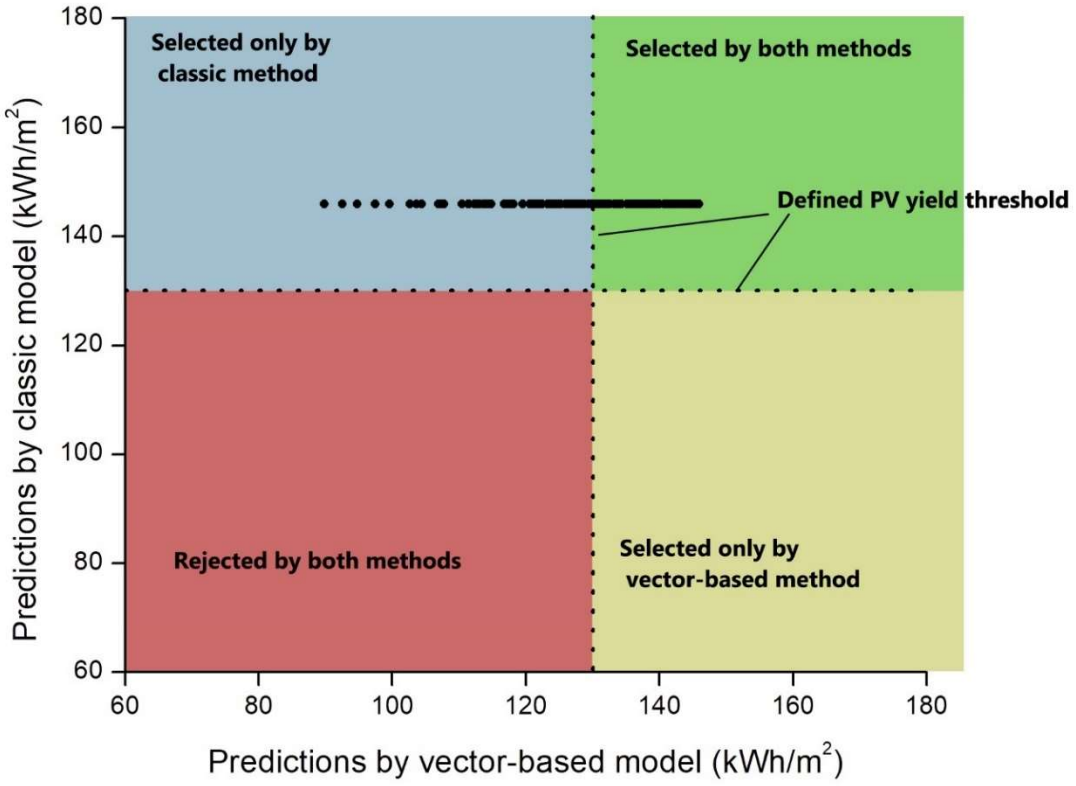

Figure 53. Annual PV yield predictions by the two methods for roofs.

Table 24. Amount of suitable and rejected roofs determined by the two models.

	Number of suitable roofs	Number of rejected roofs	Number of suitable roofs agreed by both the methods
Classic model	186	0	104
Vector-based model	104	82	

Table 25 shows the average, maximum, and minimum of annual PV yield predictions per wall area for all buildings in the urban area, computed by the canyon-based and vector-based models. Differences between the two predictions yielded a standard deviation of 17.3 kWh/m^2, which is a significantly high value compared to their average predictions. Since the canyon-based approach considers the approximate skyline obstruction only due to the opposite building walls, its calculated shading on walls may be severely overestimated or underestimated due to possibly improper representation of the surrounding obstructions.

Figure 54 shows the potentials of all buildings (only walls) that are evaluated with a PV yield threshold of 58.4 kWh/m^2. The PV yield threshold was derived to obtain a simple payback

time of twenty-five years with the current PV market price and local energy price in Wuhan found in (Suncyclopedia, 2018; Wood Mackenzie, 2018; Sate Grid, 2018). The two sets of results by the two methods showed a divergent trend. The two methods predicted very different outcomes to select building walls suitable for PV installation; they agreed to consider only a few buildings suitable for PV installation, while they yielded a disparate decision for a considerable number of buildings. Table 26 lists the number of buildings suitable for PV on walls determined by the two methods. As the canyon-based method tends to provide a higher PV yield prediction, it identified more buildings (57 buildings) suitable for PV than the vector-based model (14 buildings). only 7 buildings are considered suitable for PV on walls by both the method. As the choice of PV yield threshold is subjective to decision-makers, the results clearly highlight that predictions by the canyon-based model severely deviate from those by the vector-based approach due to improper consideration of urban shading and reflection. Therefore, the high-fidelity model of urban shading and reflection is crucial for identifying buildings on walls for PV integration.

Table 25. Annual PV yield per wall area for all buildings.

(kWh/m^2)	Canyon-based model	Vector-based model
Average	54.3	41.6
Maximum	112.5	70.8
Minimum	14.2	16.7
Standard deviation of differences between the two predictions	17.3	

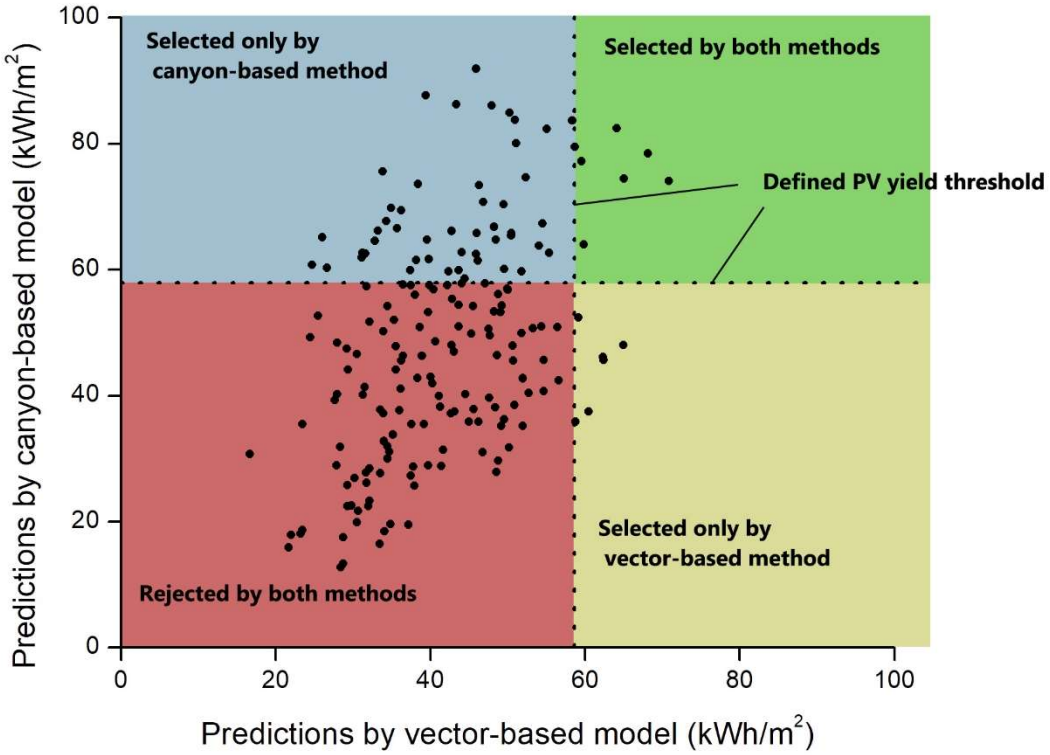

Figure 54. Annual PV yield predictions by the two methods for walls per building.

Table 26. Numbers of suitable and rejected walls determined by the methods.

	Number of suitable buildings	Number of rejected buildings	Number of suitable buildings determined by both the method
Canyon-based model	57	129	7
Vector-based model	14	172	

4.5.2.3 Economic assessment

Figure 55 plots the annual PV yield per roof area calculated by the classic and vector-based models and associated simple pay-back time. The classic method, similar to the previous analysis, predicted a single PV yield value for all roofs and therefore only yielded a single simple pay-back time of 10.1 years. The vector-based approach, predicted simple pay-back times, ranging from 10 years to over 15 years. Both the methods provided the simple pay-back times that are considered viable as currently the PV products in the market are expected to have

a lifespan of almost 30 years. Although both the models showed good economic values in all the roofs for PV integration, the vector-based approach stands out to better support economic assessment given the ability to provide specified predictions for each roof for well-informed decisions.

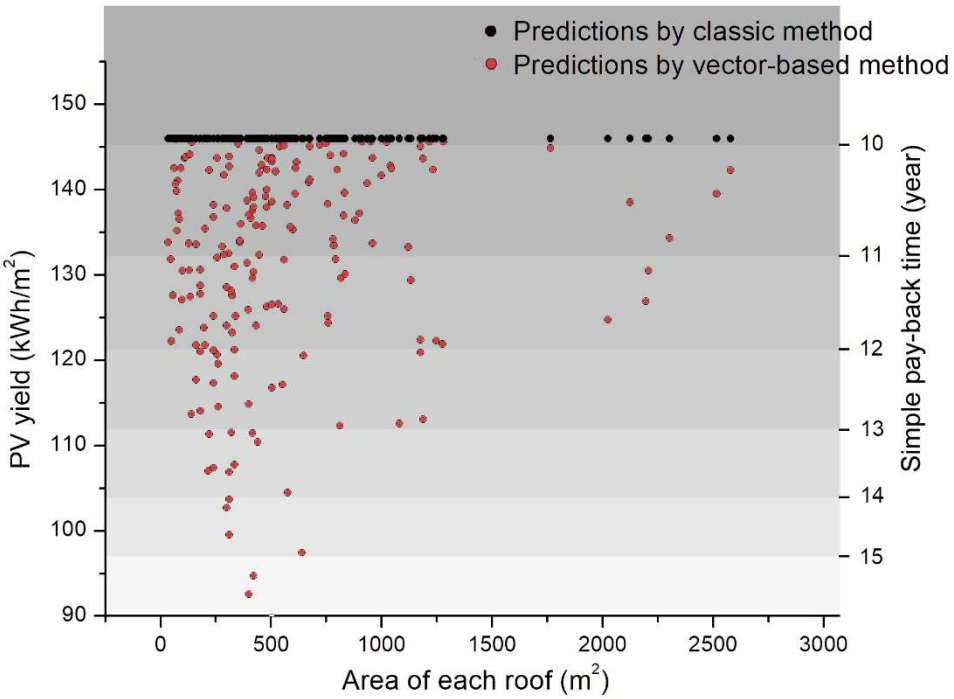

Figure 55. Simple payback times of all roofs predicted by the two methods.

Figure 56 shows the annual PV yield per wall area calculated by the two models and associated simple payback times. At first glance, it is obvious the simple payback times of the walls are much longer than those of the roofs due to severe shading on walls from the surrounding buildings. Indeed, the economic value of PV integration on the walls per area is less than that on the roofs. However, as the wall area is much larger than the roof area in an urban area, the potential PV capacity of walls and façades can be significant with applications of semi-transparent PV. Disagreements between the two predictions by the two methods are very noticeable. The canyon-based model predicted less than 30 year pay-back time for 117 buildings while the vector-based model only for 72 buildings. Some extremely long payback times as well as some very short payback times were observed in the canyon-based model results unlike the more reasonable range of predictions by the vector-based model. This comparison again highlights the inability of using the canyon concept to reflect the effect of

actual complex urban surroundings on irradiance prediction and the importance of using the vector-based model to categorize buildings in terms of their economic values.

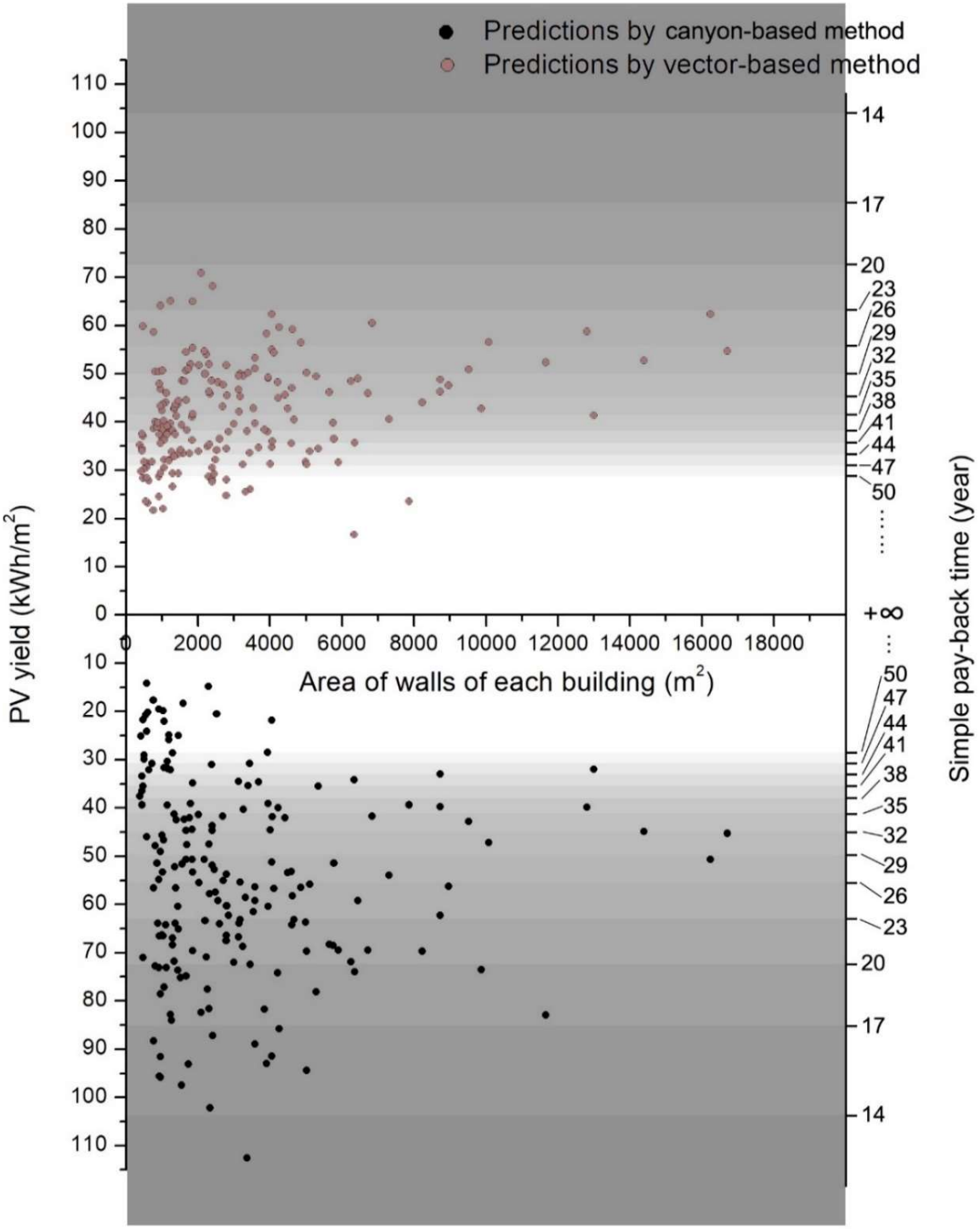

Figure 56. Simple payback times of all building walls predicted by both the methods.

4.5.3 Examination of PV models

4.5.3.1 Solar targets: maximum solar potential

Table 27 shows the total annual PV yield (GWh) of all the roofs generated by the static and dynamic PV model with the use of the vector-based model for irradiance prediction. In comparison to the dynamic models, the static model overestimated the PV yield by 0.7 GWh to 1.2 GWh, corresponding to approximately 4% to 7% difference, respectively. Small prediction differences of 0.9 to 1.9 GWh were observed for the walls as shown in Table 28. The dynamic model properly predicted higher PV cell operational temperatures caused by additional heat gains from the sun and ambient air during daytime and resulted in lower PV conversion rates while the static model kept the fixed cell operational temperature. A climate zone for the case urban area in Wuhan consists of hot summer and cold winter. Although the static model overestimated the PV conversion rate under reference temperature (i.e. 25℃) in the summer where the ambient temperature can reach as high as 40℃, the low ambient temperature in the winter counteracts the overestimation effect as a lower PV operating temperature results in higher PV conversion rate. Overall, the effect of modelling dynamic PV operational behaviour appears incremental, compared to the effect of modelling complex urban shading and reflected radiation discussed in the earlier section.

Table 27. Total annual PV yield prediction of all roofs (GWh).

	Static PV model	Dynamic PV model
Total PV yield potential （GWh）	16.2	15.0 - 15.5

Table 28. The total annual PV yield prediction of all walls (GWh).

	Static PV model	Dynamic PV model
Total PV yield potential （GWh）	27.4	25.5 - 26.5

4.5.3.2 Place-making

Figure 57 plots annual PV yield predictions for each roof in the urban area. Similar to the previous section, the static model over-predicted the PV yield, with a standard deviation of 4.1 kWh/m^2 differences between the two predictions. differences in the decisions on suitable roofs informed by the results appear slightly more noticeable in this context. Like the previous section 3.1.1, the PV yield threshold of 130 kWh/m^2 was applied to identify roofs for PV integration. 104 roofs were selected as suitable for PV integration by the static model while 81 roofs were selected by the dynamic model. Annual PV yield predictions for walls are shown in Figure 57 A small standard deviation of 2.38 kWh/m^2 differences was recorded between the two predictions. With the PV yield threshold of 58.4 kWh/m^2, 14 buildings were selected as suitable buildings for PV integration on walls by the static model while only 6 buildings selected by the dynamic model. Despite observed differences between the two results, the effect of modelling dynamic PV system on place-making is incremental when it is compared with the effects of modelling complex urban morphology on place-making; suitable roofs and walls selected by the vector-based model for PV integration were cut down from 186 to 104 and from 54 to 14, respectively.

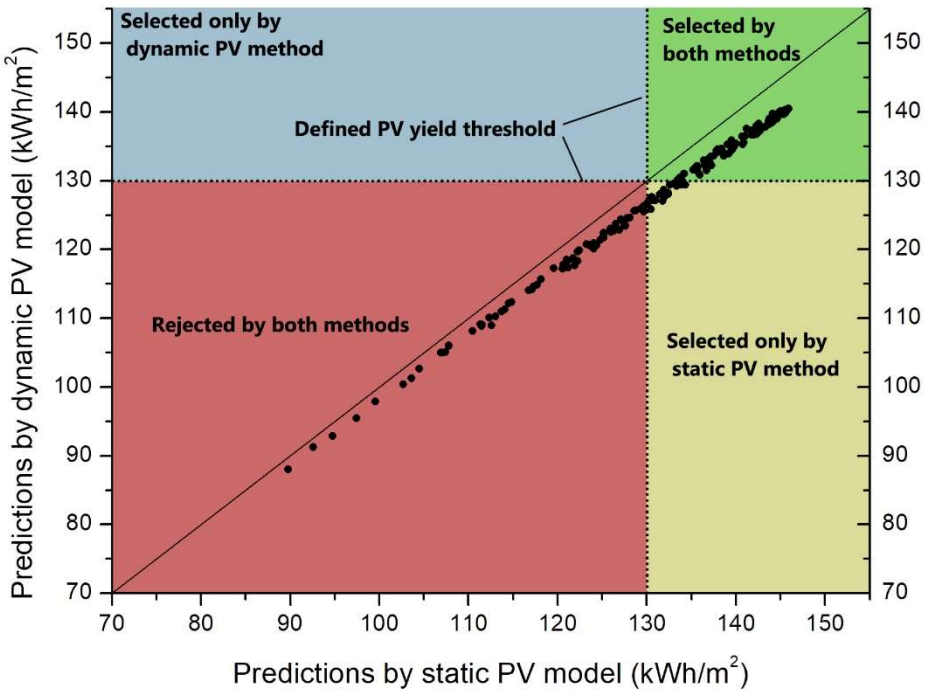

Figure 57. Annual PV yield predictions by the two method for all roofs.

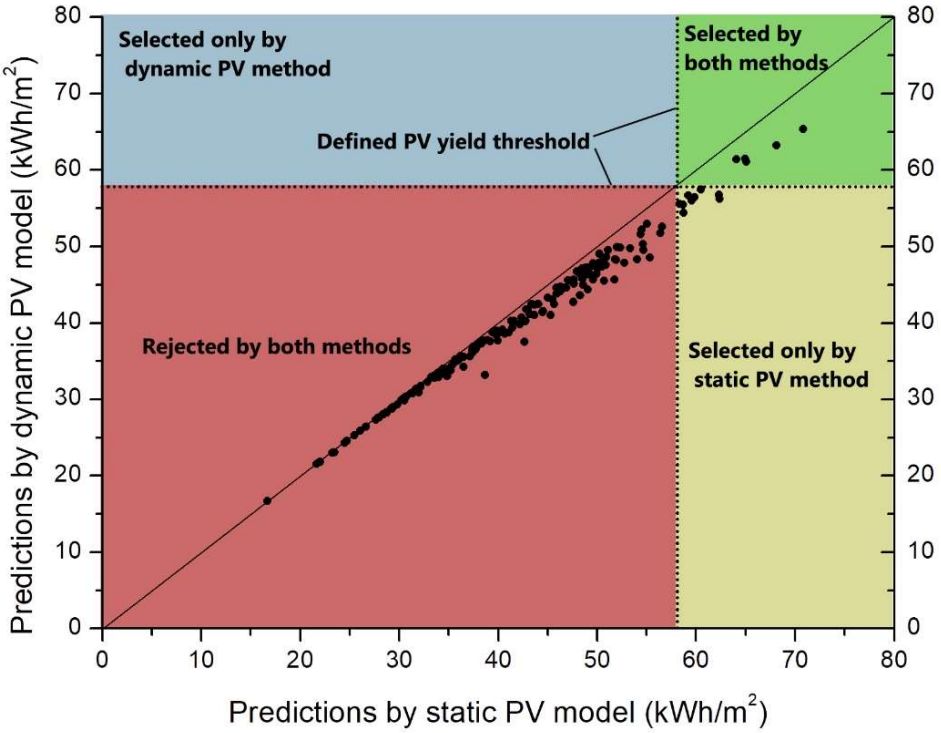

Figure 58. Annual PV yield predictions by the two methods for all buildings on walls.

4.5.3.3 Economic assessment

As small differences were observed in PV yield predictions by the static and dynamic models, relatively small differences in calculated payback times by the two methods were expected. For both roofs and walls, the static model predicted shorter payback times than those predicted by the dynamic model and, therefore, yielded a slightly higher number of buildings within shorter payback times. However, as shown in Table 29, the two methods resulted in a difference of fewer than 20 buildings within each payback time category. The differences are noticeable, but can be regarded as incremental for urban-scale economic assessment in comparison to the significant difference due to the fidelity level of modelling urban shading and reflection shown in the previous section 4.5.2.3.

Table 29. Number of buildings that fall into each category of simple payback time.

	Simple payback time (year)				
	< 14	< 13	< 12	< 11	< 10
Number of roofs					
Static model	116	112	108	93	51
Dynamic model	90	87	82	71	50
	Simple payback time (year)				
	< 47	< 41	< 35	< 29	< 25
Number of buildings (walls only)					
Static model	109	87	72	16	14
Dynamic model	99	90	56	10	6

4.6 Summary

The chapter demonstrated and examined the usability of the proposed method by examining the relevance of the following two key modelling features associated with solar potential evaluation in the solar energy planning process: (a) a level of fidelity for calculating urban shading and solar reflection and (2) dynamic PV system model. This chapter compared three different fidelities of modelling urban shading and reflection and two different levels of PV system models in terms of their relevance in major decision-making contexts for distributed PV integration at urban scale. The relevance of the models in the decision making was investigated and discussed through a case study of the urban area in Wuhan, China. Particularly, the chapter examined the effects of two major modelling features on decision-making: (1) modelling complex urban surroundings in for calculation of urban shading and reflection and (2) modelling dynamic PV operational behaviour for calculation of PV conversion rates.

As regards the fidelity level of modelling complex urban shading and reflection, the proposed model with full representation of detailed urban surroundings was compared against the classic and canyon-based methods for roofs and walls, respectively, under three decision-making contexts for urban-scale distributed PV applications. The comparison demonstrated that decisions derived by the high-fidelity vector-based model were substantially different from those derived by the classic and canyon-based models in the contexts of place-making and

economic assessment. The results indicate the high-fidelity model with an accurate reflection of urban morphology is important in calculating urban shading and reflection to correctly identify suitable buildings for PV integration and to evaluate the economic viability of intended PV integrations at urban scale. Although the classic model does not consider urban shading and reflection, it was found valuable for estimating the total maximum PV potential on roofs with acceptable accuracy for the studied urban area. It should be noted that the prediction accuracy of the classic model for roofs is likely to decrease when a studied urban area has a higher density with more variation in the building height than the case study area, and vice versa. For the evaluation of maximum PV potential on walls, the results demonstrated the importance of the high-fidelity urban shading and reflection model in comparison to the canyon-based model.

As regards the fidelity level of modelling dynamic PV conversion rates, the five different temperature-dependent PV system models were compared against the static PV system model for predicting the PV cell operating temperature and corresponding PV conversion rate. In addition, the impact of using an additional dynamic PV model on decision-making was compared against that of the high-fidelity urban shading and reflection model. For all three decision-making contexts, the dynamic and static PV models computed similar PV yield predictions, and decisions derived from the two methods appeared similar with non-negligible differences. The comparison confirmed that the effect of the dynamic PV model on decision-making is incremental in comparison to the effect of modelling complex urban shading and reflection.

Chapter 5: Conclusions and future work

5.1 Summary and conclusions

Despite the existing efforts of the developed models and tools to enable solar potential analysis, current methods are not sufficient to support solar energy planning given the urban contexts at urban scale due to the two following reasons: (1) Current advanced simulation models based on ray trace and ray interception techniques are not effectively scalable to evaluate solar potential at urban scale due to the expensive modelling process and computational cost; (2) Simple and statistical models developed for large-scale analysis are not suitable to accurately predict solar irradiance on individual surfaces with proper consideration of urban shading and reflection..

In order to overcome these limitations, this dissertation presented a simplified vector-based model on the basis of consideration of the urban context to effectively predict the solar potential at urban scale. The proposed model is based on vector-based methods without the use of ray trace and ray interception techniques, yet consists of new methods that suitably account

for the non-uniform solar radiation of the sky, obstruction by urban surfaces, and reflection by urban surfaces in urban areas. The followings are the main novelties of the new method.

- A sky discretisation tailored for urban contexts was established. The new model takes in the consideration of a typical urban view towards the sky. As buildings are typically solid masses with varying heights, starting from the ground level up to a certain height, the two-segment sky discretisation method was therefore designed to avoid unnecessary sky patches generated by the current standard Tregenza model. The two-segment sky model fully reflects urban contexts and can efficiently capture a skyline for daylight obstruction calculation with a much less required number of discretised patches. Hence, the new sky discretisation model enhances the efficiency of computing urban shading in urban contexts.

- The edge-angle-detection model, along with the unified view-angle-based reflection model, completely removes the current ray-interception/tracing algorithm in the modelling process. The new models substantially reduce the number of iterations in the calculation process of detecting obstruction and reflection in comparison to the current simplified ray-based methods such as SRA (Robinson, 2004). The new method takes a substantial step towards a much more efficient approach for calculating solar irradiance at urban scale.

- The new vector-based method was established with flexible control parameter settings, including Sky Horizontal Subdivision (SHS), Strip Inside Subdivision (SIS), Sky Radiance Sampling Subdivision (SRSS), and Building Edge Subdivision (BES) for various requirements of prediction accuracy. Furthermore, data requirement is significantly reduced as surface properties are only required as an average value separately for the buildings and roads.

The comparison study in Chapter 3 proved that the new model provides reasonably accurate predictions with flexible control settings and fewer model inputs to effectively support

large-scale solar analyses. In comparison to RADIANCE, the new model yielded predictions with the average differences of 3%, 4%, and 6%, for the low-, medium-, and high-density areas, respectively. The second comparison against measurements revealed that the model tended to overpredict the irradiance received on surfaces with a high sky view factor such as roofs and underpredict that on vertical surfaces with a low sky view factor. However, the average absolute differences between predictions and measurements were relatively small and of the order of 6% and 5% for horizontal and vertical surfaces, respectively. The computational efficiency of the new model was proven to be sufficiently improved in comparison to the current ray interception algorithms. The new model greatly reduced the iterations required for obstruction calculation that consumes the most of the computational load and, therefore, greatly reduced the computational cost for large-scale solar simulation.

The case study demonstrated the usability of the proposed method by examining the relevance of the developed method in the urban solar energy planning process, specifically in the context of the distributed PV planning process for making solar targets, place-making and economic assessment. Two key modelling features associated with solar potential evaluation were investigated in the solar energy planning process: (a) a level of fidelity for calculating urban shading and solar reflection and (2) dynamic PV system model. Results demonstrated that decisions derived by the new vector-based model with a full representation of urban morphology were substantially different from those derived by the classic and canyon-based models in the contexts of place-making and economic assessment, indicating the high-fidelity model with an accurate reflection of urban morphology is important in calculating urban shading and reflection to correctly identify suitable buildings for PV integration and to evaluate economic viability of intended PV integrations at urban scale. As regards the fidelity level of modelling dynamic PV conversion rates, for all three decision-making contexts, the dynamic and static PV models computed similar PV yield predictions, and decisions derived from the two methods appeared similar with non-negligible differences. The contrast in the two comparisons further highlighted the importance of solar analysis with full representation of urban surroundings in the calculation of urban shading and solar reflection to correctly support

distributed PV planning.

.

5.2 Future research

Several limitations of this modelling research should be noted, and future work should be initiated to resolve the following issues.

- The new models tailored the data requirement to the current urban data availability where albedos are not commonly provided on individual buildings. However, there is a growing effort to collect ground-based and remote-sensed survey data (Romanoni, et al., 2017; Sun et al., 2012), which can be used to estimate individual surface properties at urban scale in a cost-effective manner in the future. It is worth to test such data availability of individual surface properties and to confirm its impact on the prediction of solar energy and urban solar planning process. Therefore, additional model options for different albedos assigned for individual buildings and ground surfaces need to be developed to take in the consideration of detailed urban data of surface properties.

- The dissertation carried out controlled experiments for validating the model's predictions. However, the physical micro-scale urban geometry used in the experiments is a simplified representation of a real urban environment with controlled surface properties. Although the model provided reasonably accurate predictions in comparison to the measurements from the controlled experiments, it has not been tested against measurements in real urban environments. The proposed model shall be further examined and tested, so that shading effects of the complex urban landscape such as urban vegetation can be better reflected in the results.

- The new model was programmed in the environment of Python 2.7 that is not as computationally efficient as other programming languages, such as C. The advantages of the new method in computational efficiency was therefore not fully achieved. The

new model shall be implemented in a more proficient programmed scheme to fully exploit the benefits of the model algorithm.

- The relevance of the proposed method in the solar planning process of urban distributed PV was investigated based on one urban area in Wuhan, a medium-to-high density urban morphology in a specific climate condition (i.e. Middle-latitude, hot summer cold winter). As PV cell operational temperature highly correlates to ambient temperature as the study suggested in Chapter 4, more case studies are in need to fully explore the results and draw more comprehensive conclusions in different urban forms and climate.

- Currently, the method was only implemented in Python 2.7 in a programming script without a user interface, which greatly restricts its applicability in terms of being available for general users who do not have the required programming skills. Therefore, the implementation of the proposed method in a user-friendly tool should be considered in future research. Additionally, the tool shall be tailored to suit the needs for the decision-making process, such as urban design, urban retrofit or policy evaluation where their demands related to solar potential shall be further investigated, reflected and implemented so that the developed tool can indeed help the decision-makers in the design process.

Reference

Amado, M., & Poggi, F. (2014). Solar urban planning: a parametric approach. *Energy Procedia*, *48*, 1539-1548.

Amanatides, J., & Woo, A. (1987, August). A fast voxel traversal algorithm for ray tracing. In *Eurographics* (Vol. 87, No. 3, pp. 3-10).

Arnfield, A. J. (1976). *Numerical modelling of urban surface radiative parameters* (No. 7). Discussion paper.

Arnfield, A. J. (1982). An approach to the estimation of the surface radiative properties and radiation budgets of cities. *Physical Geography*, *3*(2), 97-122.

Arnfield, A. J. (1990). Street design and urban canyon solar access. *Energy and buildings*, *14*(2), 117-131.

Arvo, J. (1986, August). Backward ray tracing. In *Developments in Ray Tracing, Computer Graphics, Proc. of ACM SIGGRAPH 86 Course Notes* (pp. 259-263).

Bansal, N. K., Mathur, R., & Bhandari, M. S. (1993). Solar chimney for enhanced stack ventilation. *Building and environment*, *28*(3), 373-377.

Bassam, A., May Tzuc, O., Escalante Soberanis, M., Ricalde, L., & Cruz, B. (2017). Temperature estimation for photovoltaic array using an adaptive neuro fuzzy inference system. *Sustainability*, *9*(8), 1399.

Berlin Environmental Atlas (2008). Solar-Energy Surface Potentials. Retrieved from https://www.stadtentwicklung.berlin.de/umwelt/umweltatlas/ed806_04.htm (accessed in Nov. 2018).

Berlin Solar Atlas (2018). Solar Maps. Retrieved from https://www.businesslocationcenter.de/en/WA/B/i/1/seite0.jsp

Besharat, F., Dehghan, A. A., & Faghih, A. R. (2013). Empirical models for estimating global solar radiation: A review and case study. Renewable and Sustainable Energy Reviews, 21, 798-821.

Beurskens, L. W., Hekkenberg, M., & Vethman, P. (2011). Renewable energy projections as published in the national renewable energy action plans of the European member states. *ECN and EEA*.[15]

Wiginton, L. K., Nguyen, H. T., & Pearce, J. M. (2010). Quantifying rooftop solar photovoltaic potential for regional renewable energy policy. *Computers, Environment and Urban Systems*, *34*(4), 345-357.

Bozonnet, E., Belarbi, R., & Allard, F. (2005). Modelling solar effects on the heat and mass transfer in a street canyon, a simplified approach. *Solar Energy*, *79*(1), 10-24.

BRE (2016). Solar PV on commercial buildings: a guide for owners and developers.

Bugler, J. W. (1977). The determination of hourly insolation on an inclined plane using a diffuse irradiance model based on hourly measured global horizontal insolation. *Solar energy*, *19*(5), 477-491.

Buresch, M. (1983). Photovoltaic energy systems: Design and installation. *New York, McGraw-Hill Book Co, 1983, 347 p.*

Byrd, H., Ho, A., Sharp, B., & Kumar-Nair, N. (2013). Measuring the solar potential of a city and its implications for energy policy. *Energy policy*, *61*, 944-952.

Cano, D., Monget, J. M., Albuisson, M., Guillard, H., Regas, N., & Wald, L. (1986). A method for the determination of the global solar radiation from meteorological satellite data. *Solar energy*, *37*(1), 31-39.

Ceylan, İ., Erkaymaz, O., Gedik, E., & Gürel, A. E. (2014). The prediction of photovoltaic module temperature with artificial neural networks. *Case Studies in Thermal Engineering*, *3*, 11-20.

Chan, Y. C., & Tzempelikos, A. (2012). A hybrid ray-tracing and radiosity method for calculating radiation transport and illuminance distribution in spaces with venetian blinds. *Solar energy*, *86*(11), 3109-3124.

Chatzipoulka, C., Compagnon, R., & Nikolopoulou, M. (2016). Urban geometry and solar availability on façades and ground of real urban forms: using London as a case study. *Solar Energy*, *138*, 53-66.

Cheng, V., Steemers, K., Montavon, M., & Compagnon, R. (2006). *Urban form, density and solar potential* (No. CONF).

China Meteorological Administration (2018). Retrived from http://www.cma.gov.cn/en2014/services/ProductsService/. (accessed in Nov. 2018)

Compagnon, D. R. (1997). RADIANCE: a simulation tool for daylighting systems. *The Martin Centre for Architectural and Urban Studies University of Cambridge Department of Architecture*.

Compagnon, R. (2004). Solar and daylight availability in the urban fabric. *Energy and buildings*, *36*(4), 321-328.

Crawley, D. B., Lawrie, L. K., Winkelmann, F. C., Buhl, W. F., Huang, Y. J., Pedersen, C. O., ... & Glazer, J. (2001). EnergyPlus: creating a new-generation building energy simulation program. *Energy and buildings*, *33*(4), 319-331.

CUNY 2017. Retrived from https://nysolarmap.com/

Davis, M. W., Fanney, A. H., & Dougherty, B. P. (2001). Prediction of building integrated photovoltaic cell temperatures. *Journal of Solar Energy Engineering 123*(3), 200-210.

Dozier, J., Bruno, J., & Downey, P. (1981). A faster solution to the horizon problem. Computers & Geosciences, 7(2), 145-151., J. (1990). Rapid calculation of terrain parameters for radiation modeling from digital elevation data. *IEEE Transactions on Geoscience and Remote Sensing*, *28*(5), 963-969.

Drummond, A. J. (1956). On the measurement of sky radiation. *Archiv Für Meteorologie, Geophysik Und Bioklimatologie, Serie B*, *7*(3-4), 413-436.

Dubayah, R., & Rich, P. M. (1995). Topographic solar radiation models for GIS. *International journal of geographical information systems*, *9*(4), 405-419.

Dubey, S., Sarvaiya, J. N., & Seshadri, B. (2013). Temperature dependent photovoltaic (PV) efficiency and its effect on PV production in the world–a review. *Energy Procedia* 33, 311-321.

Duffie JA, Beckman WA.(1991). Solar Engineering of Thermal Processes 2nd edition, Wiley, New York.

Dupeyrat, P., Ménézo, C., & Fortuin, S. (2014). Study of the thermal and electrical performances of PVT solar hot water system. *Energy and Buildings*, *68*, 751-755.

EDiNA (2018). Retrieved from https://digimap.edina.ac.uk/

Erdélyi, R., Wang, Y., Guo, W., Hanna, E., & Colantuono, G. (2014). Three-dimensional SOlar RAdiation Model (SORAM) and its application to 3-D urban planning. *Solar Energy*, *101*, 63-73.

European Union. (2009). Directive 2009/28/EC of the European Parliament and of the Council of 23 April 2009 on the promotion of the use of energy from renewable sources and amending and subsequently repealing Directives 2001/77/EC and 2003/30/EC. *Official Journal of the European Union*, *5*, 2009.

Fortin, J. G., Anctil, F., Parent, L. É., & Bolinder, M. A. (2008). Comparison of empirical daily surface incoming solar radiation models. *Agricultural and forest meteorology*, *148*(8-9), 1332-1340.

Freitas, S., Catita, C., Redweik, P., & Brito, M. C. (2015). Modelling solar potential in the urban environment: State-of-the-art review. *Renewable and Sustainable Energy Reviews*, *41*, 915-931.

Fu, P., & Rich, P. M. (1999). Design and implementation of the Solar Analyst: an ArcView extension for modeling solar radiation at landscape scales. In *Proceedings of the nineteenth annual ESRI user conference* (Vol. 1, pp. 1-31). USA: San Diego.

Gosens, J., Kåberger, T., & Wang, Y. (2017). China's next renewable energy revolution: goals and mechanisms in the 13th Five Year Plan for energy. *Energy Science & Engineering*, *5*(3), 141-155.

Grimmond, C. S. B., Potter, S. K., Zutter, H. N., & Souch, C. (2001). Rapid methods to estimate sky‐view factors applied to urban areas. *International journal of climatology*, *21*(7), 903-913.

Gueymard, C. A., & Wilcox, S. M. (2011). Assessment of spatial and temporal variability in the US solar resource from radiometric measurements and predictions from models using ground-based or satellite data. *Solar Energy*, *85*(5), 1068-1084.

Hay, J. E., & McKAY, D. C. (1985). Estimating solar irradiance on inclined surfaces: a review and assessment of methodologies. *International Journal of Solar Energy*, *3*(4-5), 203-240.

Hay, J. E., & McKay, D. C. (1988). *Calculation of Solar Irradiances for Inclined Surfaces: Verification of Models which Use Hourly and Daily Data. Vol 1. Vol 2, Analysis Package User's Guide, Reference Manual and Programme Listings*. International Energy Agency.

Hetrick, W. A., Rich, P. M., Barnes, F. J., & Weiss, S. B. (1993). GIS-based solar radiation flux models. In *ACSM ASPRS ANNUAL CONVENTION* (Vol. 3, pp. 132-132). AMERICAN SOC PHOTOGRAMMETRY & REMOTE SENSING+ AMER CONG ON.

Hofierka, J., & Suri, M. (2002, September). The solar radiation model for Open source GIS: implementation and applications. In *Proceedings of the Open source GIS-GRASS users conference* (Vol. 2002, pp. 51-70).

HOMER (2017). Derived from https://www.homerenergy.com.

IENE (2013). PV Exceeds 2020 EU Renewable Energy Target. Retrieved from https://www.iene.eu/pv-exceeds-2020-eu-renewable-energy-target-p1842.html

Ingrams S.(2018). Is Solar PV a Good Investment? Retrived from https://www.which.co.uk/reviews/solar-panels/article/solar-panels/is-solar-pv-a-good-investment

Jakubiec, J. A., & Reinhart, C. F. (2011, November). DIVA 2.0: Integrating daylight and thermal simulations using Rhinoceros 3D, Daysim and EnergyPlus. In *Proceedings of building simulation* (Vol. 20, No. 11, pp. 2202-2209).

Jakubiec, J. A., & Reinhart, C. F. (2012). Towards validated urban photovoltaic potential and solar radiation maps based on lidar measurements, GIS data, and hourly daysim simulations. *Proceedings of SimBuild*, *5*(1), 628-637.

Kabir, E., Kumar, P., Kumar, S., Adelodun, A. A., & Kim, K. H. (2018). Solar energy: Potential and future prospects. *Renewable and Sustainable Energy Reviews*, *82*, 894-900.

Kämpf, J. H., Montavon, M., Bunyesc, J., Bolliger, R., & Robinson, D. (2010). Optimisation of buildings' solar irradiation availability. *Solar energy*, *84*(4), 596-603.

Kanters, J., & Horvat, M. (2012). Solar energy as a design parameter in urban planning. *Energy Procedia*, *30*, 1143-1152.

Kanters, J., & Wall, M. (2016). A planning process map for solar buildings in urban environments. *Renewable and Sustainable Energy Reviews*, *57*, 173-185.

Karteris, M., Slini, T., & Papadopoulos, A. M. (2013). Urban solar energy potential in Greece: A statistical calculation model of suitable built roof areas for photovoltaics. *Energy and Buildings*, *62*, 459-468.

Kessler, W. (2017). Comparing energy payback and simple payback period for solar photovoltaic systems. In *E3S Web of Conferences* (Vol. 22, p. 00080). EDP Sciences.

Klucher, T. M. (1979). Evaluation of models to predict insolation on tilted surfaces. *Solar energy*, *23*(2), 111-114.

Knowles, R. L. (2003). The solar envelope: its meaning for energy and buildings. *Energy and buildings*, *35*(1), 15-25.

Koca, A., Oztop, H. F., Varol, Y., & Koca, G. O. (2011). Estimation of solar radiation using artificial neural networks with different input parameters for Mediterranean region of Anatolia in Turkey. *Expert Systems with Applications*, *38*(7), 8756-8762.

Koehl, M., Heck, M., Wiesmeier, S., & Wirth, J. (2011). Modeling of the nominal operating cell temperature based on outdoor weathering. *Solar Energy Materials and Solar Cells 95*(7), 1638-1646.

Kumar, L., & Skidmore, A. K. (2000). Radiation-vegetation relationships in a Eucalyptus forest. *Photogrammetric Engineering and Remote Sensing*, *66*(2), 193-204.

Lewis, M. (2004). Integrated design for sustainable buildings. *ASHRAE Journal*, *46*(9), S22.

Liang, J., Gong, J., Li, W., & Ibrahim, A. N. (2014). A visualization-oriented 3D method for efficient computation of urban solar radiation based on 3D–2D surface mapping. *International Journal of Geographical Information Science*, *28*(4), 780-798.

Liao, W., Heo, Y., & Xu, S. (2018). Evaluation of temperature dependent models for PV yield prediction. *4th Building Simulation and Optimization Conference*, Cambridge, UK.

Lindberg, F., Jonsson, P., Honjo, T., & Wästberg, D. (2015). Solar energy on building envelopes–3D modelling in a 2D environment. *Solar Energy*, *115*, 369-378.

Lobera, D. T., & Valkealahti, S. (2013). Dynamic thermal model of solar PV systems under varying climatic conditions.*Solar energy 93*, 183-194.

Loveday, D. L., & Taki, A. H. (1996). Convective heat transfer coefficients at a plane surface on a full-scale building facade. *International Journal of Heat and Mass Transfer*, *39*(8), 1729-1742.

Ma, C. C. Y., & Iqbal, M. (1983). Statistical comparison of models for estimating solar radiation on inclined surgaces. *Solar energy*, *31*(3), 313-317.

Mapdwell (2018). Solar Maps. Retrieved from https://www.mapdwell.com/en/solar (accessed in Nov. 2018).

Marion, B., Anderberg, M., Gray-Hann, P., & Heimiller, D. (2001). *PVWATTS Version 2--Enhanced Spatial Resolution for Calculating Grid-Connected PV Performance* (No. NREL/CP-560-30941). National Renewable Energy Lab., Golden, CO.(US).

McVicar, T. R., Li, L., Van Niel, T. G., Zhang, L., Li, R., Yang, Q., ... & Zhao, Y. A. (2007). Developing a decision support tool for China's re-vegetation program: Simulating regional impacts of afforestation on average annual streamflow in the Loess Plateau. *Forest Ecology and Management*, *251*(1-2), 65-81.

Melo, E. G., Almeida, M. P., Zilles, R., & Grimoni, J. A. (2013). Using a shading matrix to estimate the shading factor and the irradiation in a three-dimensional model of a receiving surface in an urban environment. *Solar Energy*, *92*, 15-25.

Mermoud, A. (1994). PVSYST: a user-friendly software for PV-system

Mészároš, I., Miklánek, P., & Parajka, J. (2002). Solar energy income modelling in mountainous areas. *ERB and NEFRIEND Proj*, *5*, 127-135.

Mohajeri, N., Upadhyay, G., Gudmundsson, A., Assouline, D., Kämpf, J., & Scartezzini, J. L. (2016). Effects of urban compactness on solar energy potential. *Renewable Energy*, *93*, 469-482.

Möller, T., & Trumbore, B. (2005, July). Fast, minimum storage ray/triangle intersection. In *ACM SIGGRAPH 2005 Courses*(p. 7). ACM.

Montavon, M. (2010). *Optimisation of urban form by the evaluation of the solar potential* (No. THESIS). EPFL.

Morello, E., & Ratti, C. (2009). Sunscapes:'Solar envelopes' and the analysis of urban DEMs. *Computers, Environment and Urban Systems*, *33*(1), 26-34.

Muneer, T. (1997). Perez slope irradiance and illuminance models: evaluation against Japanese data. *International Journal of Lighting Research and Technology*, *29*(2), 83-87.

Munoz, M. A., Alonso-García, M. C., Vela, N., & Chenlo, F. (2011). Early degradation of silicon PV modules and guaranty conditions. *Solar energy 85*(9), 2264-2274.

Muzathik, A. M. (2014). Photovoltaic modules operating temperature estimation using a simple correlation. *International Journal of Energy Engineering 4*(4), 151.

Nadal, R. P., & Moll, V. M. (2012). Optical analysis of the fixed mirror solar concentrator by forward ray-tracing procedure. *Journal of Solar Energy Engineering*, *134*(3), 031009.

Nordmann, T., & Clavadetscher, L. (2003, May). Understanding temperature effects on PV system performance. In *3rd World Conference onPhotovoltaic Energy Conversion, 2003. Proceedings of* (Vol. 3, pp. 2243-2246). IEEE.

Nordmann, T., & Clavadetscher, L. (2003, May). Understanding temperature effects on PV system performance. In *Photovoltaic Energy Conversion, 2003. Proceedings of 3rd World Conference on* (Vol. 3, pp. 2243-2246). IEEE.

NREL (2018). Retrieved from https://photovoltaic-software.com/principle-ressources/how-calculate-solar-energy-power-pv-systems (accessed in Nov. 2018).

O'Hegarty, R., Kinnane, O., & McCormack, S. J. (2016). Review and analysis of solar thermal facades. *Solar Energy*, *135*, 408-422.

Palyvos, J. A. (2008). A survey of wind convection coefficient correlations for building envelope energy systems' modeling. *Applied thermal engineering*, *28*(8-9), 801-808.

Paul, D., Mandal, S. N., Mukherjee, D., & Chaudhuri, S. B. (2010). Optimization of significant insolation distribution parameters–A new approach towards BIPV system design. *Renewable Energy*, *35*(10), 2182-2191.

Perez, R., Seals, R., & Michalsky, J. (1993). All-weather model for sky luminance distribution—preliminary configuration and validation. *Solar energy*, *50*(3), 235-245.

Perez, R., Seals, R., Ineichen, P., Stewart, R., & Menicucci, D. (1987). A new simplified version of the Perez diffuse irradiance model for tilted surfaces. *Solar energy*, *39*(3), 221-231.

Radziemska, E. (2003). The effect of temperature on the power drop in crystalline silicon solar cells. *Renewable energy*, *28*(1), 1-12.

Redweik, P., Catita, C., & Brito, M. (2013). Solar energy potential on roofs and facades in an urban landscape. *Solar Energy*, *97*, 332-341.

Reinhart, C., & Breton, P. F. (2009). Experimental validation of Autodesk® 3ds Max® Design 2009 and DAYSIM 3.0. *Leukos*, *6*(1), 7-35.

Reuter, H. I., Kersebaum, K. C., & Wendroth, O. (2005). Modelling of solar radiation influenced by topographic shading—evaluation and application for precision farming. *Physics and Chemistry of the Earth, Parts A/B/C*, *30*(1-3), 143-149.

Roberts, A., & Marsh, A. (2001). ECOTECT: environmental prediction in architectural education. Retrieved from http://papers.cumincad.org/cgi-bin/works/Show?09cd (accessed in Nov. 2018).

Robinson, D., & Stone, A. (2004). Solar radiation modelling in the urban context. *Solar energy*, *77*(3), 295-309.

Robinson, D., Campbell, N., Gaiser, W., Kabel, K., Le-Mouel, A., Morel, N., ... & Stone, A. (2007). SUNtool–A new modelling paradigm for simulating and optimising urban sustainability. *Solar Energy*, *81*(9), 1196-1211.

Robinson, N., & Stoch, L. (1964). Sky radiation measurement and corrections. *Journal of Applied Meteorology*, *3*(2), 179-181.

Romanoni, A., Fiorenti, D., & Matteucci, M. (2017, September). Mesh-based 3D textured urban mapping. In *2017 IEEE/RSJ International Conference on Intelligent Robots and Systems (IROS)* (pp. 3460-3466). IEEE.

Ross Jr, R. G. (1976). Interface design considerations for terrestrial solar cell modules. In *12th Photovoltaic Specialists Conference* (pp. 801-806).

Roudsari, M. S., Pak, M., & Smith, A. (2013, August). Ladybug: a parametric environmental plugin for grasshopper to help designers create an environmentally-conscious design. In *Proceedings of the 13th international IBPSA conference held in Lyon, France Aug*.

Sabbagh, J. A., Sayigh, A. A. M., & El-Salam, E. M. A. (1977). Estimation of the total solar radiation from meteorological data. *Sol. Energy;(United States)*, *19*(3).

Sarralde, J. J., Quinn, D. J., Wiesmann, D., & Steemers, K. (2015). Solar energy and urban morphology: Scenarios for increasing the renewable energy potential of neighbourhoods in London. *Renewable Energy*, *73*, 10-17.

Sate Grid (2018). Retrieved from http://www.hb.sgcc.com.cn/.

Schöttl, P., Moreno, K. O., Bern, G., & Nitz, P. (2016). Novel sky discretization method for optical annual assessment of solar tower plants. *Solar Energy*, *138*, 36-46.

Scratchapixel (2018). Retrived from https://www.scratchapixel.com/lessons/3d-basic-rendering/ray-tracing-rendering-a-triangle/moller-trumbore-ray-triangle-intersection (accessed in Nov. 2018)

Şenkal, O., & Kuleli, T. (2009). Estimation of solar radiation over Turkey using artificial neural network and satellite data. *Applied Energy*, *86*(7-8), 1222-1228.

Skoplaki, E., & Palyvos, J. A. (2009). On the temperature dependence of photovoltaic module electrical performance: A review of efficiency/power correlations. *Solar energy*, *83*(5), 614-624.

Skoplaki, E., Boudouvis, A. G., & Palyvos, J. A. (2008). A simple correlation for the operating temperature of photovoltaic modules of arbitrary mounting. *Solar Energy Materials and Solar Cells*, *92*(11), 1393-1402.

Solar Simplified, 2018. Retrived from http://solarsimplified.org/solar-resources/solar-map (accessed in Nov. 2018).

Solarkataster (2018). Solar Maps. Retrieved from https://www.wien.gv.at/umweltgut/public/grafik.aspx?ThemePage=9&bookmark=FF5YRhs0JEbDZbZEHjJlRDnCjrGPfAdwccKCTH3ui0kPs1sMkmoGZjjWamRGA07JWd0S5LrYHZvcEPs-c

Song, L., Kimerling, A. J., & Sahr, K. (2002). Developing an equal area global grid by small circle subdivision. *National Center for Geographic Information & Analysis, Santa Barbara, CA, USA*.

Sözen, A., Menlik, T., & Ünvar, S. (2008). Determination of efficiency of flat-plate solar collectors using neural network approach. *Expert Systems with Applications*, *35*(4), 1533-1539.

Stritih, U., & Novak, P. (1996). Solar heat storage wall for building ventilation. *Renewable Energy*, *8*(1-4), 268-271.

Sun, J., Chen, X., Lu, X., & Xi, J. (2012). Research on 3D textured dress geometry modelling. *International Journal of Clothing Science and Technology*, *24*(2/3), 102-117.

Suncyclopedia (2018). Retrieved from http://www.suncyclopedia.com/en/solar-panels-a-nice-package-to-capture-the-sun/(accessed in Nov. 2018).

Šúri, M., Huld, T. A., Dunlop, E. D., & Ossenbrink, H. A. (2007). Potential of solar electricity generation in the European Union member states and candidate countries. *Solar energy*, *81*(10), 1295-1305.

Tarpley, J. D. (1979). Estimating incident solar radiation at the surface from geostationary satellite data. *Journal of Applied Meteorology*, *18*(9), 1172-1181.

Tregenza, P. R. (1987). Subdivision of the sky hemisphere for luminance measurements. *Lighting Research & Technology*, *19*(1), 13-14.

Tripathi, R., Tiwari, G. N., & Dwivedi, V. K. (2016). Overall energy, exergy and carbon credit analysis of N partially covered photovoltaic thermal (PVT) concentrating collector connected in series. *Solar Energy*, *136*, 260-267.

van den Brink, G. J. (1987). Validation of solar radiation models and recommendation of the model for Dutch climatological circumstances. *technisch physische dienst*, 314-226.

Vignola, F., Michalsky, J., & Stoffel, T. (2016). *Solar and infrared radiation measurements*. CRC press.

Waibel, C., Evins, R., & Carmeliet, J. (2017). Efficient time-resolved 3D solar potential modelling. *Solar Energy*, *158*, 960-976.

Walla, T. (2012). Hosting capacity for photovoltaics in Swedish distribution grids. Retrieved from http://urn.kb.se/resolve?urn=urn:nbn:se:uu:diva-207871

Walter, E., & Kämpf, J. H. (2015). A verification of CitySim results using the BESTEST and monitored consumption values. In *Proceedings of the 2nd Building Simulation Applications conference* (No. CONF, pp. 215-222). Bozen-Bolzano University Press.

Ward, G. J. (1994, July). The RADIANCE lighting simulation and rendering system. In *Proceedings of the 21st annual conference on Computer graphics and interactive techniques*(pp. 459-472). ACM.

Wiginton, L. K., Nguyen, H. T., & Pearce, J. M. (2010). Quantifying rooftop solar photovoltaic potential for regional renewable energy policy. *Computers, Environment and Urban Systems*, *34*(4), 345-357.

Wilson, J. P., & Gallant, J. C. (Eds.). (2000). *Terrain analysis: principles and applications*. John Wiley & Sons.

Wilson, J. S., Clay, M., Martin, E., Stuckey, D., & Vedder-Risch, K. (2003). Evaluating environmental influences of zoning in urban ecosystems with remote sensing. *Remote sensing of environment*, *86*(3), 303-321.

Wood Mackenzie (2018). Retrieved from https://www.woodmac.com/reports/power-markets-u-s-pv-system-pricing-h1-2018-forecasts-and-breakdowns-58176503#gs.5vdOsj0

Yeang, L. D. (2000). Urban design compendium. *English Partnerships/Housing Corporation, London*.

Zhang, S. Q., Feng W. R., Zhang W. M., Shi, J. H. (1997). The corrections and calculation method of shadowbands coefficient. *Acta Energiae Solaris Sinica* 18 (2), 157–163.

Publications

Journal Papers

Liao, W., Heo, Y., & Xu, S. (2019). Simplified vector-based model tailored for urban-scale prediction of solar irradiance. *Solar Energy*, *183*, 566-586.

In reviewing process:

Liao, W., Heo, Y., & Xu, S. Evaluation of solar analysis methods for decision support in distributed PV integration at urban scale.

Conference Papers

Liao, W., Heo, Y., & Xu, S. (2018). Evaluation of temperature dependent models for PV yield prediction. 4th Building Simulation and Optimization Conference, Cambridge, UK.

Liao, W., Heo, Y., & Xu, S. (2017). A simplified vector-based method for irradiance prediction at urban scale. IBPSA Building Simulation Conference 2017, San Francisco, USA.